Order Number 9409309

A numerical study of attached oblique detonation

Fort, James A., Ph.D.

University of Washington, 1993

U·M·I
300 N. Zeeb Rd.
Ann Arbor, MI 48106

A Numerical Study of Attached Oblique Detonation

by

James A. Fort

A dissertation submitted in partial fulfillment of
the requirements for the degree of

Doctor of Philosophy

University of Washington

1993

Approved by David T. Ratt
(Chairperson of Supervisory Committee)

Program Authorized
to Offer Degree Mechanical Engineering

Date August 18, 1993

In presenting this dissertation in partial fulfillment of the requirements for the Doctoral degree at the University of Washington, I agree that the Library shall make its copies freely available for inspection. I further agree that extensive copying of this dissertation is allowable for scholarly purposes, consistent with "fair use" as prescribed in the U.S. Copyright Law. Requests for copying or reproduction of this dissertation may be referred to University Microfilms, 1490 Eisenhower Place, P.O. Box 975, Ann Arbor, Michigan 48106, to whom the author has granted "the right to reproduce and sell (a) copies of the manuscript in microform and/or (b) copies of the manuscript made from microform."

Signature James A. Ford

Date August 18, 1993

University of Washington

Abstract

A Numerical Study of Attached Oblique Detonation

by James A. Fort

Chairperson of Supervisory Committee: *Prof. David T. Pratt*
Mechanical Engineering

The goal of this research is to develop a predictive capability for oblique detonation waves (ODWs). Planar wedge flows and axisymmetric conical flows are considered. The Rankine-Hugoniot solution is reviewed first, which yields necessary conditions for attached ODWs. But this solution is limited to inviscid flows over idealized geometries and infinite Damköhler number (Da), which is the ratio of fluid dynamical to chemical time scales. A multidimensional numerical model is developed, tested against theory, and is then used to investigate the influence of finite Da and viscous flows. Results demonstrate the role of the Damköhler number in bulk ignition. Refined grid results show that viscous (laminar) effects are confined to boundary layers and do *not* contribute to ODW formation. This conclusion corrects a previously held belief that was based on inadequately resolved simulations.

Results presented for underdriven oblique detonation waves are the first known for fuel-air mixtures of propulsion interest. Together with an explanatory model, these results suggest the existence of underdriven ODW's. Transient numerical solutions give clues to the wave's formation mechanisms, and perturbed solutions illustrate interesting properties of the wave once formed.

TABLE OF CONTENTS

LIST OF FIGURES

LIST OF TABLES

ACKNOWLEDGMENTS

I am grateful for the financial support from the Marquardt Corporation, the U.S. Air Force Office of Scientific Research and Battelle Pacific Northwest Laboratories. The NASA-Lewis Research Center provided the RPLUS code used in the initial stages of this research. Many individuals contributed to the success of this work. In particular, I wish to thank Prof. Jim Riley of the University of Washington who generously provided computer resources while I was on campus, Prof. Randy LeVeque of the University of Washington who helped me sort through the subtleties of flux Jacobian derivation, and Prof. Scott Eberhardt of the University of Washington for opening my eyes to computational fluid dynamics and helping me produce a working code. Finally, and most importantly, I wish to thank my advisor, Prof. Dave Pratt, for giving me a goal and the motivation to achieve it.

DEDICATION

To Billie and Will

Chapter 1

INTRODUCTION

Current research into hypersonic airbreathing vehicles for transcontinental or single-stage to orbit flights has generated a new appraisal of hypersonic propulsion concepts [1]. The supersonic combustion ramjet (scramjet) engine remains the most likely candidate. However, interest has been renewed in the oblique detonation wave (ODW) engine. Dunlap et al. first suggested the use of a wedge-stabilized (attached) ODW for hypersonic ramjet propulsion [2]. Since only the normal component of flow leaving an ODW is subsonic, supersonic flow exists throughout the combustor. Assuming that an ODW could be stabilized by a simple wedge, an ODW engine would require much less inlet diffusion than a diffusive-burning scramjet engine, and the scramjet combustor could be essentially eliminated as a discrete engine component [3].

The major drawback of an ODW engine foreseen in Ref. [2] was the necessity of premixing the fuel and air while avoiding ignition upstream of the stabilizing wedge. While scramjet engines did not suffer this constraint, premixing was later shown to offer significant benefits to scramjet cycle performance [4]. Furthermore, a recent finite-rate chemistry analysis [5] suggests that premixing may be required for scramjet combustion in the flight Mach number range 8 to 16, due to excessively long mixing and chemical induction (ignition delay) times. Also, any significant degree of premixing in a scramjet combustor could lead to an unwanted ODW.

In another application, Hertzberg et al. have recently proposed the use of stabilized detonation waves, both normal and oblique, among many alternative combustion modes for a ram-accelerator [6]. In this device, a shaped projectile is fired into a tube filled with a reactive gas mixture. Chemical energy release accompanying the combustion in the annulus between the projectile and tube provides the net pressure difference and means of propulsion. Yungster and Bruckner examined ram-accelerator performance for a range of superdetonative velocities [7]. Among their

results are premature combustion cases with an ODW on the forebody. While certain of these cases were shown to produce a net thrust, premature combustion normally results in net drag and failure. The problem mentioned above for ODW engines does not exist in this application since the flow is premixed by design.

The above examples are areas of propulsion research that involve ODW's, either by design or as an unwanted side effect. It is essential to be able to predict when these will occur, so as to exploit their benefits, or to avoid their consequences, whichever the case may be. Rankine-Hugoniot analysis can be used to predict necessary conditions and the resulting wave angle and jump conditions *if* an attached ODW should occur; however, by itself this approach has limited predictive capability. To accurately predict the occurrence of an attached ODW, additional factors must be considered. These include finite rate chemistry and ignition sources beyond pure bulk ignition [8], such as viscous heating in boundary layers.

Numerical simulations of ODW's that incorporate all of the important physical phenomena are now made practical by high resolution solution algorithms and fast and affordable computer resources. Numerical studies of attached ODW's are cited in the literature [9-14]. Glenn and Pratt [9] gave results for a simplified finite rate model and inviscid flow. Cambier et al [10] presented results for detailed finite rate chemistry in a high resolution solution scheme. Fort and Pratt [11] presented the first solutions that resolved finite rate effects and included viscous effects. These authors extended their analysis to conical flows in [12]. Li et al [13] explored finite rate effects for planar, inviscid flows using fine computational grids and a simplified kinetic model. Li extended his investigation to include viscous effects in [14]. The present work builds on these earlier results.

The successful application of numerical models requires diligent comparison with experiments and theory. Unfortunately, experimental results for attached ODW's do not yet exist and theory is limited to ideal gases [15]. The approach taken in this research is to compare results for two numerical models, 1) a Rankine-Hugoniot analysis, and 2) a high resolution finite-difference computational fluid dynamics (CFD) code. The Rankine-Hugoniot analysis is a simplified model that is used to verify the CFD model for limiting cases. Once verified, the CFD model is used to explore more general conditions.

This dissertation describes a systematic investigation of attached ODW's for two

canonical test problems, one characteristic of the ODW engine (internal flow over a compression ramp) and one characteristic of a ram-accelerator with premature combustion (axisymmetric conical flow). The research is limited to two-dimensional supersonic flows of hydrogen-air mixtures. Chapter 2 begins with some background on normal and oblique detonation waves. Chapter 3 describes the Rankine-Hugoniot model. The multi-dimensional, finite difference model is described in Chapter 4. In Chapter 5, results for planar geometry illustrate the impact of finite rate chemistry on ODW formation and correct earlier misconceptions about viscous effects published in [11] (these results agree with Li et al [14]). Also included are the first known results for an underdriven ODW simulation which challenge previous conclusions regarding their physical existence and suggest new mechanisms of wave support. Chapter 6 gives an expanded description of the conical detonation results in [12]. Finally, conclusions are drawn from these results in Chapter 7 and recommendations are made in Chapter 8.

Chapter 2

BACKGROUND

A detonation is a special case of shock-induced combustion and is observed in a number of physical situations, including the rapid decomposition of high explosives and the supersonic propagation of combustion waves through a combustible gas mixture. In the usual case, the detonation propagates at supersonic speed through a quiescent reactive medium. These so-called *self-propagating* detonations consist of a leading shock wave driven by energy liberated in rapid chemical reactions immediately behind the shock. Detonations may also occur as stationary combustion waves in steady supersonic flows. Examples include oblique detonation waves in supersonic combustion chambers and coupled shock deflagration waves found ahead of projectiles in reactive gas mixtures. In contrast to self-propagating detonations, stabilized detonation waves balance the kinetic energy of the incoming flow with the chemical energy release in the combustion wave. To remain stationary, the speed of the incoming flow must exceed the self-propagating wave speed.

Strehlow's definition of a detonation obviously applies only to self-propagating detonations [16], "At the present time the term *detonation* should be applied only to processes where a shock-induced combustion wave is propagating through a reactive mixture or pure exothermic compound." A preferred definition, including both self-propagating and stationary detonations, is offered by Pratt et al. [15], "When a shock-induced combustion wave follows so closely on the igniting shock wave that the two waves are fully pressure-coupled, the resulting shock/combustion wave structure is a *detonation.* By contrast, a *shock-induced combustion* wave results whenever the igniting shock wave is uncoupled, is clearly non-reactive, and is followed—typically after a measurable induction or ignition delay period—by a distinct, temporally or spatially resolvable combustion wave."

This work is concerned exclusively with stationary detonations, specifically oblique detonations, in reacting mixtures of ideal gases. To understand the physical behavior and theoretical description of an oblique detonation, it is useful to first consider the

same for a normal detonation.

2.1 *Normal Detonation*

As in normal shock theory, a normal detonation is one-dimensional, i.e., the wave has no transverse velocity relative to the burnt or the unburnt mixture (although pressure waves are known to laterally traverse the wave front [16]). Normal detonations can be divided into two groups, self-propagating and overdriven. While self-propagating waves travel at a speed characteristic of the reactive gas mixture, overdriven normal detonations require an external driving force to accelerate the wave beyond self-propagating speed. Underdriven normal detonations, should they be possible, are not of interest here.

The motion of a self-propagating detonation is derived entirely from processes within the wave. The detonation wave has a finite thickness (0.01 to 1 mm in a solid explosive [17]), and is composed of a leading shock wave, which instantaneously raises the temperature and pressure of the material, followed by a zone of rapid chemical reaction and energy release. The high temperature and pressure in the detonation wave is maintained by inertial confinement, since the surrounding material cannot be displaced appreciably before the reaction is completed [18]. Since the wave is preceded by a shock, the detonation speed is always supersonic relative to the undisturbed media; representative propagation speeds range from 2 to 3 km/s in gas mixtures to 6 to 8 km/s in liquid and solid explosives [16, 18].

The self-propagating wave speed is a unique property for a combustible gas mixture at a specific temperature and pressure, and is known as the Chapman-Jouguet, or C-J, detonation velocity. Because of this, self- propagating detonations are frequently referred to as Chapman-Jouguet detonations. The C-J detonation velocity may be readily calculated as shown in [16, 18].

2.2 *Oblique Detonation*

Oblique detonations, like overdriven normal detonations, require an external driving force to propagate the wave at velocities greater than the C-J velocity. A wedge-shaped projectile propelled at superdetonative velocity could support an oblique detonation wave (ODW) in a combustible mixture. Similarly a conical projectile could

support a conical ODW. Depending on the included angle of the wedge or cone, the ODW could be either attached or detached. Only attached waves are of interest here.

Chapter 3

RANKINE-HUGONIOT MODEL

A detailed description of the Rankine-Hugoniot model is given for the general case of planar geometry. Differences are discussed afterward for conical geometry.

3.1 Planar Geometry

This section summarizes a theoretical analysis of planar oblique detonation by Pratt, Humphrey and Glenn [15]. In their analysis the authors considered two-dimensional supersonic flow of gaseous fuel/oxidizer mixtures past a simple compression ramp or wedge. For a non-reacting flow of an ideal gas, the presence of the ramp of angle θ leads to a planar oblique shock wave with an angle β. The changes in flow properties over the shock are given by classical oblique shock theory (see for example [19]). To represent an oblique detonation wave, sensible heat due to the exothermic chemical reaction is assumed to be released entirely within the shock wave structure. This allows the coupled wave to be treated as a single discontinuity and use the same forms of the conservation equations as for the non-reacting (adiabatic) flow.

mass:

$$\rho_1 u_{1n} = \rho_2 u_{2n} \tag{3.1}$$

normal momentum:

$$p_1 + \rho_1 u_{1n}^2 = p_2 + \rho_2 u_{2n}^2 \tag{3.2}$$

tangential momentum:

$$(\rho_1 u_{1n}) u_{1t} = (\rho_2 u_{2n}) u_{2t} \tag{3.3}$$

or

$$u_{1t} = u_{2t} = u_t \tag{3.4}$$

energy:

$$h_1 + u_{1n}^2/2 = h_2 + u_{2n}^2/2 \tag{3.5}$$

For the case of a reacting (non-adiabatic) flow, the enthalpies h_1 and h_2 must include the chemical as well as the sensible enthalpies of each active species.

The specification of the problem is completed with the ideal gas equation of state,

$$p = \rho RT \tag{3.6}$$

and the kinematic relations,

$$u_{1n} = u_1 sin\beta \tag{3.7}$$

$$u_{1t} = u_1 cos\beta \tag{3.8}$$

$$u_{2n} = u_2 sin(\beta - \theta) \tag{3.9}$$

$$u_{2t} = u_2 cos(\beta - \theta) \tag{3.10}$$

Solution of equations (3.1) through (3.10), for the general case, requires the use of variable specific heats and an equilibrium calculation for the post-shock conditions.

The results for a specific free stream Mach number, pressure and temperature can be expressed on a plot of wedge angle, θ, versus wave angle, β, with heat release as a parameter. The general form of this stability map is shown in Figure 3.1. In this case heat release is expressed in terms of the fuel/air equivalence ratio,

$$\phi = (F/A)/(F/A)_{stoichiometric} \tag{3.11}$$

The curve for adiabatic flow ($\phi = 0$) is familiar from gasdynamics. For finite heat release ($\phi > 0$), two oblique detonation regimes are indicated, the underdriven regime ($M_{2n} > 1$) and the overdriven regime ($M_{2n} < 1$). Of these, a wave mechanics argument is generally used to show that only the overdriven regime is physically realizable. (This premise is brought into question in Section 5.4.) The solution is double valued for any ramp angle less than θ_{max}; this corresponds to strong and weak oblique shocks in an adiabatic flow, and to weak overdriven and strong overdriven oblique detonations (or just strong oblique detonations since all strong oblique detonations are overdriven). Also, for ramp angles less than θ_{max} the oblique shock or oblique detonation wave remains attached to tip of the ramp. If, however, the ramp angle exceeds θ_{max}, the wave becomes detached from the tip of the ramp and the present analysis is no longer useful. Finally, attention is called to the locus of states at

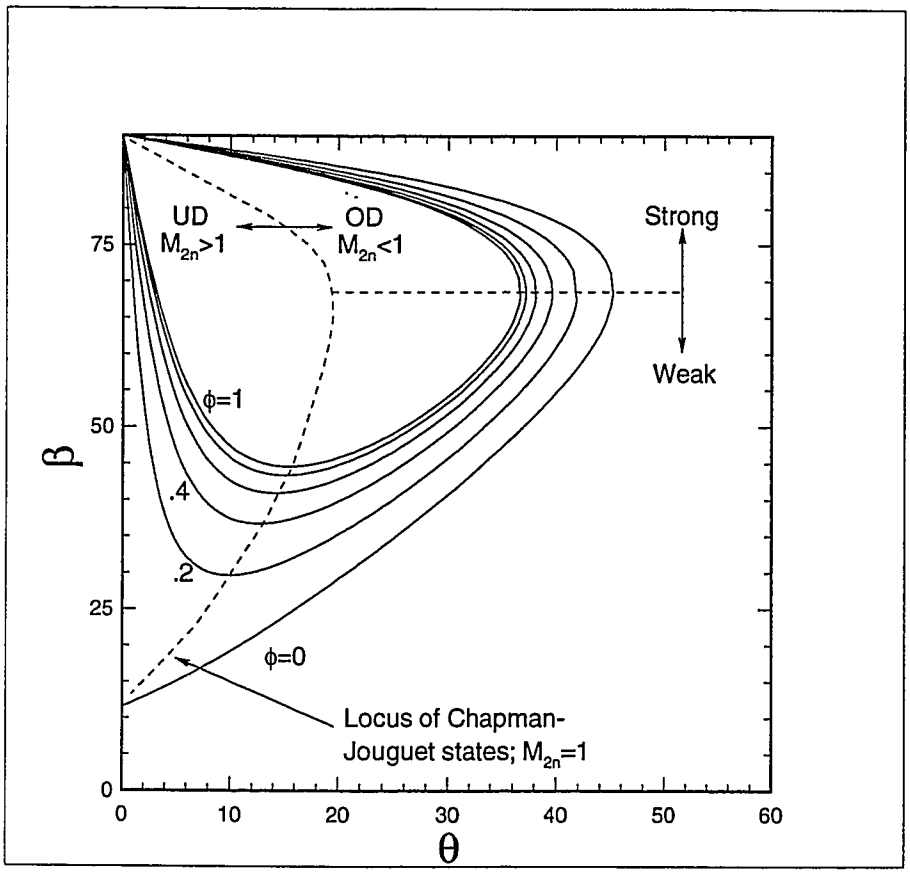

Figure 3.1: Variation of Oblique Shock Wave Angle β with Turning Angle θ for Variable Equivalence Ratio ϕ (hydrogen-air at $555^{o}K$, 1 atm, Mach 5).

the interface between the underdriven and overdriven regimes. These are called the Chapman-Jouguet (or C-J) states since, as in a free running normal detonation, the exiting normal flow is sonic ($M_{2n} = 1$). For a specific value of equivalence ratio, the C-J point represents the minimum turning angle, θ_{cj}, for which stable heat release due to chemical reaction can occur.

Implicit in this analysis is the assumption that chemical heat release occurs entirely within the coupled wave. To be generally true, this would require infinite rate chemistry. Chemical rates are always finite, yet may appear infinitely fast relative to a low speed fluid dynamical process. A better measure of relative chemical rates is

the Damköhler number,

$$Da = t_{fluid}/t_{chem} \tag{3.12}$$

Here t_{fluid} is the fluid residence time and t_{chem} is a representative chemical time scale. In the case of ODW's t_{chem} would be the post-shock chemical induction time (ignition delay) and t_{res} would be the transit time through the post-shock domain. Should t_{chem} be much larger than t_{res} (thus $Da \ll 1$) the shock and combustion waves may not couple to form an ODW, despite what is indicated on the stability plot (Figure 3.1). Considering the range of Da, potential results may be grouped as in Table 3.1.

Table 3.1: Effect of Damköhler number (Da) on the Formation of an ODW

$Da \ll 1$	no ignition
$Da \sim 1$	shock-induced combustion
$Da \gg 1$	ODW

In addition to finite rate chemistry, viscous processes, in particular wall boundary layers, may also contribute to the formation of ODW's [11]. In summary, a stability plot such as Figure 3.1 indicates only possible end states for a flow configuration; the accurate prediction of what will occur depends on the complex interaction of gas dynamic, chemical-kinetic and viscous phenomena. Moreover, the coupled nature of these processes eliminates the use of analytical tools or even piecemeal numerical treatment [8]. The only practical solution is given by a multi-dimensional numerical model that includes all the dominant physical processes.

3.2 Conical Geometry

The theory for conical ODW's is discussed by several authors [20, 21, 22]. The conical ODW differs from the planar ODW only by the presence of the conical flow field between the wave and the cone surface. Since the conical ODW can be treated locally as a planar wave, the theory developed for planar ODWs can be used to solve for the jump conditions. Once calculated, the jump conditions can be used to

initialize the conical flow, or Taylor-Maccoll solution. From [19] the equations for the Taylor-Maccoll solution are,

$$\frac{d\bar{v}}{d\psi} = -\bar{u} + \frac{c^2(\bar{u} + \bar{v}cot\psi)}{\bar{v}^2 - c^2} \tag{3.13}$$

$$\frac{d\bar{u}}{d\psi} = \bar{v} \tag{3.14}$$

where $\bar{u}$ and $\bar{v}$ are velocity components parallel, and normal to, a ray emanating from the vertex of the cone. c is the sound speed and ψ is the angle of the ray from the cone centerline. Equations (3.13) and (3.14) are given here to call attention to the singularity at sonic velocity. To avoid dealing with this singularity, the stability plot calculated for conical ODWs was limited to overdriven waves. Frozen flow was assumed downstream of the ODW where the actual flow undergoes shifting equilibrium in the conical flow. However this is a reasonable assumption considering the small additional pressure change there. The appearance of the conical plot in Figure 3.2 is similar to that for the planar geometry, just shifted in turning angle to reflect the additional angle that the flow is turned through between the ODW and cone surface.

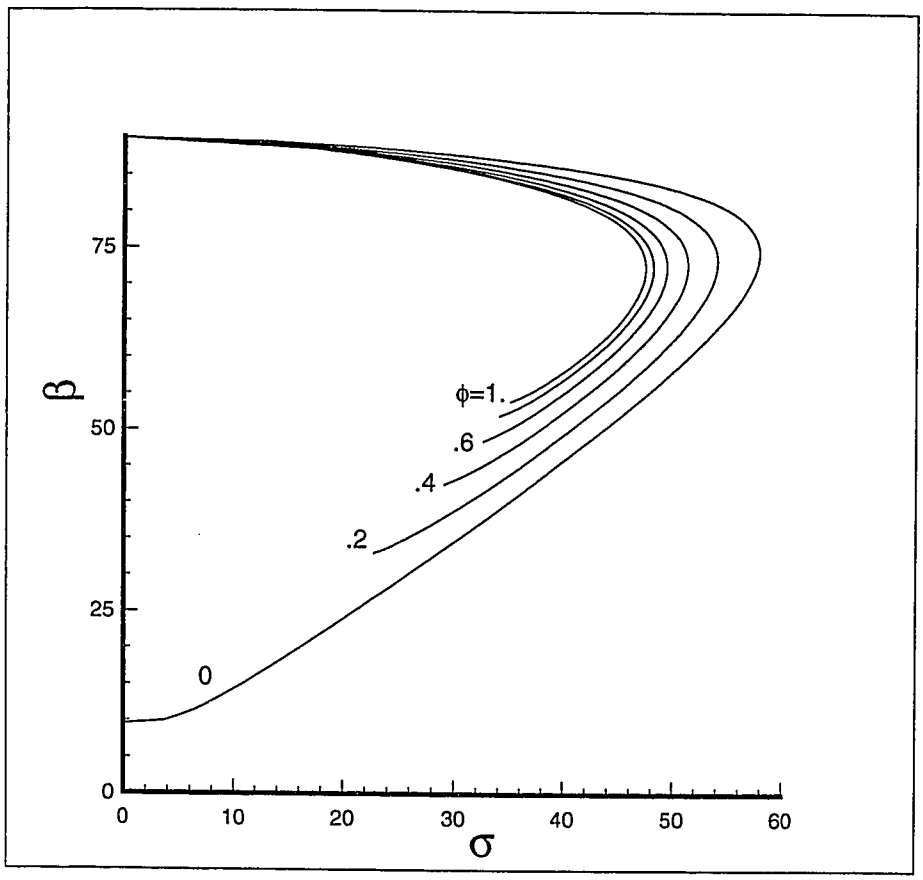

Figure 3.2: Variation of Oblique Shock Wave Angle β with Cone Half-Angle σ for Variable Equivalence Ratio ϕ (hydrogen-air at $800^{o}K$, 1 atm, Mach 5).

Chapter 4

FINITE-DIFFERENCE MODEL

The finite-difference model used in this work solves the two-dimensional, "thin-layer", Navier-Stokes equations for a reactive gas mixture. It is second order accurate overall, using Runge-Kutta integration in time and Yee's improved upwind scheme [23, 24] for the spatial derivatives. The chemical and viscous source terms are incorporated using operator splitting.

This chapter presents a detailed description of the numerical model. The exact form of the equations is given first. This is followed by a description of the finite difference solution scheme, chemical kinetic integrator and thermochemical and transport properties calculations.

4.1 Governing Equations

Two coordinate geometries are considered, planar and axisymmetric. Derivations of the governing equations for both are included in Appendix A. Expressed in generalized, non-orthogonal coordinates and a geometry dependent parameter, β, the two-dimensional, "thin-layer", Navier-Stokes equations for a reacting mixture of N species are,

$$\frac{\partial Q}{\partial t} + \frac{\partial F_i}{\partial \xi} + \frac{\partial G_i}{\partial \eta} = \beta S_1 + \frac{\partial S_2}{\partial \eta} + S_3 \tag{4.1}$$

where Q is the vector of conserved variables,

$$Q = J^{-1} \begin{bmatrix} \rho_1 \\ \rho_2 \\ \vdots \\ \rho_N \\ \rho u \\ \rho v \\ E \end{bmatrix} \tag{4.2}$$

and F_i and G_i are the inviscid components of the flux vectors,

$$F_i = J^{-1} \begin{bmatrix} \rho_1 U \\ \rho_2 U \\ \vdots \\ \rho_N U \\ \rho u U + \xi_x p \\ \rho v U + \xi_y p \\ U(E+p) \end{bmatrix} \tag{4.3}$$

$$G_i = J^{-1} \begin{bmatrix} \rho_1 V \\ \rho_2 V \\ \vdots \\ \rho_N V \\ \rho u V + \eta_x p \\ \rho v V + \eta_y p \\ V(E+p) \end{bmatrix} \tag{4.4}$$

Axisymmetric and viscous components are contained in the source terms, S_1 and S_2,

$$S_1 = -\frac{J^{-1}}{x} \begin{bmatrix} \rho_1 u \\ \rho_2 u \\ \vdots \\ \rho_N u \\ \rho u^2 \\ \rho u v \\ u(E+p) \end{bmatrix} \tag{4.5}$$

$$S_2 = J^{-1}\begin{bmatrix} 0 \\ 0 \\ \vdots \\ 0 \\ \mu(\eta_x^2+\eta_y^2)u_\eta + \frac{\mu}{3}[\eta_x(3u_\eta - 2x^{-\beta}(x^\beta u)_\eta) + \eta_y v_\eta]\eta_x \\ \mu(\eta_x^2+\eta_y^2)v_\eta + \frac{\mu}{3}[\eta_x(3u_\eta - 2x^{-\beta}(x^\beta u)_\eta) + \eta_y v_\eta]\eta_y \\ (\eta_x^2+\eta_y^2)\left[\frac{\mu}{2}(u^2+v^2)_\eta + kT_\eta\right] + \frac{\mu}{3}(\eta_x u + \eta_y v)[\eta_x(3u_\eta - 2x^{-\beta}(x^\beta u)_\eta) + \eta_y v_\eta] \end{bmatrix} \tag{4.6}$$

where the geometry dependent parameter β is,

$$\beta = \begin{cases} 0 & \text{for planar geometry} \\ 1 & \text{for axisymmetric geometry} \end{cases} \tag{4.7}$$

The third source term incorporates species formation and destruction through chemical kinetics,

$$S_3 = J^{-1}\begin{bmatrix} \dot{\rho}_1 \\ \dot{\rho}_2 \\ \vdots \\ \dot{\rho}_N \\ 0 \\ 0 \\ 0 \end{bmatrix} \tag{4.8}$$

For planar geometry, x, y, u and v are defined as usual. For axisymmetric geometry, $x = r$, $y = z$, $u = v_r$ and $v = v_z$. Subscripts x and y in equations (4.3), (4.4) and (4.6) denote partial differentiation with respect to the physical coordinates. Likewise, subscripts ξ and η denote partial differentiation with respect to the transformed coordinates.

It is a common practice to express the governing equations in dimensionless form. Oran and Boris [25] recommend using dimensional equations for simplicity and ease of debugging and interpreting complex, reactive flow simulations. This advice is followed here.

Terms that are a consequence of the transformation to non-orthogonal curvilinear coordinates include J^{-1}, the inverse of the transformation Jacobian,

$$J^{-1} = \begin{vmatrix} x_\xi & x_\eta \\ y_\xi & y_\eta \end{vmatrix} = x_\xi y_\eta - x_\eta y_\xi \tag{4.9}$$

the grid metrics, ξ_x, ξ_y, η_x and η_y,

$$\xi_x = y_\eta J\ , \quad \eta_x = -y_\xi J\ , \quad \xi_y = -x_\eta J\ , \quad \eta_y = x_\xi J \tag{4.10}$$

and the contravariant velocities, U and V,

$$U = \xi_x u + \xi_y v\ , \quad V = \eta_x u + \eta_y v \tag{4.11}$$

In (3.2) through (3.6), ρ_i is the mass density of species i, ρ is the mixture mass density, and is equal to the sum of the individual species mass densities,

$$\rho = \sum_{i=1}^{N} \rho_i \tag{4.12}$$

u and v are the cartesian fluid velocities and E is the total energy per unit volume,

$$E = \rho \left[\varepsilon + \frac{1}{2} \left(u^2 + v^2 \right) \right] \tag{4.13}$$

The specific internal energy of the mixture, ε, is calculated as the mole weighted sum of the internal energies of the individual species,

$$\varepsilon = \left(\sum_{i=1}^{N} \sigma_i \bar{e}_i \right) / \sigma_m \tag{4.14}$$

where, σ_i is the mass specific mole number for species i,

$$\sigma_i = \frac{\rho_i}{\rho M W_i} \tag{4.15}$$

their sum being equal to the inverse of the mixture molecular weight,

$$\sigma_m = \sum_{i=1}^{N} \sigma_i = 1/MW \tag{4.16}$$

Each specie's internal energy includes sensible and chemical contributions,

$$\bar{e}_i = \bar{e}^{\circ}_{fi} + \int_{T_o}^{T} \bar{C}_{v_i} dT \tag{4.17}$$

where the formation internal energy for species i, e°_{fi} is equal to the formation enthalpy, h°_{fi}, and T_o is $298^{\circ}K$.

Closure requires an equation of state, in this case the multispecies ideal gas law,

$$p = \sum_{i=1}^{N} \sigma_i \rho R_u T \tag{4.18}$$

or equivalently

$$p = \sum_{i=1}^{N} \frac{\rho_i}{MW_i} R_u T \tag{4.19}$$

Only the laminar form of the equations are considered. A turbulent model is not used since the viscous features of interest (viscous dissipation at wall boundaries, subsonic region in boundary layer) are present in a simple laminar model. However, to the extent that the thickness of the wall boundary layer effects predictions for turbulent flows, this represents a limitation in the current model. The mixture molecular viscosity, μ, and conductivity, k, are computed from the individual species values as described in Section 4.5.

4.2 Convective Algorithm

The convective algorithm is second order accurate overall and TVD (total variation diminishing). The implementation generally follows that of Cambier, Adelman and Menees [10]; the major difference is a finite volume formulation in the reference, whereas the present algorithm uses a finite difference formulation.

4.2.1 Spatial Differencing

Beyond the basic monotone solution schemes, there exist a class of *high-resolution* solution methods for hyperbolic conservation laws (FCT, MUSCL, ENO, PPM to name a few). Monotone schemes are necessarily first order to correctly treat discontinuities, but unfortunately are first order everywhere. High-resolution schemes use a hybrid approach where discontinuities are still treated with the basic monotone

scheme, but higher order accuracy is maintained throughout the remainder of the flow field. Roe [26] gives a concise explanation of the general approach. In flux limiter parlance, the diffusive flux imposed by the monotone scheme is reduced or "limited" to that of say, a second order accurate representation of the differential equation (e.g. Lax-Wendroff). Note that methods with greater than second order accuracy have been developed (one extreme example being 16th order FCT), but these are very specialized.

Of the available high-resolution schemes, Yee's second order accurate improved upwind TVD scheme is used in this work [23, 24, 27]. This is actually a refinement of the original second order accurate TVD scheme developed by Harten [28]. The interested reader should consult these references for a complete description, as only the essential details are described here.

Begin by noting that equation (4.1) can be rewritten as,

$$\frac{\partial Q}{\partial \tau} + A\frac{\partial Q}{\partial \xi} + B\frac{\partial Q}{\partial \eta} = rhs \tag{4.20}$$

where A and B are the *flux Jacobians*. These terms will be used shortly.

The finite difference form of (3.1) is written in terms of central differencing of a modified flux,

$$\Delta_t Q = -\bar{\delta}_\xi \tilde{F} - \bar{\delta}_\eta \tilde{G} \tag{4.21}$$

where Δ_t, δ_ξ and δ_η are finite difference operators. Δ_t denotes forward differencing in time while δ_ξ and δ_η denote central differencing in the ξ coordinate direction. The overbars on the central difference operators signify differences over the cell interfaces $(j \pm 1/2, k \pm 1/2)$ rather than at cell centers $(j \pm 1, k \pm 1)$. Since $\Delta\xi$ and $\Delta\eta$ are unity for generalized coordinates,

$$\begin{aligned} \bar{\delta}_\xi \tilde{F}_{j,k} &= (\tilde{F}_{j+1/2,k} - \tilde{F}_{j-1/2,k}) \\ \bar{\delta}_\eta \tilde{G}_{j,k} &= (\tilde{G}_{j,k+1/2} - \tilde{G}_{j,k-1/2}) \end{aligned} \tag{4.22}$$

The interface fluxes $\tilde{F}$ and $\tilde{G}$ are estimated as the average of adjacent nodal flux values plus a correction term,

$$\tilde{F}_{j+1/2,k} = \frac{1}{2}[F_{j+1} + F_{j,k} + (X_A \Phi)_{j+1/2,k}]$$

$$\tilde{F}_{j-1/2,k} = \frac{1}{2}[F_{j-1} + F_{j,k} + (X_A\Phi)_{j-1/2,k}] \tag{4.23}$$

$$\tilde{G}_{j,k+1/2} = \frac{1}{2}[G_{k+1} + G_{j,k} + (X_B\Phi)_{j,k+1/2}]$$

$$\tilde{G}_{j,k-1/2} = \frac{1}{2}[G_{k-1} + G_{j,k} + (X_B\Phi)_{j,k-1/2}]$$

The correction terms $X_A\Phi$ and $X_B\Phi$ are the spectral decomposition of the A and B flux Jacobians, multiplied by the difference in conserved quantities over the corresponding cell interfaces. This is clear in the first order case,

$$(X_A\Phi)_{j+1/2,k} = -(X_A|\Lambda_A|_A X_A^{-1})_{j+1/2,k}\left(\frac{(JQ)_{j+1,k} - (JQ)_{j,k}}{\frac{1}{2}(J_{j+1,k} + J_{j,k})}\right)$$

$$(X_B\Phi)_{j,k+1/2} = -(X_B|\Lambda_A|_B X_B^{-1})_{j,k+1/2}\left(\frac{(JQ)_{j,k+1} - (JQ)_{j,k}}{\frac{1}{2}(J_{j,k+1} + J_{j,k})}\right) \tag{4.24}$$

$$(X_A\Phi)_{j-1/2,k} = +(X_A|\Lambda_B|_A X_A^{-1})_{j-1/2,k}\left(\frac{(JQ)_{j-1,k} - (JQ)_{j,k}}{\frac{1}{2}(J_{j-1,k} + J_{j,k})}\right)$$

$$(X_B\Phi)_{j,k-1/2} = +(X_B|\Lambda_B|_B X_B^{-1})_{j,k-1/2}\left(\frac{(JQ)_{j,k-1} - (JQ)_{j,k}}{\frac{1}{2}(J_{j,k-1} + J_{j,k})}\right)$$

where X and Λ are the eigenvector and eigenvalue matrices for a specific flux Jacobian. The second order relationship prescribed for Yee's improved upwind scheme is much more complicated. The term $(X_A\Phi)_{j+1/2,k}$ becomes,

$$(X_A\Phi)_{j+1/2,k} = X_A[\psi(\lambda_{j+1/2,k})(g_{j,k} + g_{j+1}) - \psi(\lambda_{j+1/2,k} + \gamma_{j+1/2,k})\alpha_{j+1/2,k}] \tag{4.25}$$

where λ are the eigenvalues at the cell interface,

$$\lambda_{j+1/2,k} = Diag(\Lambda_{j+1/2,k}) \tag{4.26}$$

and α is the interface-centered characteristic difference, which must include the change in the transformation Jacobian over the interface,

$$\alpha_{j+1/2,k} = X^{-1}_{j+1/2,k}\left(\frac{(JQ)_{j+1,k} - (JQ)_{j,k}}{\frac{1}{2}(J_{j+1,k} + J_{j,k})}\right) \tag{4.27}$$

The remaining terms in equation (4.25) include the flux limiter,

$$g_{j,k} = S_{j+1/2,k} \cdot max[0, min(|\sigma_{j+1/2,k}\alpha_{j+1/2,k}|, S_{j+1/2,k} \cdot \sigma_{j-1/2,k}\alpha_{j-1/2,k})] \quad (4.28)$$

where,

$$\sigma_{j+1/2,k} = \frac{1}{2}[\psi(\lambda_{j+1/2,k}) - (\lambda_{j+1/2,k})^2] \quad (4.29)$$

$$S_{j+1/2,k} = Sign(\alpha_{j+1/2,k}) \quad (4.30)$$

$$\gamma_{j+1/2,k} = \begin{cases} \frac{g_{j+1}-g_{j,k}}{\alpha_{j+1/2,k}} & \text{if } \alpha_{j+1/2,k} \neq 0 \\ 0 & \text{if } \alpha_{j+1/2,k} = 0 \end{cases} \quad (4.31)$$

and ψ is a coefficient of numerical viscosity,

$$\psi(z) = \begin{cases} |z| & \text{if } |z| \geq \epsilon \\ (z^2 + \epsilon^2)/2\epsilon & \text{if } |z| < \epsilon \end{cases} \quad (4.32)$$

where ϵ is typically 0.1 [28].

Although it is very difficult to follow what this scheme does, several observations can be made. First, when all elements of the flux limiter, g, are zero, equation (4.25) reduces to the first order case. Since α represents the slope between nodal points, g is seen to reduce to zero at minimums and maximums. The result is that the monotone differencing scheme is activated to cancel oscillations. Away from extremum, nonzero values of g act to reduce the effective dissipation of the monotone scheme to give desired higher order accuracy. Secondly, ψ is a smoothing operator that modifies the argument in parenthesis (represented by the dummy variable z in (4.32)) such that the slope is continuous as $z \rightarrow 0$. Finally, equation (4.25) suggests the need for g_{j+1}. Because of our definition for g (equation (4.28)), this requires $\alpha_{j+3/2}$ which in turn requires nodal data at $j+1$ and $j+2$. Similar logic for $\Phi_{j-1/2,k}$ shows the need for data at $j-1$ and $j-2$. Thus it is evident that this is a *5-point scheme* as opposed to the *3-point scheme* used for the first order case.

Lastly, expressions for the eigenvector matrices X, X^{-1} and eigenvalues λ are required. Cambier, Adelman and Menees [10] give the form of these matrices, but with incomplete definitions of all the terms, especially the pressure derivatives. This

journal article was also printed with an astounding number of typographical errors. Therefore, derivations of these matrices were checked and the complete form of all terms was developed. The results are summarized below and are included in detail in Appendix A. These derivations confirmed Cambier, et al's forms for X and X^{-1}. Since this initial work on the model was completed, Shuen, Liou and van Leer [29] have published a similar derivation of these terms.

Eigenvalues and eigenvector matrices for the A flux Jacobian are

$$\Lambda_A = \begin{bmatrix} U & \cdots & 0 & 0 & 0 & 0 \\ \vdots & \ddots & \vdots & \vdots & \vdots & 0 \\ 0 & \cdots & U & 0 & 0 & 0 \\ 0 & \cdots & 0 & U & 0 & 0 \\ 0 & \cdots & 0 & 0 & U + c\sqrt{\xi_x^2 + \xi_y^2} & 0 \\ 0 & \cdots & 0 & 0 & 0 & U - c\sqrt{\xi_x^2 + \xi_y^2} \end{bmatrix} \tag{4.33}$$

$$X_A = \begin{bmatrix} 1 & \cdots & 0 & 0 & c_1 & c_1 \\ \vdots & \ddots & \vdots & \vdots & \vdots & \vdots \\ 0 & \cdots & 1 & 0 & c_N & c_N \\ u & \cdots & u & \xi_y' & u + \xi_x' c & u - \xi_x' c \\ v & \cdots & v & -\xi_x' & v + \xi_y' c & v - \xi_y' c \\ u^2 + v^2 - \frac{P_{\rho 1}}{P_E} & \cdots & u^2 + v^2 - \frac{P_{\rho N}}{P_E} & \xi_y' u - \xi_x' v & H + cU' & H - cU' \end{bmatrix} \tag{4.34}$$

The inverse eigenvector matrix is

$$X_A^{-1} =$$

$$\begin{bmatrix} 1 - \frac{c_1}{c^2} P_{\rho_1} & \cdots & -\frac{c_1}{c^2} P_{\rho_N} & u\frac{c_1}{c^2} P_E & v\frac{c_1}{c^2} P_E & -\frac{c_1}{c^2} P_E \\ \vdots & \ddots & \vdots & \vdots & \vdots & \vdots \\ -\frac{c_N}{c^2} P_{\rho_1} & \cdots & 1 - \frac{c_N}{c^2} P_{\rho_N} & u\frac{c_N}{c^2} P_E & v\frac{c_N}{c^2} P_E & -\frac{c_N}{c^2} P_E \\ -\xi_y' u + \xi_x' v & \cdots & -\xi_y' u + \xi_x' v & \xi_y' & -\xi_x' & 0 \\ (P_{\rho 1} - cU')/2c^2 & \cdots & (P_{\rho 1} - cU')/2c^2 & (\xi_x' c - u P_E)/2c^2 & (\xi_y' c - v P_E)/2c^2 & P_E/2c^2 \\ (P_{\rho 1} + cU')/2c^2 & \cdots & (P_{\rho 1} + cU')/2c^2 & -(\xi_x' c + u P_E)/2c^2 & -(\xi_y' c + v P_E)/2c^2 & P_E/2c^2 \end{bmatrix} \tag{4.35}$$

In (4.34) and (4.35) c_i is the mass fraction of species i, and primes denote the normalized quantities,

$$\xi'_x = \frac{\xi_x}{\sqrt{\xi_x^2 + \xi_y^2}}, \quad \xi'_y = \frac{\xi_y}{\sqrt{\xi_x^2 + \xi_y^2}} \tag{4.36}$$

$$U' = \xi'_x u + \xi'_y v$$

Note that the eigenvalue matrix Λ does not use normalized quantities and that properties at the cell interface are required in X, Λ and X^{-1}. Although Roe prescribes a special form of density weighted averaging for this purpose, arithmetic averaging is usually satisfactory and is more efficient. Arithmetic averaging is used in the present formulation.

Similarly, matrices for the B flux Jacobian are

$$\Lambda_B = \begin{bmatrix} V & \cdots & 0 & 0 & 0 & 0 \\ \vdots & \ddots & \vdots & \vdots & \vdots & 0 \\ 0 & \cdots & V & 0 & 0 & 0 \\ 0 & \cdots & 0 & V & 0 & 0 \\ 0 & \cdots & 0 & 0 & V + c\sqrt{\eta_x^2 + \eta_y^2} & 0 \\ 0 & \cdots & 0 & 0 & 0 & V - c\sqrt{\eta_x^2 + \eta_y^2} \end{bmatrix} \tag{4.37}$$

$$X_B = \begin{bmatrix} 1 & \cdots & 0 & 0 & c_1 & c_1 \\ \vdots & \ddots & \vdots & \vdots & \vdots & \vdots \\ 0 & \cdots & 1 & 0 & c_N & c_N \\ u & \cdots & u & \eta'_y & u + \eta'_x c & u - \eta'_x c \\ v & \cdots & v & -\eta'_x & v + \eta'_y c & v - \eta'_y c \\ u^2 + v^2 - \frac{P_{p1}}{P_E} & \cdots & u^2 + v^2 - \frac{P_{pN}}{P_E} & \eta'_y u - \eta'_x v & H + cV' & H - cV' \end{bmatrix} \tag{4.38}$$

The inverse eigenvector matrix is

$$X_B^{-1} =$$

$$\begin{bmatrix} 1-\frac{c_1}{c^2}P_{\rho_1} & \cdots & -\frac{c_1}{c^2}P_{\rho_N} & u\frac{c_1}{c^2}P_E & v\frac{c_1}{c^2}P_E & -\frac{c_1}{c^2}P_E \\ \vdots & \ddots & \vdots & \vdots & \vdots & \vdots \\ -\frac{c_N}{c^2}P_{\rho_1} & \cdots & 1-\frac{c_N}{c^2}P_{\rho_N} & u\frac{c_N}{c^2}P_E & v\frac{c_N}{c^2}P_E & -\frac{c_N}{c^2}P_E \\ -\eta'_y u+\eta'_x v & \cdots & -\eta'_y u+\eta'_x v & \eta'_y & -\eta'_x & 0 \\ (P_{\rho 1}-cV')/2c^2 & \cdots & (P_{\rho 1}-cV')/2c^2 & (\eta'_x c-uP_E)/2c^2 & (\eta'_y c-vP_E)/2c^2 & P_E/2c^2 \\ (P_{\rho 1}+cV')/2c^2 & \cdots & (P_{\rho 1}+cV')/2c^2 & -(\eta'_x c+uP_E)/2c^2 & -(\eta'_y c+vP_E)/2c^2 & P_E/2c^2 \end{bmatrix} \tag{4.39}$$

where likewise normalized quantities are

$$\eta'_x = \frac{\eta_x}{\sqrt{\eta_x^2+\eta_y^2}}\,, \quad \eta'_y = \frac{\eta_y}{\sqrt{\eta_x^2+\eta_y^2}} \tag{4.40}$$

$$V' = \eta'_x u + \eta'_y v$$

Equations (4.33) through (4.35) and (4.37) through (4.39) require expressions for the speed of sound, c, and partial derivatives P_{ρ_i} and P_E. From the eigenvalue decomposition, the speed of sound is given by,

$$c^2 = \sum_{i=1}^{N} c_i P_{\rho i} + P_E(H-u^2-v^2) \tag{4.41}$$

where H is the enthalpy

$$H = (E+p)/\rho \tag{4.42}$$

and $P_{\rho i}$ and P_E are

$$P_{\rho i} = \frac{R_u T}{MW_i} + P_E[\frac{1}{2}(u^2+v^2) - \frac{1}{MW_i}(\int_{T_o}^{T} \bar{C}_{vi}dT + \bar{h^o_{fi}})] \tag{4.43}$$

$$P_E = R_u \sum_{i=1}^{N} \frac{\rho_i}{MW_i} / \sum_{i=1}^{N} \frac{\rho_i \bar{C}_{vi}}{MW_i} \tag{4.44}$$

Note that P_E reduces to the familiar single component, constant specific heat form

$$P_E = \gamma - 1 \tag{4.45}$$

where γ is the ratio of mixture specific heats, and substituting (4.43) and (4.44) into (4.41) gives the familiar relationship for the speed of sound,

$$c^2 = \frac{\gamma P}{\rho} \tag{4.46}$$

In reference [27, page 64], Yee notes that the frozen sound speed c defined in (4.41) "has no physical meaning." If this is to be taken literally, it is clearly an incorrect statement. Otherwise the sound speed as defined by (4.46) would likewise have no physical meaning, when in fact it does.

4.2.2 Time Differencing

Yee's improved upwind scheme gives second order spatial accuracy (away from discontinuities). This can be matched with a second order time stepping scheme to produce an overall second order algorithm. Second order accuracy in time is accomplished using modified Euler (second order Runge-Kutta) time differencing,

Step 1:

$$\bar{Q}_{j,k} = Q^n_{j,k} - \bar{\delta}_x \tilde{F}^n_{j,k} \tag{4.47}$$

Step 2:

$$Q^{n+1}_{j,k} = \frac{1}{2}(Q^n_{j,k} + \bar{Q}_{j,k}) - \frac{\Delta t}{2}\bar{\delta}_x \bar{\tilde{F}}^n_{j,k} \tag{4.48}$$

The first step is a first order predictor. The second step gives a second order correction based on the results of the first step and on values from the last time step.

The time step for this explicit finite difference scheme is limited by the Courant stability limit. For generalized coordinates, there is a Courant number associated with both the ξ and η coordinate directions,

$$\nu_\xi = \Delta t \left(U + c\sqrt{\xi_x^2 + \xi_y^2}\right) \tag{4.49}$$

$$\nu_\eta = \Delta t \left(U + c\sqrt{\eta_x^2 + \eta_y^2}\right) \tag{4.50}$$

The appropriate Courant number is the maximum of the two since the stability of the algorithm is directionally decoupled [30].

4.3 Operator Splitting

Source terms for finite rate chemistry and molecular transport, S_2 and S_3 in equation (3.1), are coupled into the finite difference solution using operator splitting. The

axisymmetric source term, S_1, is included in the second time step of the convective scheme. The procedure for each simulation time step is to first advance the convective solution by the second order time stepping procedure outlined above, followed by the addition of the viscous and chemical source terms source terms to the solution vector. The source term calculations are based on most recent data, i.e. that resulting from the convective solution.

Operator splitting is effective and is widely used because the most efficient solution procedure can be used for each source term. For example, a specialized chemical kinetic integrator can be used to efficiently compute S_3. Operator splitting also has a pair of limitations. First, the equations cannot be written, and solved, in conservative form. This can result in a failure to predict the correct jump conditions. Second, second order temporal accuracy is not maintained. Strictly speaking, the algorithm is second order accurate in time only for inviscid, non-reacting flow.

4.4 Thermodynamic Properties and Finite Rate Chemistry

Growth and decay of chemical species is modeled using traditional techniques for gas-phase chemical kinetics [31]. The set of nr one-step chemical reactions can be expressed notationally as,

$$\sum_{i=1}^{N} \nu'_{ji} M_i \underset{K_{bj}}{\overset{K_{fj}}{\rightleftharpoons}} \sum_{i=1}^{N} \nu''_{ji} M_i, \qquad j = 1, 2, \ldots, nr \tag{4.51}$$

where K_{fj} and K_{bj} are the forward and reverse rates for each reaction, M_i is the chemical symbol for species i, and ν'_{ji} and ν''_{ji} are the stoichiometric coefficients for the reactants and products of reaction j.

Rates are expressed in a modified Arrhenius form. For the forward reaction rate,

$$K_{fj} = A_j T^{n_j} \exp[-E_j/(R_u T)] \tag{4.52}$$

where values of the pre-exponential constant A_j, temperature exponent N_j, and the activation energy E_j must be experimentally determined. A reaction set together with these empirical constants is referred to as a chemical mechanism, and the one used in the present research is described in Section 4.4.2.

The chemical mechanism is related to rates of change of individual specie molar concentrations using the law of mass action. For each reaction j,

$$\frac{d(C_i)_j}{dt} = (\nu''_{ji} - \nu'_{ji}) \left[K_{fj} \prod_{i=1}^{N} C_i^{\nu'_{ji}} - K_{bj} \prod_{i=1}^{N} C_i^{\nu''_{ji}} \right]$$

$$i = 1, 2, \ldots, N \tag{4.53}$$

The net rate of change of concentration for each specie is then given by summing over all reactions,

$$\frac{dC_i}{dt} = \sum_{j=1}^{nr} \frac{d(C_i)_j}{dt} \tag{4.54}$$

Finally, multiplication by the molecular weight results in the change in specie density required in equation (4.8).

$$\frac{d\rho_i}{dt} = MW_i \frac{dC_i}{dt} \tag{4.55}$$

Changes in concentrations reacting species are calculated by integrating the coupled set of ordinary differential equations defined in equation (4.53) for each computational grid point in the flow, at every time step in the simulation. Typically thousands of initial value problems are being solved at each time step, which can dominate the CPU time if done inefficiently. An operator split approach is taken in the present solution algorithm. This enables the use of specialized and highly efficient software to compute the changes in the chemical species. This does mean that the physics are artificially decoupled; however, the Courant limited time steps are so small that the result is still a good representation of the coupled system. The finite rate chemistry software package is described next, followed by the details of the chemical mechanism used in this research.

4.4.1 CFDK

The thermochemical properties management and integration of the chemical rate equations is accomplished with the special purpose program CFDK, written by Pratt (an improved version of CVK1 [32]). The integrator is a fast, automatic solver for homogeneous, gas-phase chemical kinetic equations. It uses an exponentially-fitted trapezoidal method. The two-part predictor-corrector algorithm includes filtering of ill-posed initial conditions and automatic stepsize control. While Newton-Raphson

iteration is an available option, Jacobi-Newton iteration is used exclusively in this version because of the small time steps dictated by the convective flow solver.

The thermochemical properties manager in CFDK computes temperature dependent specific heats for the gas mixture. Curve fit coefficients for the temperature range of 300 to 5000°K have been produced for 421 pure species by NASA Lewis [33] and these data are easily incorporated into the CFDK data file for species of interest. Curve fits for specific heat of species i are polynomials of the form,

$$\frac{C_{p_i}}{R_u} = a + bT + cT^2 + dT^3 + eT^4 \tag{4.56}$$

which can be easily integrated to compute enthalpy,

$$\frac{\bar{h}_i}{R_u T} = a + \frac{bT}{2} + \frac{cT^2}{3} + \frac{dT^3}{4} + \frac{eT^4}{5} + \frac{\bar{h}_f^o - \bar{h}_{T_{ref}}}{R_u T} \tag{4.57}$$

Also, since $R_u = C_p - C_v$, the constant volume specific heat and internal energy can be readily computed as,

$$\frac{C_{v_i}}{R_u} = \frac{C_{p_i}}{R_u} - 1 \tag{4.58}$$

$$\frac{\bar{e}_i}{R_u T} = \frac{\bar{h}_i}{R_u T} - 1 \tag{4.59}$$

These values are used in equation 4.17.

For high-speed viscous flow calculations, species transport properties are also required. Of the 421 pure species for which specific heat data is available, 155 gaseous species have also been included in data sets for viscosity and thermal conductivity. This reduced list is given in Table 4.1. The use of the transport property data set is described below in Section 4.5.

4.4.2 Hydrogen - Air Kinetic Mechanisms

The combustion of hydrogen with air is, perhaps, the simplest fuel-oxidizer combination possible. This is especially true when reactions with nitrogen can be neglected. The reactions are well understood (see, for example [31]) and individual rates are well known. A number of chemical mechanisms have been proposed that vary mainly in the number of species modeled [5, 8, 34].

Table 4.1: List of Gaseous Chemical Species[1] for Which Temperature Dependent Thermodynamic and Transport Properties are Included

Al	$BeCl_2$	CO	ClF_3	I_2	N_2O_4	PS
AlCl	BeF	CoS	ClO	Li	Na	P_2
$AlCl_3$	BeF_2	CO_2	Cl_2	LiCl	NaBr	P_4
AlF	BeI_2	CP	F	LiF	NaCN	S
AlF_3	Br	CS	FCN	LiO	NaCl	SF_6
AlN	Br_2	CS_2	FO	Li_2	NaF	SH
AlO	C	C_2	F_2	Li_2O	NaI	SO
AlS	CCl	C_2H_2	F_2O	Mg	NaO	SO_2
Al_2	CCl_2	C_2H_4	H	MgCl	NaOH	S_2
Ar	CCl_2F_2	C_2H_6	HBr	$MgCl_2$	Na_2	S_2F_2
B	CCl_3	C_2H_5OH	HCN	MgF	Na_2O	Si
BCl	CCl_3F	C_2N_2	HCl	MgF_2	Ne	SiCl
BCl_2	CCl_4	C_3H_6	HF	Mg_2	O	$SiCl_4$
BCl_3	CF	C_3H_8	HI	N	OH	SiF
BF	CF_2	C_3H_7OH	H_2	NF_3	O_2	SiF_4
BF_2	CF_3	I-C_4H_{10}	H_2O	NH	P	SiH_4
BF_3	CF_4	N-C_4H_{10}	H_2O_2	NH_3	PCl_3	SiO
BO	CH	C_6H_6	H_2S	NO	PF	SiO_2
B_2	CH_3Cl	Cd	He	NOCl	PF_3	SiS
B_2O_3	CH_3OH	Cl	Hg	NO_2	PH_3	Si_2
Be	CH_4	ClCN	$HgBr_2$	N_2	PN	$SnCl_4$
$BeBr_2$	CN	ClF	I	N_2O	PO	Zn
BeCl						

[1] Fuels in this table include methanol (CH_3OH), acetylene (C_2H_2), ethylene (C_2H_4), ethane (C_2H_6), ethanol (C_2H_5OH), cyanogen (C_2N_2), cyclopropane (C_3H_6), propane (C_3H_8), 1-propanol (C_3H_7OH), isobutane (I-C_4H_{10}), *n*-butane (N-C_4H_{10}), benzene (C_6H_6).

The hydrogen-air chemical mechanism used in the present research is due to Westbrook [8]. It models 8 species (H_2,O_2,O,H,OH,HO_2,H_2O_2,H_2O) in 17 reaction steps. Westbrook's mechanism represents a middle ground between the simplified version (7 species in 8 reaction steps) of Waldman et al.[34], and the detailed mechanism (13 species in 33 reaction steps) of Jackimowski[5]. The complexity of Jachimowski's model is due to the inclusion of oxides of nitrogen. This level of detail can be avoided in the present research because of the small time scales associated with detonations. Diatomic nitrogen, which forms oxides on relatively long time scales, is simply included as a non-reactive diluent. Westbrook's chemical mechanism is given in Table 4.2.

4.5 Transport Properties

Values of molecular viscosity and thermal conductivity for the gas mixtures are computed as functions of local temperature and species mass fractions. The methodology and curve fit data used are those of Gordon, McBride and Zeleznik [35].

Mixture viscosity is calculated from individual species viscosities using a relationship first proposed by Sutherland [36],

$$\mu_{mix} = \sum_{i=1}^{N} \frac{x_i \mu_i}{x_i + \sum_{\substack{j=1 \\ j \neq i}}^{N} x_j \phi_{ij}} \tag{4.60}$$

where x_i is the mole fraction of species i and ϕ_{ij} is the viscosity interaction coefficient between species i and j.

The relationship for thermal conductivity was first proposed by Wassiljewa [37] and is identical except that k replaces μ and ψ replaces ϕ,

$$k_{mix} = \sum_{i=1}^{N} \frac{x_i k_i}{x_i + \sum_{\substack{j=1 \\ j \neq i}}^{N} x_j \psi_{ij}} \tag{4.61}$$

In this case ψ is the frozen-thermal-conductivity interaction coefficient between species i and j.

Gordon, McBride and Zeleznik discuss many options for the interaction coefficients ϕ_{ij} and ψ_{ij}, all of which gave reasonable agreement with experimental data. The relationship proposed by Wilke [38] was chosen for ϕ_{ij},

Table 4.2: Westbrook's Hydrogen Oxidation Mechanism. cm^3-mole-sec-kcal units, $K = AT^n \exp(-E/R_uT)$.

	Reaction	Forward rate			Reverse rate		
		$\log A$	n	E	$\log A$	n	E
1	$H + O_2 \rightarrow O + OH$	14.27	0	16.79	13.17	0	0.68
2	$H_2 + O \rightarrow H + OH$	10.26	1	8.90	9.92	1	6.95
3	$H_2O + O \rightarrow OH + OH$	13.53	0	18.35	12.50	0	1.10
4	$H_2O + H \rightarrow H_2 + OH$	13.98	0	20.30	13.34	0	5.15
5	$H_2O_2 + OH \rightarrow H_2O + HO_2$	13.00	0	1.80	13.45	0	32.79
6	$H_2O + M \rightarrow H + OH + M$	16.34	0	105.00	23.15	-2	0.00
7	$H + O_2 + M \rightarrow HO_2 + M$	15.22	0	-1.00	15.36	0	45.90
8	$HO_2 + O \rightarrow OH + O_2$	13.70	0	1.00	13.81	0	56.61
9	$HO_2 + H \rightarrow OH + OH$	14.40	0	1.90	13.08	0	40.10
10	$HO_2 + H \rightarrow H_2 + O_2$	13.40	0	0.70	13.74	0	57.80
11	$HO_2 + OH \rightarrow H_2O + O_2$	13.70	0	1.00	14.80	0	73.86
12	$H_2O_2 + O_2 \rightarrow HO_2 + HO_2$	13.60	0	42.64	13.00	0	1.00
13	$H_2O_2 + M \rightarrow OH + OH + M$	17.08	0	45.50	14.96	0	-5.07
14	$H_2O_2 + H \rightarrow HO_2 + H_2$	12.23	0	3.75	11.86	0	18.70
15	$O + H + M \rightarrow OH + M$	16.00	0	0.00	19.90	-1	103.72
16	$O_2 + M \rightarrow O + O + M$	15.71	0	115.00	15.67	-0.28	0.00
17	$H_2 + M \rightarrow H + H + M$	14.34	0	96.00	15.48	0	0.00

$$\phi_{ij} = \frac{1}{4}\left(\frac{2MW_j}{MW_i + MW_j}\right)^{1/2}\left[1 + \left(\frac{\mu_i}{\mu_j}\right)^{1/2}\left(\frac{MW_j}{MW_i}\right)^{1/4}\right]^2 \tag{4.62}$$

where MW_i and MW_j are the molecular weights of species i and j. The combination of equations 4.60 and 4.62 is commonly referred to as Wilke's mixing law.

Vanderslice et al. [39] proposed an expression of identical form for ψ_{ij},

$$\psi_{ij} = \frac{1}{4}\left(\frac{2MW_j}{MW_i + MW_j}\right)^{1/2}\left[1 + \left(\frac{k_i}{k_j}\right)^{1/2}\left(\frac{MW_j}{MW_i}\right)^{1/4}\right]^2 \tag{4.63}$$

Equations 4.61 and 4.63 were used to compute values of frozen thermal conductivity for the mixture.

Individual species properties are calculated as a function of temperature from curve fits of the form,

$$\left.\begin{matrix}\ln\mu \\ \ln k\end{matrix}\right\} = A\ln T + \frac{B}{T} + \frac{C}{T^2} \tag{4.64}$$

In their transport database, Gordon, McBride and Zeleznik provide data for 155 pure gaseous species over the temperature range of 300 to 5000°K. Included in this database are curve-fit constants for 8 of the 9 species modeled for the hydrogen-air reaction (H_2, O_2, H, O, OH, H_2O_2, H_2O and N_2); unfortunately, the hydroperoxy radical (HO_2) is not included. Since HO_2 properties were not readily available, the approximation was made to use the property constants for hydrogen peroxide (H_2O_2) in their place.

Transport properties generated with these curve fits were compared with available table values as a check on the curve fit and software coding. Good agreement was obtained as shown in Table 4.3. A test performed for a gas mixture gave similar agreement as shown in Table 4.4.

For the present work, properties are updated at each grid point at every time step. An improvement in computational efficiency could easily be obtained by refreshing properties only when the change in temperature exceeds some preset limit.

4.6 Boundary Conditions

4.6.1 Supersonic Inflow/Outflow

For the supersonic inflow boundary condition, all data are supplied including mixture pressure, temperature, species composition and Mach number. These data are converted to the conserved variables and maintained constant throughout the simulation. The supersonic outflow boundary condition is achieved with a simple zeroth order extrapolation of data from the first row of cells upstream of the outflow boundary.

$$Q_{i,jmax} = Q_{i,jmax-1} \tag{4.65}$$

Table 4.3: Comparison of Curve Fit and Table Properties[1] for modeled species at 600°K.

	μ, μP		k, μW/cm°K	
species	code	table	code	table
H	109.6	-	3392	-
H_2	143.8	143	3017	3147
H_2O	213.8	206	464.8	421.2
HO_2	-	-	-	-
H_2O_2	116.2	-	253.9	-
N_2	295.5	291	444.8	455
O	327.6	-	638.1	-
OH	240.1	-	592.1	-
O_2	345.0	339	480.0	483

4.6.2 Planar Non-Penetrative

This boundary condition is used for inviscid wall boundaries where grid trajectories are orthogonal to the wall. For the algebraic grids generated this meant planar wall boundaries. This simple reflective boundary condition is applied by duplicating all properties except normal velocity at grid points equally-spaced on both sides of the boundary. The sign on the normal velocity in the interior point is set opposite that of the point in the flow. The result is that tangency is satisfied by effectively setting all first derivatives to zero across the boundary.

4.6.3 General Non-Penetrative

The general, non-planar wall boundary condition used for inviscid and viscous simulations is described in detail in [42]. The basic approach is to use the curvilinear metrics to compute normal and tangential velocity components at points adjacent to the wall boundary. For inviscid simulations, the tangential velocity is extrapolated to a grid point on the wall; for viscous simulations, the tangential velocity at the wall

[1] Table properties taken from Welty, Wicks and Wilson[40].

Table 4.4: Comparison of Model and Experimental Transport Properties[1] for a Gas Mixture at 1 atm and 293°K.

species/ mixture	μ μP	k μW/cm°K
CO_2	147.9	159.8
O_2	202.3	257.0
N_2	176.1	252.5
$0.133CO_2 + 0.039O_2 + 0.828N_2$	172.3	233.5
experiment	179.3	NA

is set to zero. Normal velocity is set to zero for both cases. Cartesian velocities are calculated along the wall for the inviscid case, then pressure at wall grid points is calculated from the normal momentum equation using an inversion of a tridiagonal system.

The process is readily implemented but caution must be used in selecting a grid. A clustered grid is recommended to reduce errors in the extrapolation process. This is especially important when trying to simulate expansion fans. However some degree of grid clustering is *required* to avoid gross errors at boundary points immediately downstream of a shock. The problem arises in the solution of the normal momentum equation for wall pressure. If the shock falls between the wall grid point and adjacent grid point in the flow, the wall pressure will be incorrect and the usual result is a failed solution. The problem can be avoided by clustering the grid such that downstream wall and adjacent grid points fall within the oblique shock angle. For hypersonic flows this can be a severe, but necessary, limitation.

4.6.4 Axisymmetric Centerline

The problem at the axisymmetric centerline is that the axisymmetric source term, S_1 becomes singular. Roache [43] prescribes a different set of equations for the centerline, and provides illustrations of why commonly used approximations are unsatisfactory.

[1] Test problem and experimental values taken from Bird, Stewart and Lightfoot[41, p. 25].

But for the sake of simplicity, this advise is not put into practice here. Instead, the approximation used for a centerline boundary is to use the general non-penetrative boundary condition just discussed, with small but finite minimum radius to avoid the singularity. This minimum radius was kept to a small fraction of the minimum grid spacing and was typically set to 1 μm.

Chapter 5

PLANAR RESULTS

This chapter presents a comparison of Rankine-Hugoniot analyses and two-dimensional finite-difference simulations for planar geometry. The canonical test problem is described first, followed by results of a parametric study which focused on the ODW formation mechanisms and properties.

5.1 Test Problem

The wedge flow test problem is that considered by Glenn and Pratt [9]: Mach 5 flow of a stoichiometric hydrogen-air mixture at $800°K$, 1 atm, into a 10 cm high combustion tunnel, with a 5.5 cm long compression ramp (or wedge) of varying ramp angle, starting 2.5 cm into the tunnel. The initial temperature and pressure were selected to insure that the induction time of the freestream is at least one order of magnitude greater than the convective time within the computational domain. The CJ Mach number for a hydrogen-air mixture at these conditions is 2.90, and the flow is therefore superdetonative.

Glenn and Pratt [9] used the Los Alamos code SALE2D [44] to perform a two-dimensional, time accurate, inviscid simulation. Their version of the code was modified to include adaptive gridding and finite rate chemical effects. The latter was achieved with a modified two-equation Korobeinikov induction model due to Oran et al. [45]. For a 20° wedge, a complete ODW is predicted. Their grid and results are shown in Figure 5.1.

5.2 Rankine-Hugoniot Analysis

A Rankine-Hugoniot analysis was performed for the planar test problem using the methodology discussed in Chapter 3. The results are shown in Figure 5.2. *If* an ODW forms, the 20° wedge angle and unit equivalence ratio require an attached, weak overdriven wave with an angle of 38.1° (the strong detonation would not occur

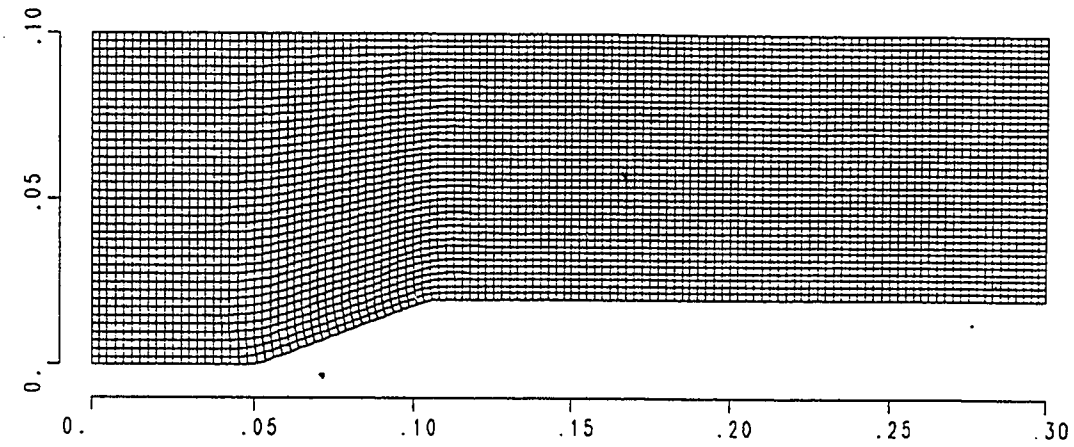

Initial 40x120 grid

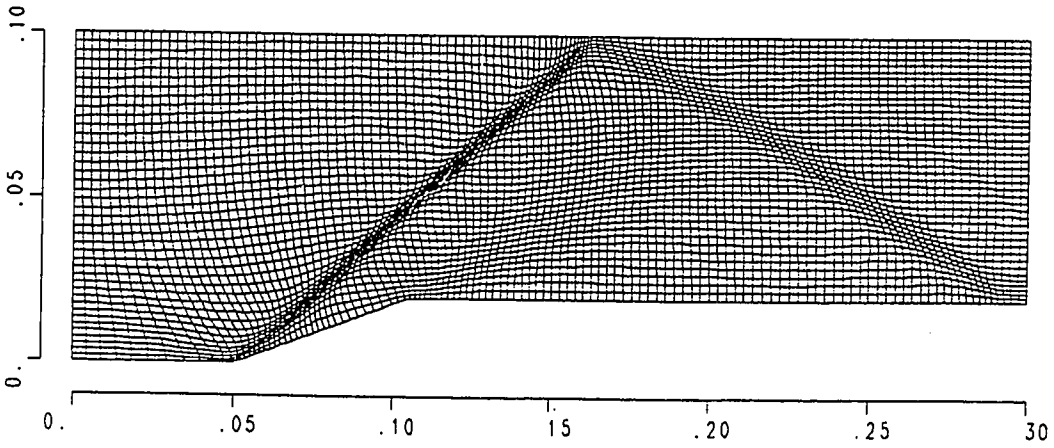

Adaptive grid after 0.2 msec.

Figure 5.1: Grid and Results from Glenn and Pratt, dimensions in meters

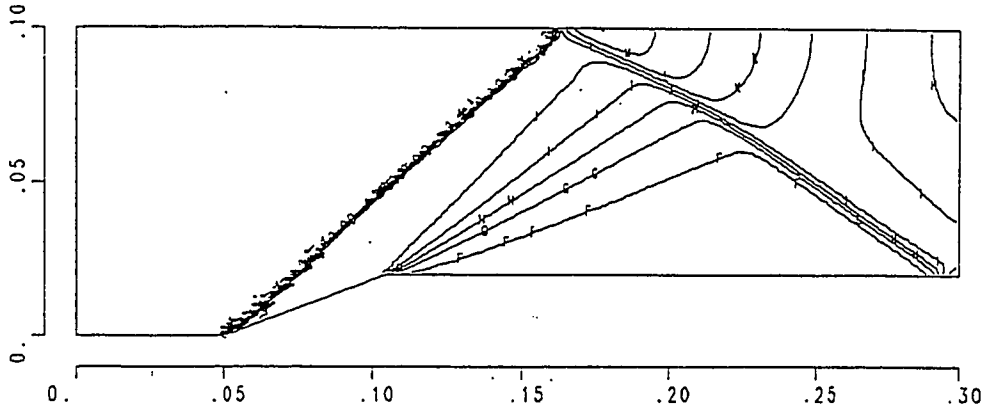

Pressure contours after 0.2 msec.

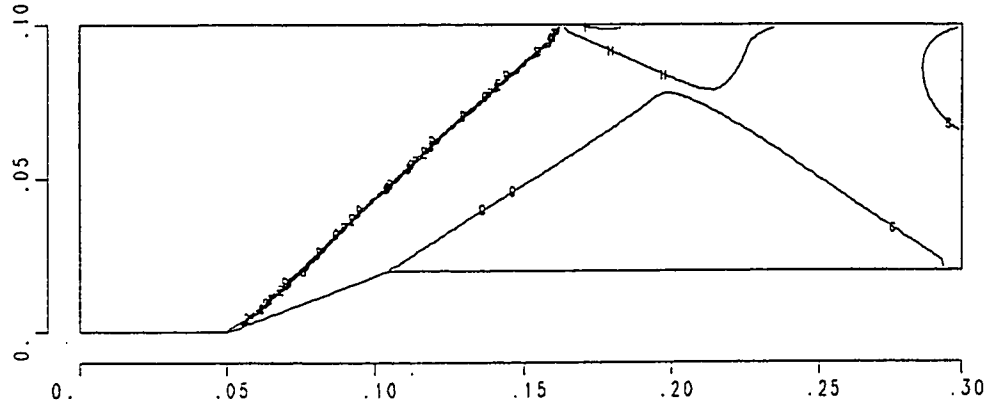

Temperature contours after 0.2 msec.

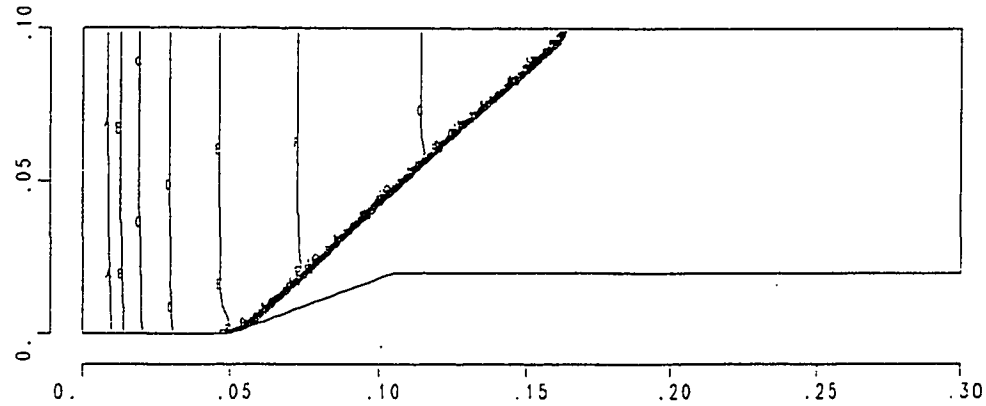

Induction time function $f(\tau)$ after 0.2 msec. Contour intervals shown: A = 0.1% , B = 0.2% , C = 0.4% , D = 0.6% , E = 0.8%, F = 1.0%, G = 2.0%. All higher values are collapsed into the wavefront.

Figure 5.1: (continued)

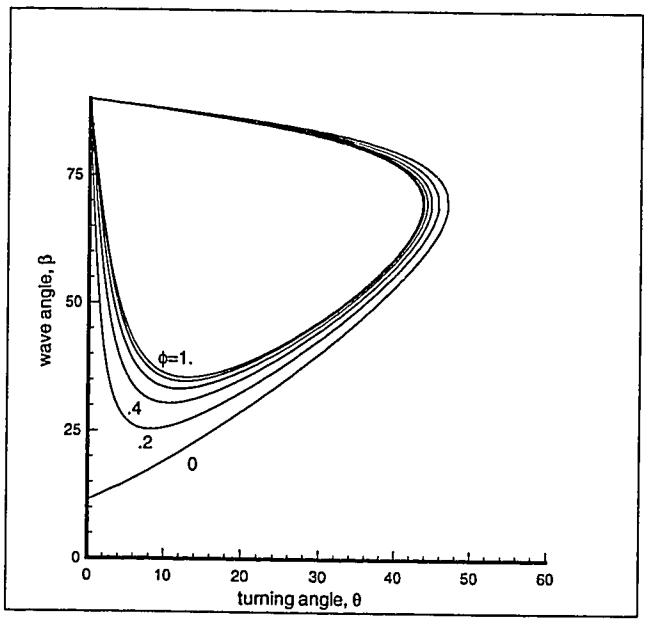

Figure 5.2: Stability Map for Planar Test Problem, hydrogen-air at $800^{o}K$, 1 atm, Mach 5 (ϕ = equivalence ratio)

without a significant downstream influence in the flow). Jump conditions are given in Table 5.1.

Glenn and Pratt's results in Figure 5.1 show a predicted angle of 41^{o} (after correcting for aspect ratio errors in the plots). The difference between this and the correct value of 38.1^{o} is likely due to the limited accuracy of the induction time model and simplified treatment of heat release.

5.3 Overdriven Wave Simulations

5.3.1 Test Problem Results

The 71 x 61 grid [1] used for the planar test problem simulation is shown in Figure 5.3. A shorter length of the physical problem is represented in this grid than in the original work (see Fig. 5.1), however the streamwise grid spacing remains the same

[1] The grid size is always specified as nx x ny, where nx is the streamwise grid cell count and ny is the cross-stream cell count.

Table 5.1: Rankine-Hugoniot Property Jumps Over an ODW for the Planar Test Problem

Property	upstream	downstream
Mach number	5.00	2.29
temperature, ^oK	800	3164
pressure, atm	1	8.56
density, kg/m^3	.3187	.765
mass frac. H_2O	.0	.190

as the original, unadapted grid. Grid clustering on the lower wall is required for use with the general non-penetrative boundary condition used there (see Section 4.6). Grid clustering is used on the upper wall to capture the detail of the shock reflection. Additional points were added in the cross-stream direction to give a uniform grid density in the middle of the flow field.

The simulation was begun with an impulsive initial condition (free stream conditions throughout the computational domain) and was integrated at the CFL stability limit until a steady state solution was achieved. The results are presented in Figure 5.4. Combustion product (H_2O) mass fraction contours show near-equilibrium values occurring in the shock/combustion wave. The wave measures 38.5°, which agrees very well with the value of 38.1° given by the Rankine-Hugoniot analysis for a weak, overdriven ODW. This is much better agreement than the 41° wave predicted by Glenn and Pratt, as might be expected due to the improved chemistry of the present model. Table 5.2 presents a comparison of the predicted and Rankine-Hugoniot jump conditions. The maximum difference is in static temperature, and is just slightly over one percent.

Steady state conditions are established by unchanging plots of the primary variables accompanied by a reduction in the L_2 norm of the residual of at least 3 orders of magnitude. (Mixture density is used as the test variable.) Steady state conditions were reached for the present simulation in 2600 time steps, which corresponded to a simulated time of 90 μs. This consumed approximately 12.5 hours of CPU time on a Sun SPARCstation 2 computer, a substantial time considering that this is only a two-dimensional model. Two different approaches were investigated to reduce this

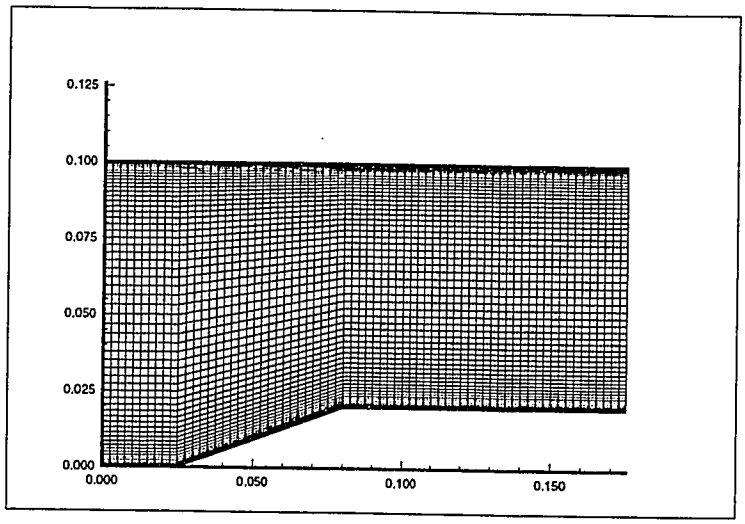

Figure 5.3: 71 x 61 Grid, dimensions in meters

computational effort, local time stepping and an alternative grid.

A major cause of the computational effort in the above simulation is the use of uniform (or global) time stepping to preserve time accuracy. In this case a uniform time step is applied to all cells, the magnitude of which is limited by the CFL stability limit in the most restrictive cell. This can be a severe restriction on convergence time in a model with widely varying grid spacing. In contrast to global time stepping, local time stepping varies the time step in each cell to impose a uniform CFL number.

Table 5.2: Comparison of Code Predicted and Rankine-Hugoniot Property Jumps for Planar Test Problem, Simulation Results from Figure 5.4 at grid point (28,12).

Post-Wave Property	R-H	code
Mach number	2.29	2.27
temperature, ^oK	3164	3200
pressure, atm	8.56	8.63
density, kg/m^3	.765	.762
mass frac. H_2O	.190	.192

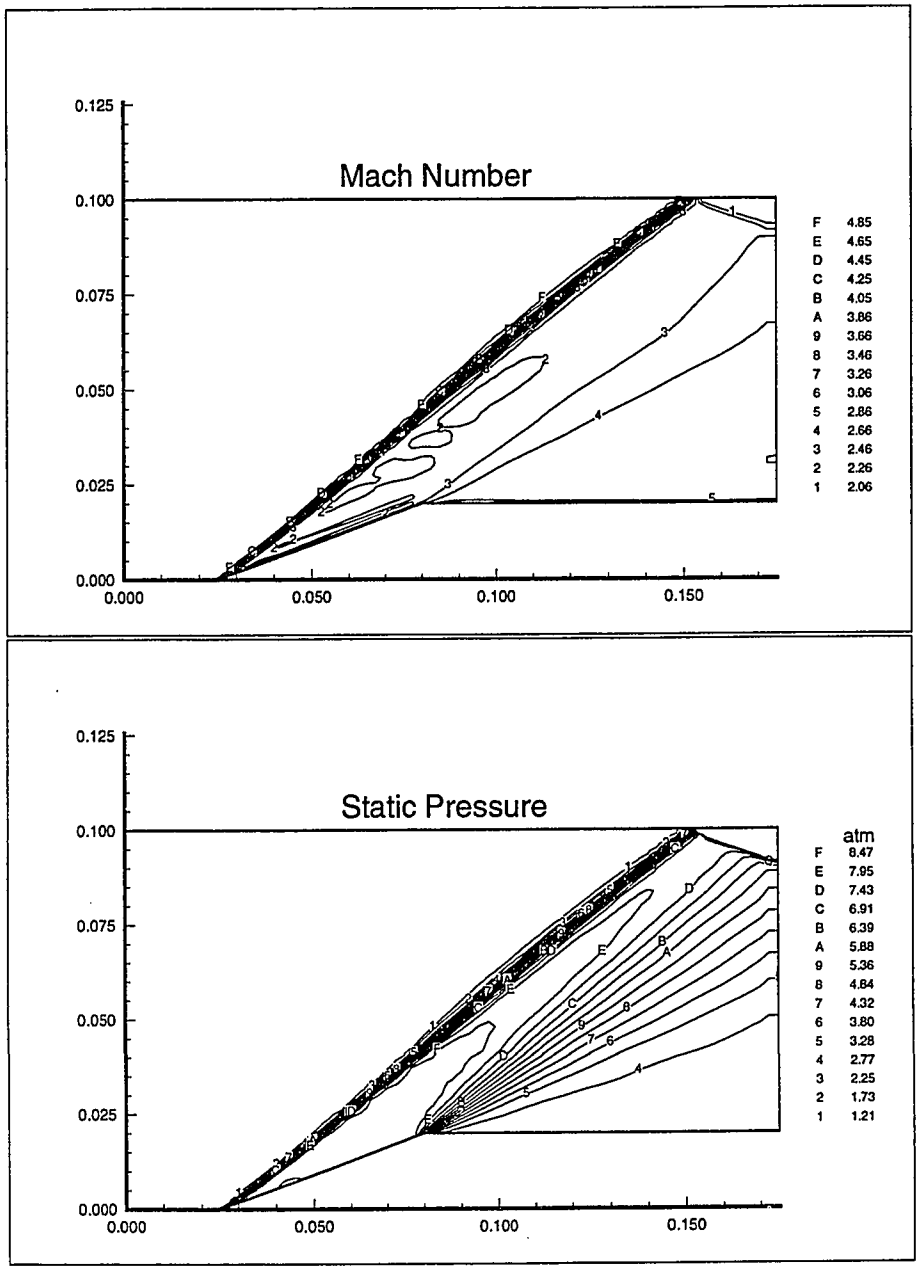

Figure 5.4: Inviscid Simulation Results for Full Scale Planar Test Problem

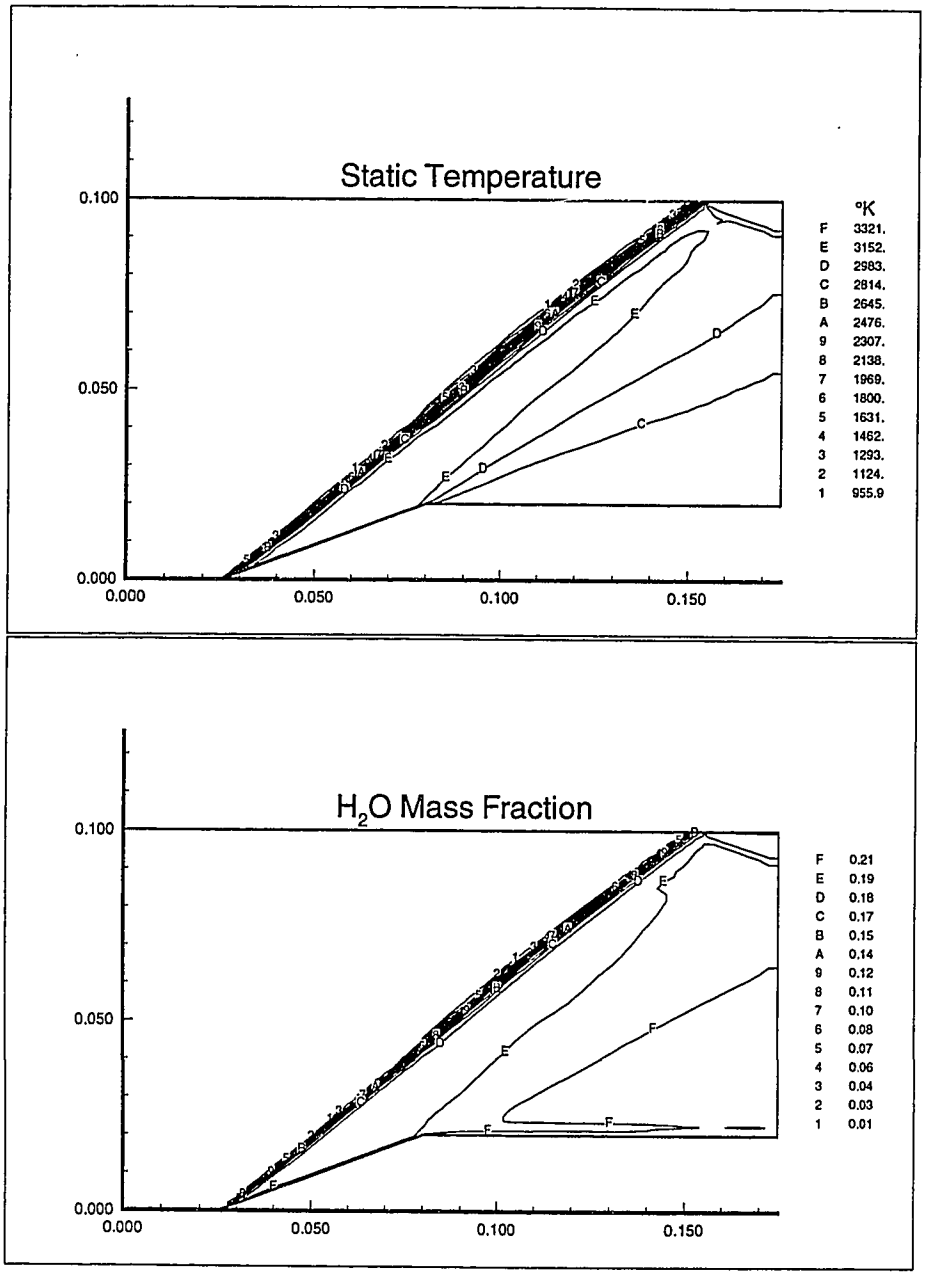

Figure 5.4: (continued)

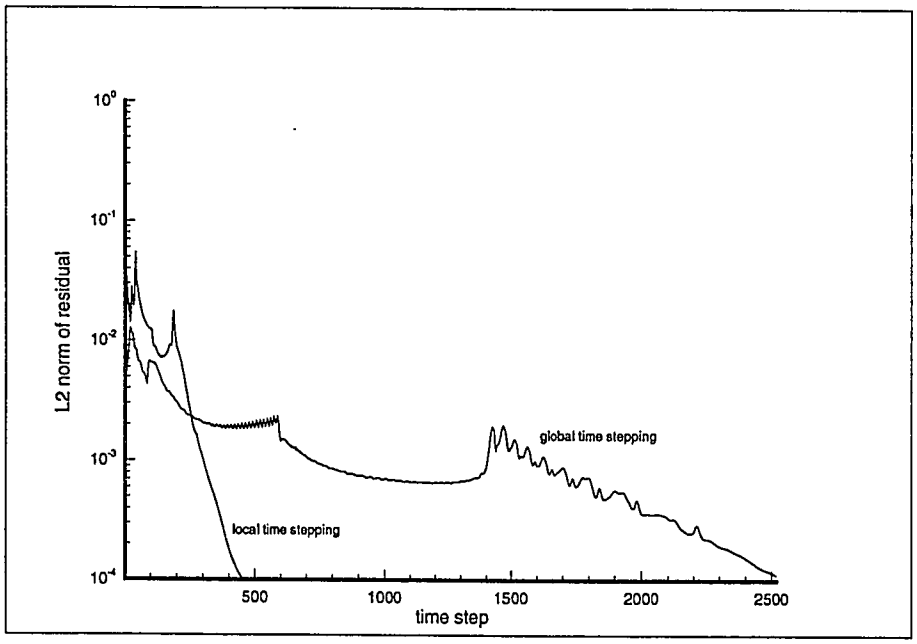

Figure 5.5: Convergence History for Planar Test Problem

Local time stepping is useful for accelerating the solution of an explicit algorithm on a non-uniform grid, but is not time accurate. While global time stepping can proceed at the CFL limit, local time stepping usually is limited to some fraction of this limit (say, $CFL = 0.5 \rightarrow 0.7$). See [42] for more details on local time stepping.

Since steady state solutions are of interest here, the lack of temporal accuracy is not a problem. As a comparison of global and local time stepping, the planar test problem was repeated with local time stepping. These results are identical to the global time stepped solution after 2600 time steps, the same L_2 norm of the residual being reached by the local time step simulation after only 450 time steps (see Figure 5.5). The first 25 steps were made at a CFL number of 0.25, the balance at 0.5. Though the local time step solution required less than one-fifth the number of time steps, it does require about 55 percent more CPU time per time step, a direct result of the increased burden on the kinetics integration for the time steps at the larger grid cells. Still, the overall CPU time for the local time stepped solution is just one-forth of that of the global time stepped solution, a substantial savings.

If attention is restricted to the ramp, an alternative computational grid can be used to give similar time savings *and* time accuracy. In this case, the only essential element is that the incoming uniform flow be turned through some angle θ. Two possible computational configurations are shown in Figure 5.6. The parallel inflow configuration models flow over a wall with a ramp, the skewed inflow configuration models flow over an aerodynamic wedge. For an inviscid flow they are functionally equivalent, however the latter offers a potentially enormous computational advantage over the other. The parallel inflow configuration requires that the normal momentum equation be solved along the lower wall boundary. This boundary condition requires a clustered grid along the wall, where the degree of clustering becomes more restrictive as the inflow Mach number increases (again, see Section 4.6). In the skewed inflow configuration, a simple reflective boundary condition suffices and a uniform grid can be used for any Mach number. The accompanying upper boundary condition is easily implemented as long as there is no outflow, i.e, as long as the oblique shock exits through the outflow boundary. The computational benefit is realized when an inviscid simulation is performed using an explicit solution algorithm, where the CFL stability limit constrains the maximum allowable time step to be proportional to the minimum grid cell dimension. For even modest hypersonic Mach numbers, say Mach 5, the clustered grid may require twenty times the computational work!

To test the skewed inflow approach, the planar test problem was simulated using two grids, the 45 x 23 grid shown in Figure 5.7 and a 181 x 91 grid. The results for both cases are shown in Figure 5.8 at 90 μs after an impulsive start. For the coarse grid, the wave is inclined 19° to the lower wall. This, added to the 20° angle of the incoming flow, gives a total wave angle is 39°. The fine grid is better with a total wave angle of 38.5°. A comparison of the Rankine-Hugoniot and predicted property jumps over the wave are given in Table 5.3. Differences here are within about 2 percent for the coarse grid and only slightly improved for the fine grid. While less accurate than the previous result (Table 5.2), this is still reasonable agreement with the correct solution. It is particularly interesting to see how good the coarse grid solution is considering the computational work invested; just 270 time steps were required. Simulations with the usual grid (i.e. Fig. 5.4) require over 2500 time steps to reach the same simulated time. Beyond predicting jump conditions, the real benefit of the fine grid is resolving details of the solution. The structure in the fine grid Mach

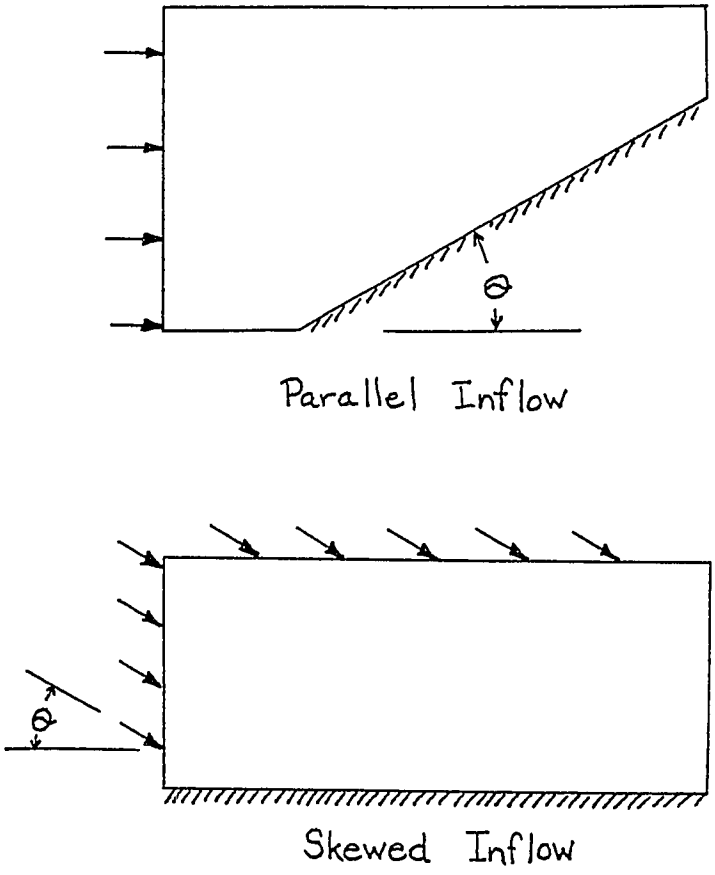

Figure 5.6: Alternative Configurations for Flow Over a Ramp

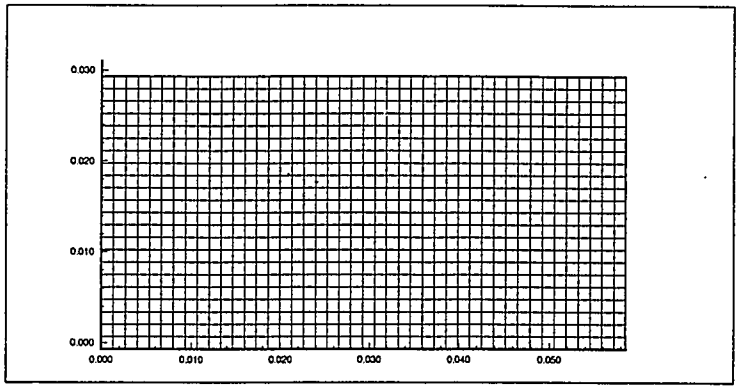

Figure 5.7: 45 x 23 Grid, dimensions in meters

contours in Figure 5.8 near the root of the ramp illustrate a finite chemical induction time prior to forming the ODW. This behavior will be further explored in the next section.

Table 5.3: Comparison of Rankine-Hugoniot Analysis and Finite Difference Predictions of Properties Downstream of ODW for Planar Test Problem with Uniform Grid, downstream properties taken at grid point (45,10) for the coarse grid and (150,25) for the fine grid

Property	R-H	Coarse Grid	Fine Grid
Mach number	2.29	2.24	2.25
temperature, $^{\circ}K$	3164	3216	3208
pressure, atm	8.56	8.70	8.65
density, kg/m^3	.7647	.761	.760
mass frac. H_2O	.190	.194	.192

Two alternatives have been demonstrated for improving the computational efficiency of steady state, inviscid simulations: local time stepping and an alternative computational grid. Only the first option is available for viscous simulations. Because of the need to resolve wall boundary layers, the required grid clustering eliminates

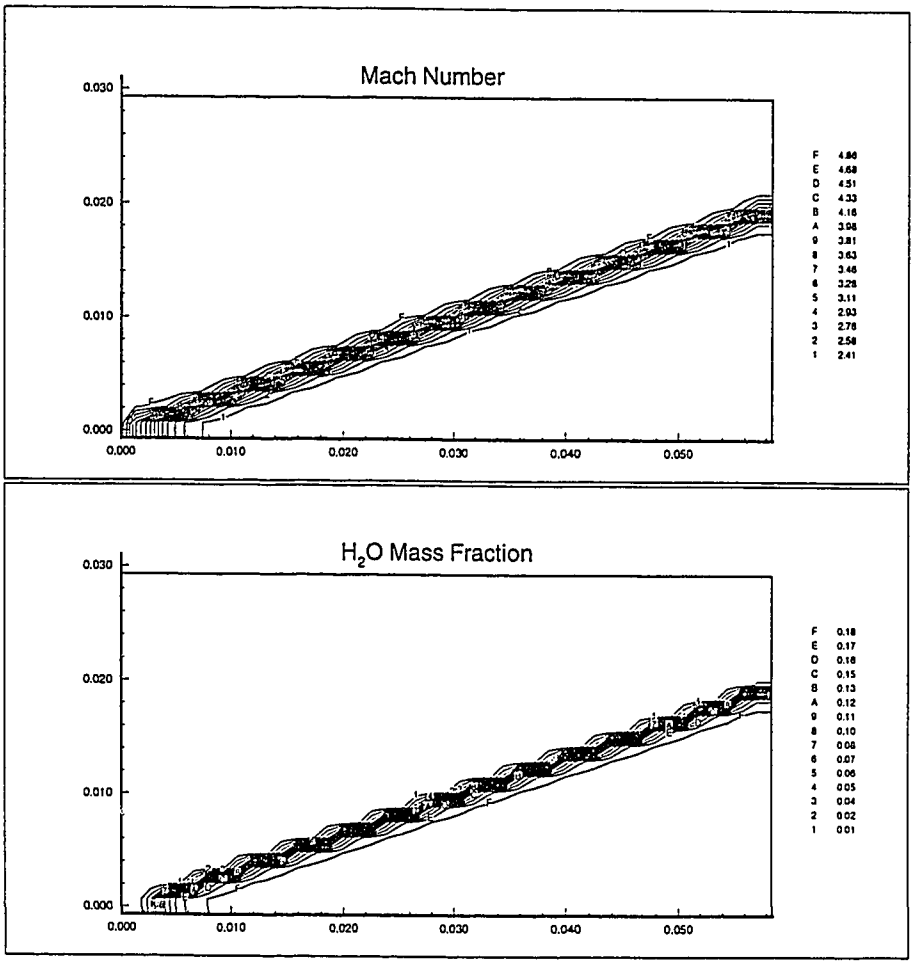

(a) 45 x 23

Figure 5.8: Solution for Planar Test Problem Using Uniform Grids (a) 45 x 23, (b) 181 x 91

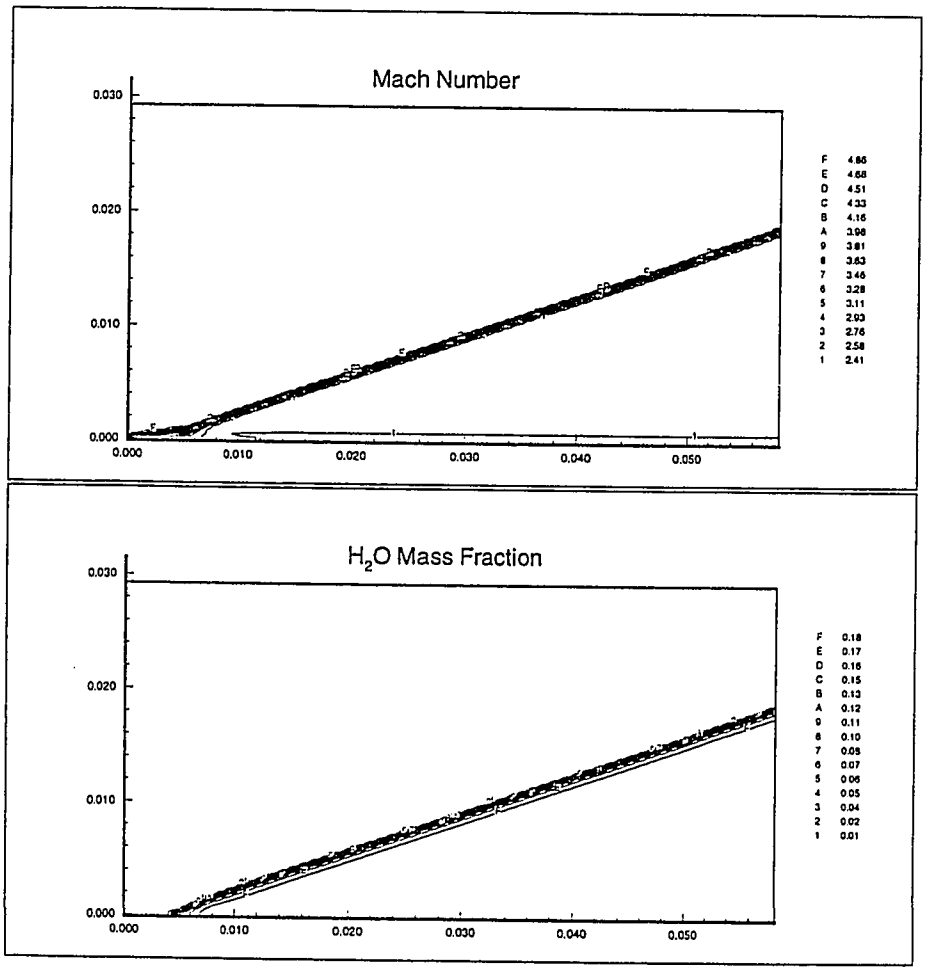

(b) 181 x 91

Figure 5.8: (continued)

the benefit obtained with the skewed inflow grid configuration. However, local time stepping remains an effective means of accelerating convergence.

5.3.2 Damköhler number Effects

The importance of the Damköhler number was discussed in Chapter 3. For an ODW to form, the chemical time scale must be small relative to the fluid residence time. Since the Damköhler number is the ratio of fluid to chemical time scales, this requires that $Da \gg 1$. In order to estimate the Damköhler number for the planar test problem, the chemical time scale, t_{chem} is obtained with a batch reactor simulation, i.e., integration of the chemical rate equations using the post-shock state as the initial condition. Jump conditions for a non-reactive shock are used in this case, the assumption being that the combustion wave has no influence on the shock wave. For these initial conditions, and the same chemical mechanism as in the multidimensional model (see Section 4.4.1), the chemical induction time is 2 μs (as indicated by a $1°K$ temperature increase). The fluid dynamic residence time, t_{fluid}, is based on the ramp length and post-shock fluid velocity. For the planar test problem, this transit time is 20 μs. The resulting Damköhler number is 10, and the predicted ODW is consistent with the requirement stated above. Two test cases are presented next that illustrate the effect of the Damköhler number.

The first variation on the planar test problem is to reduce the Damköhler number from 10 to 1. This was accomplished by reducing the problem dimensions by a factor of ten, while keeping all other aspects of the simulation unchanged. This computational domain was limited to the ramp and grid density was increased for greater resolution. The 129 x 121 grid is shown in Figure 5.9. The locally-time-stepped solution after 2100 time steps is shown in Figure 5.10. For this case heat release does not occur until the flow is at the top of the ramp; consequently a detonation does not form.

A third case was run with a one-fifth scaling of the planar test problem geometry and the computational domain was limited to the ramp. The Damköhler number in this case is 2. The locally-time-stepped results after 2100 time steps is shown in Figure 5.11. The combustion wave begins between 4.6 mm from the ramp tip and ends by 6.3 mm. The ODW angle is difficult to measure since it is still curved in the region simulated. The chemical induction time should elapse when the flow has

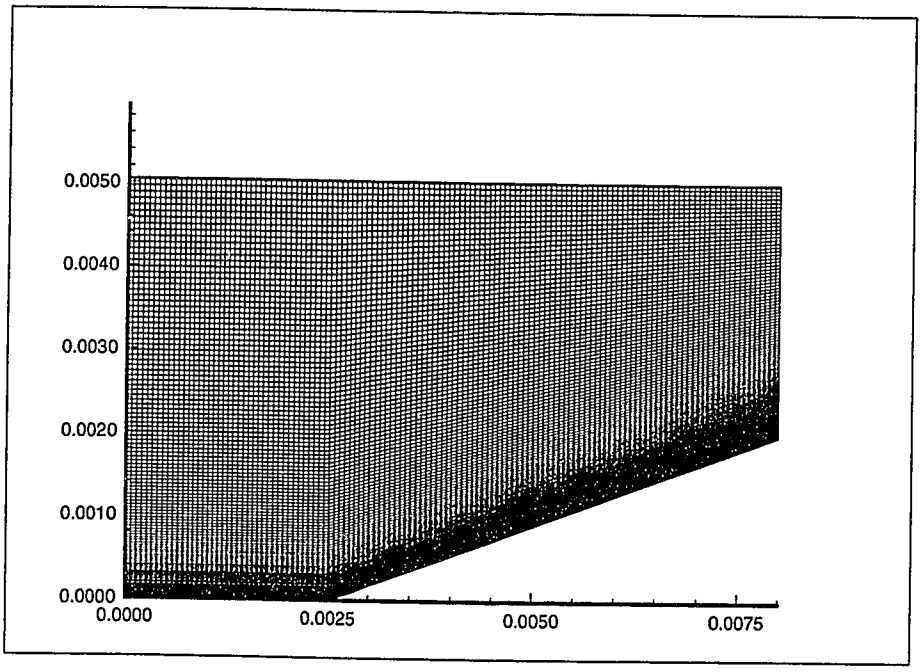

Figure 5.9: 129 x 121 Grid for One-Tenth Scale Problem, dimensions in meters.

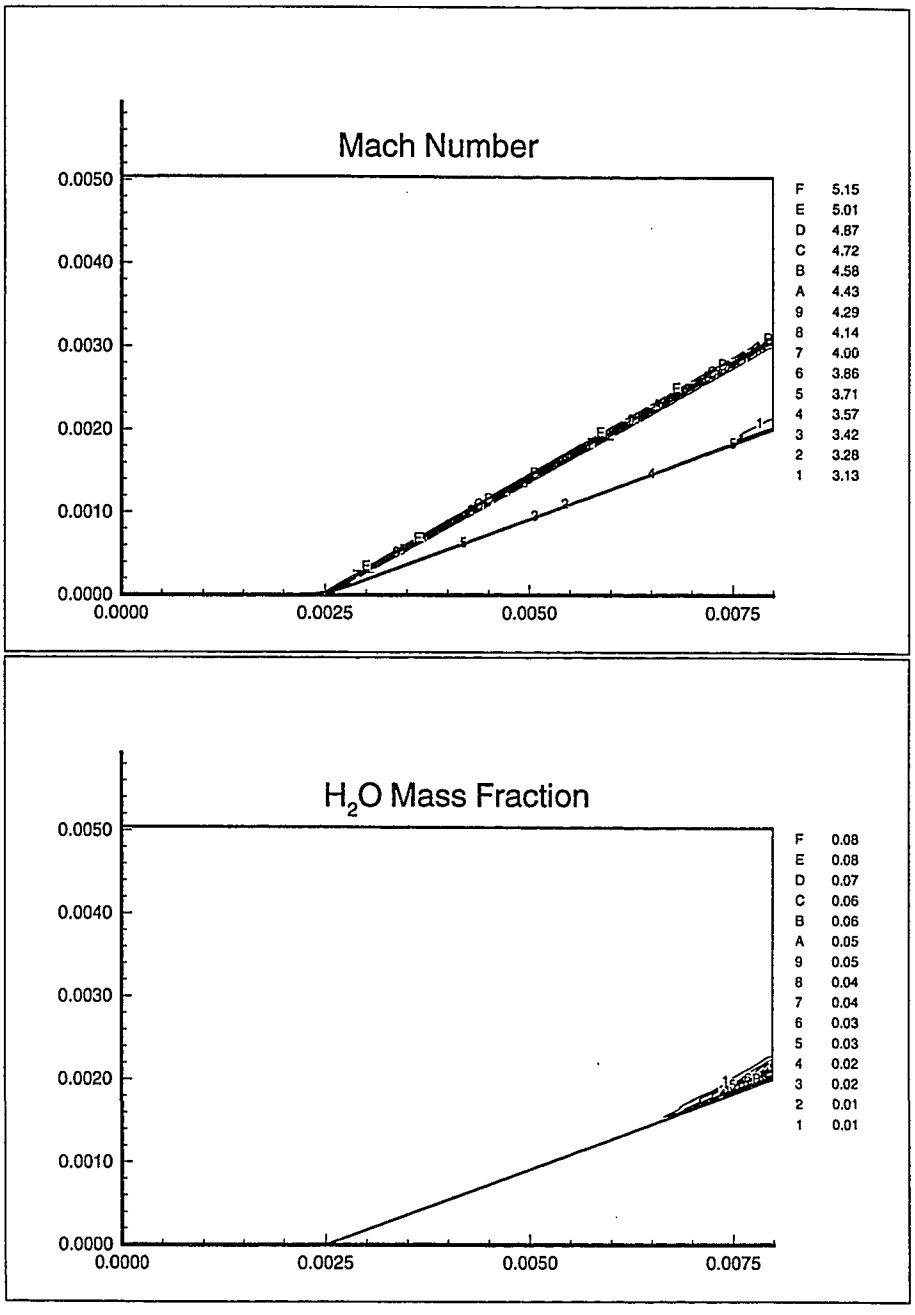

Figure 5.10: Inviscid Simulation Results for the One-Tenth Scale Planar Test Problem.

passed over $1/Da$ of the ramp length; for $Da = 2$ this would at 5.8 mm from the ramp tip. The finite difference model predictions bracket this nicely.

5.3.3 Viscous Effects

Results for the laminar simulation of the planar test problem are presented in Figure 5.12. In this case global time stepping was used, and the simulated time was the same as in the inviscid case, 90 μs. Despite the presence of wall boundary layers, the character of the ODW is undistinguishable from the inviscid case, both in angle and property jumps. This is consistent with expectations: ODWs, like shock waves, are inviscid phenomena.

This solution does require further examination. In the first place, the full-scale simulation would have been more properly modeled with turbulent flow properties. Based on free stream conditions and the upper wall length, Re_L is 5 million. Based on post-shock conditions and the ramp length, Re_L is 1.3 million. Both are well beyond the transitional value of 500,000. However, despite the fact that the turbulent boundary layer would be thicker, the ODW would still be present. It has been consistently shown in this research that, if an ODW forms in an inviscid simulation, it will always be present in the viscous simulation. Second, even if laminar properties are assumed, the boundary layers are not well resolved by the computational grid. The boundary layer thickness was estimated as 0.06 mm at the top of the ramp, based on post-shock properties, laminar flow and ignoring the wall preceding the ramp. The minimum cross-stream grid spacing was 0.1 mm, and was therefore incapable of resolving the boundary layer. A refined grid simulation was performed of the ramp region only. The 129 x 121 grid was the same shown in Figure 5.9 except for the length scale. Boundary layer resolution for this case was a full 15 cells at the top of the ramp. The refined grid solution is shown in Figure 5.13. The ODW is still present and is unchanged from Figure 5.12.

As in the inviscid simulations, it is interesting to consider smaller geometric scales to evaluate the impact of reduced Damköhler number. The viscous simulation of the one-tenth scale case used the same 129 x 121 grid, but at reduced scale. The Reynolds number for this case is well *below* the transitional value at the top of the ramp and the numerical simulation should be a reasonable representation of the physical problem. The solution shown in Figure 5.14 contains a large recirculation zone at the foot of the

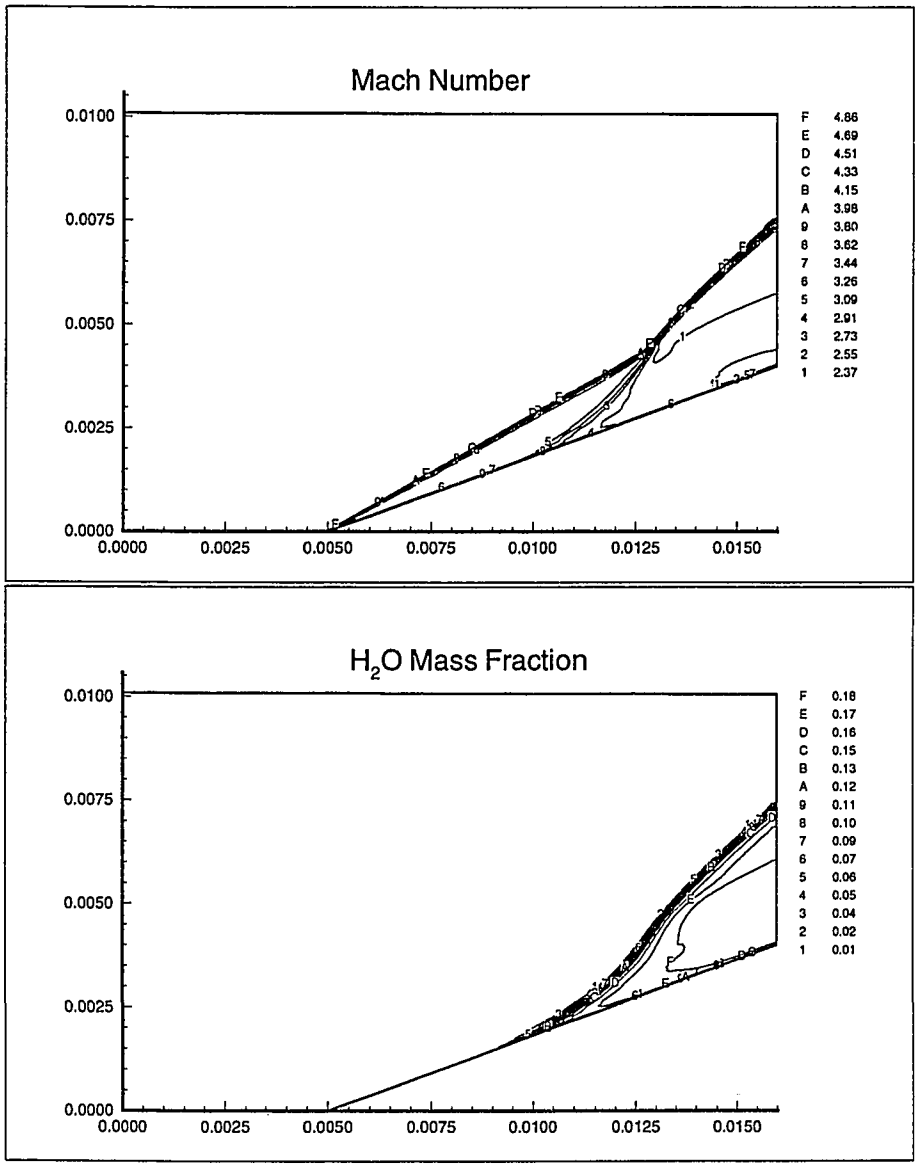

Figure 5.11: Inviscid Simulation Results for One-Fifth Scale Problem.

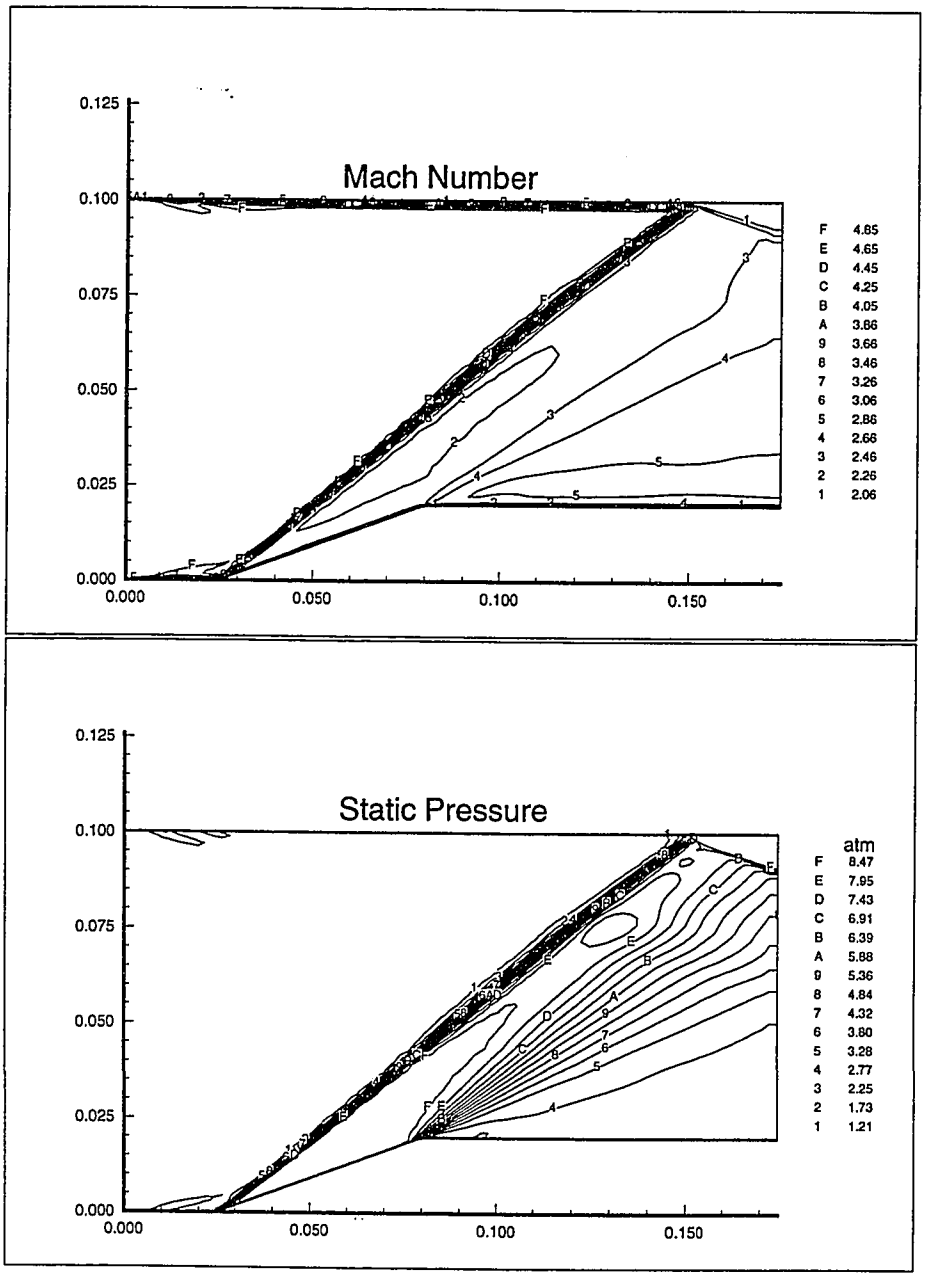

Figure 5.12: Laminar Solution for Full-Scale Planar Test Problem

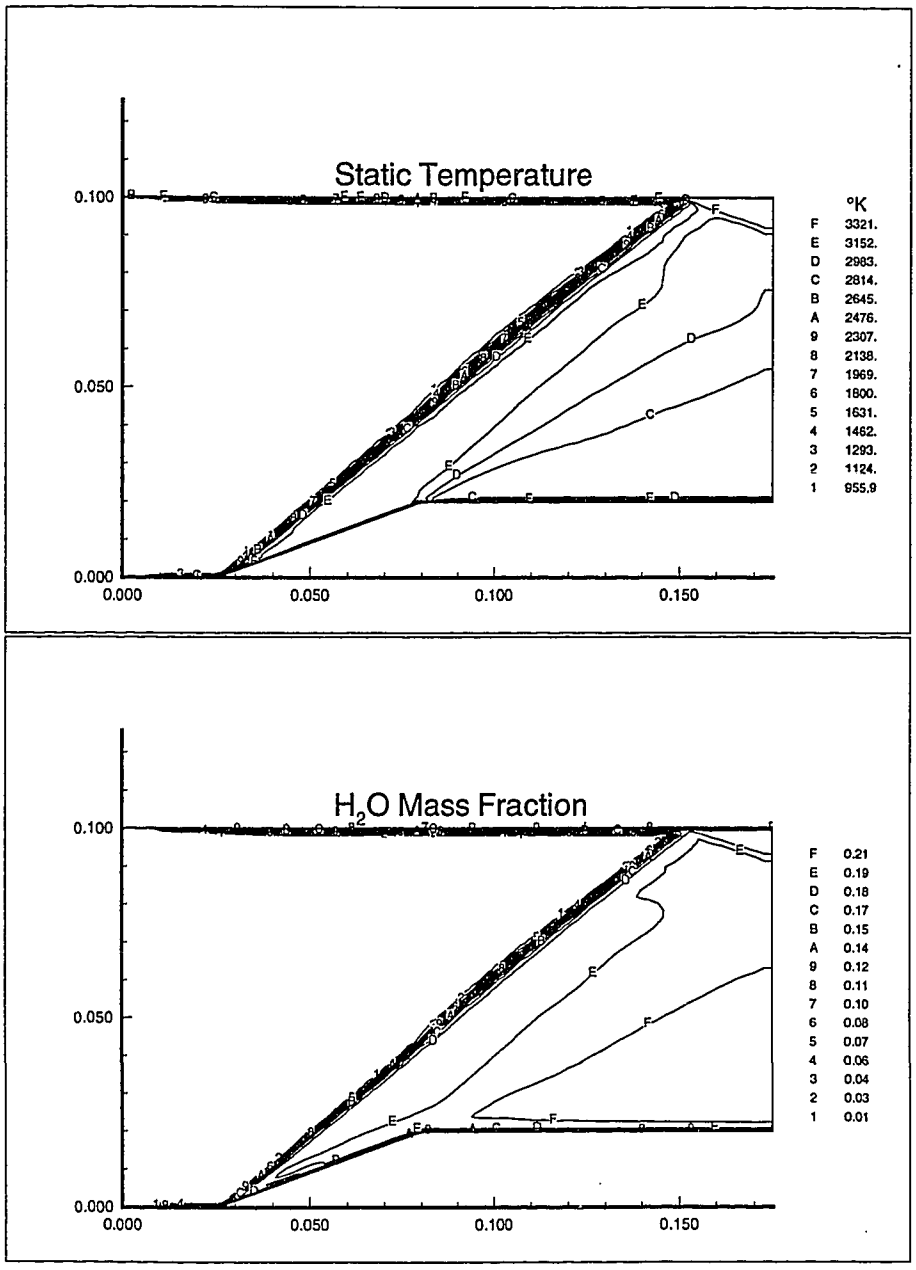

Figure 5.12: (continued)

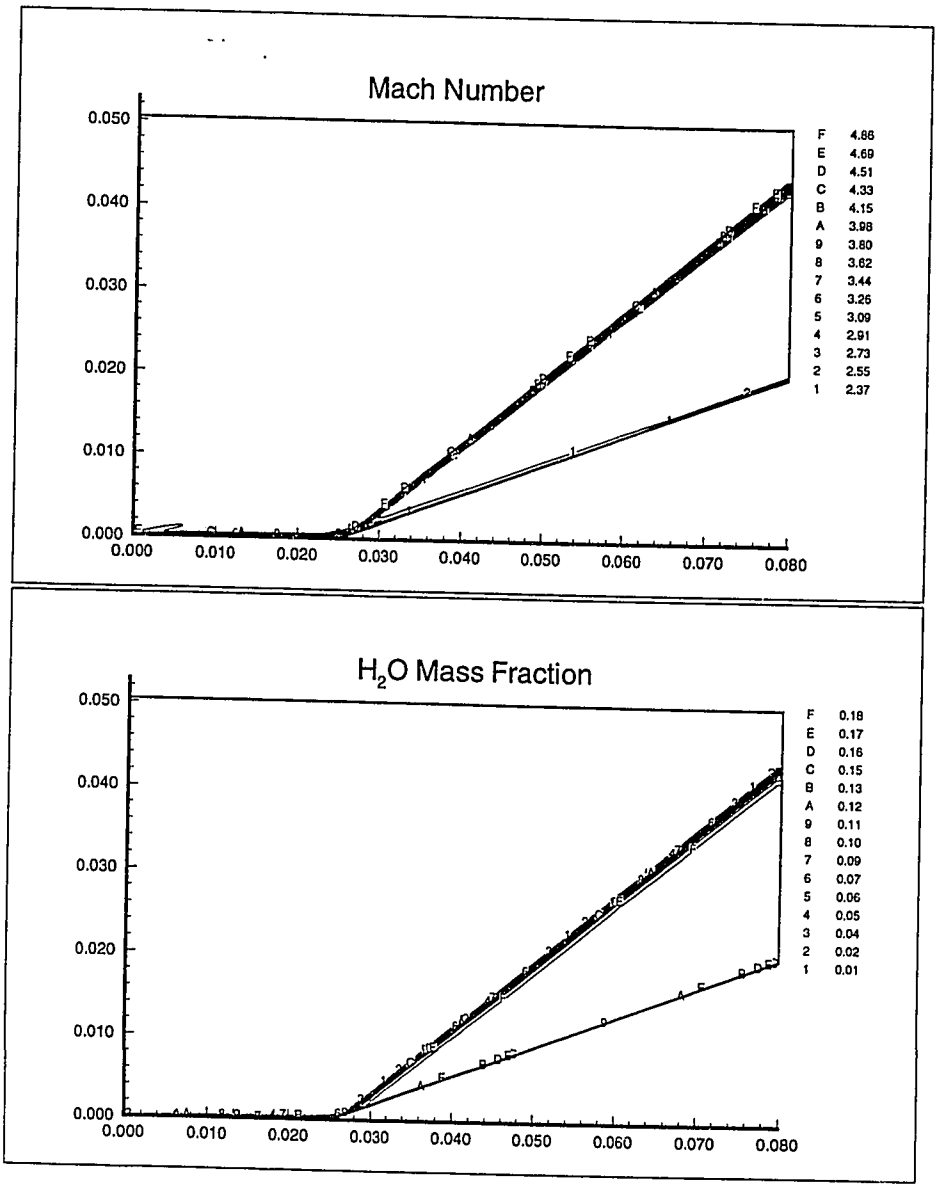

Figure 5.13: Laminar Solution for Full-Scale Planar Test Problem, Ramp Region Only, 129 x 121 Grid

ramp that was just barely visible in the full-scale simulation (Figure 5.13). Despite this viscous feature, and a significantly thickened boundary layer on the ramp, the only combustion not in the boundary layer is at the end of the ramp. In fact, solution beyond the boundary layer is virtually identical to the inviscid case (Figure 5.10). The extent of this similarity is shown better in the one-fifth scale simulation, which is discussed next.

The viscous result for the one-fifth scale problem is shown in Figure 5.15. Re_L based on the ramp length is roughly 300,000 and the corresponding laminar boundary layer thickness is only 0.03 mm. The minimum lateral grid cell spacing for this case is 0.001 mm, which produces a well resolved boundary layer. This viscous result is indistinguishable from the inviscid result (Figure 5.11) away from the boundary layer.

This apparent lack of effect of viscosity on the ODW refutes previous conclusions made by this author [11]. These earlier observations were based on simulations using the NASA Lewis code RPLUS-2D [46] that were later confirmed with the present code. Unfortunately, at least in the latter simulations, the boundary layer was insufficiently resolved by the computational grid. In general, care must always be taken to resolve the physical boundary layer because the numerical boundary layer will always be at least one cell thick; too coarse of a grid was found to produce an ODW that would not be present for a finer grid.

5.3.4 Alternate Wedge Angles and Equivalence Ratios

The last three cases for planar geometry use a variety of turning angles and mixture equivalence ratios to further explore the stability map (Fig. 5.2). The first two cases are overdriven ODWs, the third case is in the region of the stability map that dictates an underdriven ODW. All three cases are perturbations of the planar test problem, and an inviscid simulation is used exclusively.

The first case is for a 30° turning angle and a fuel-air equivalence ratio of 0.2. The Rankine-Hugoniot analysis gives a wave angle of 42.9° and the simulation results shown in Figure 5.16 give 43.5°.

The second case is for a 10° turning angle and an equivalence ratio of 0.2. The results are presented in Figure 5.17. For this case the agreement is excellent between the theoretical wave angle (25.6°) and measured value from the simulation (25.5°). The geometrical scale for this problem had to be increased by an order of magnitude

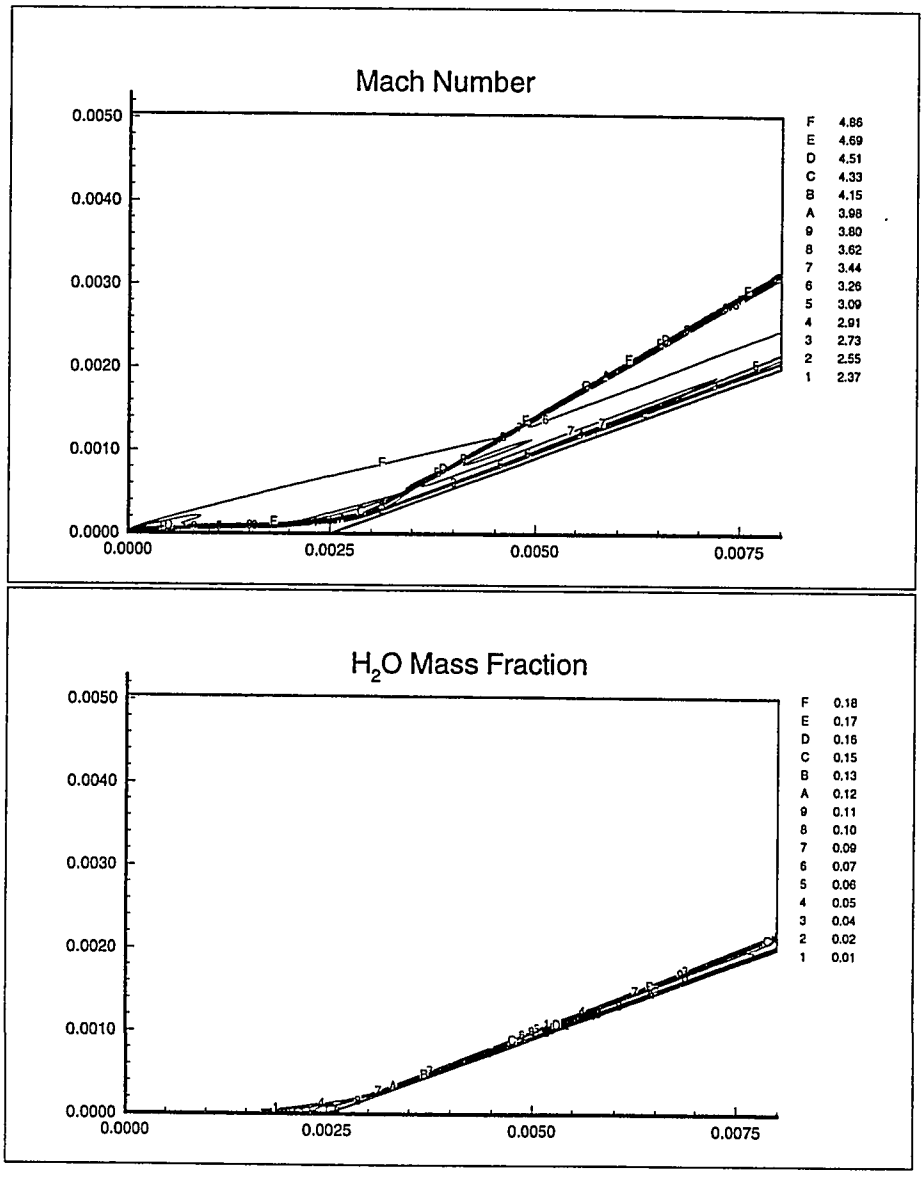

Figure 5.14: Laminar Simulation Results for One-Tenth Scale Problem, Ramp Region Only, 129 x 121 Grid

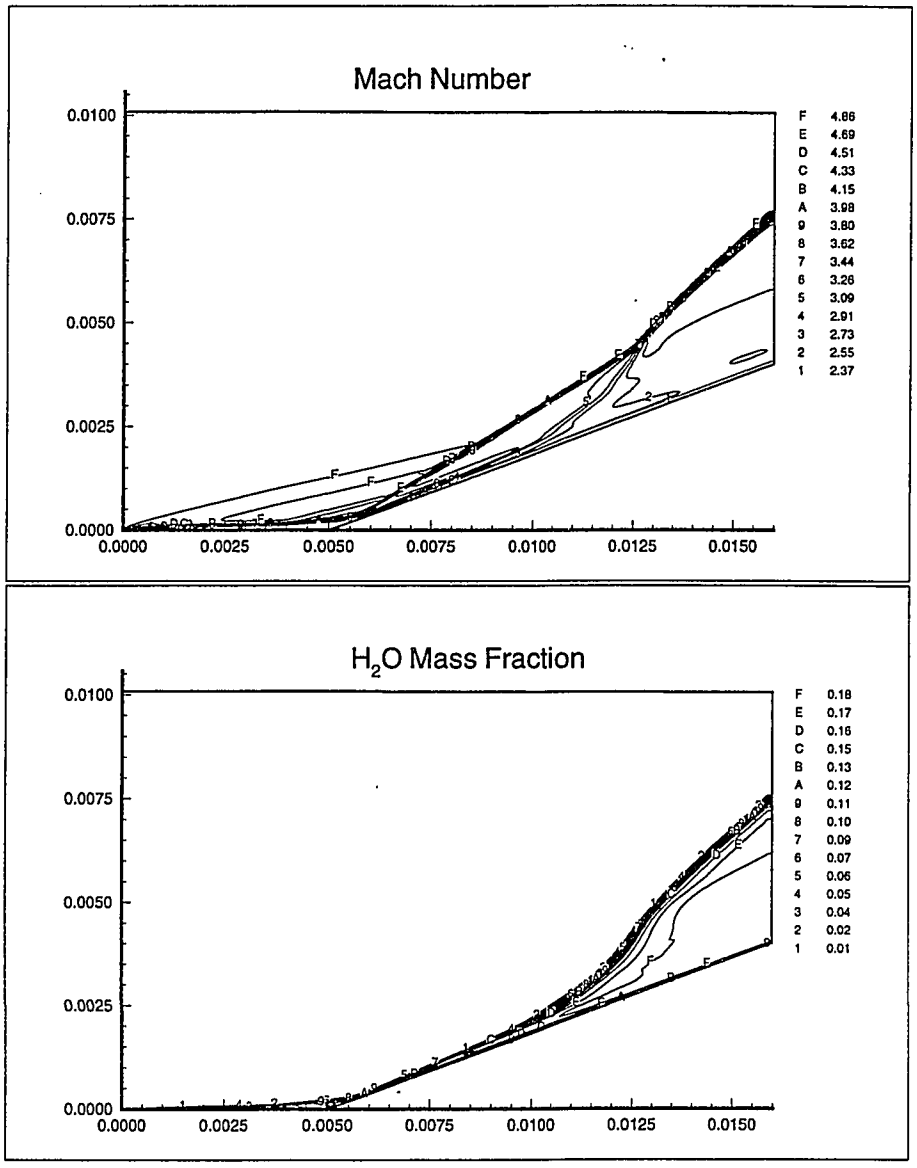

Figure 5.15: Laminar Simulation Results for One-Fifth Scale Problem

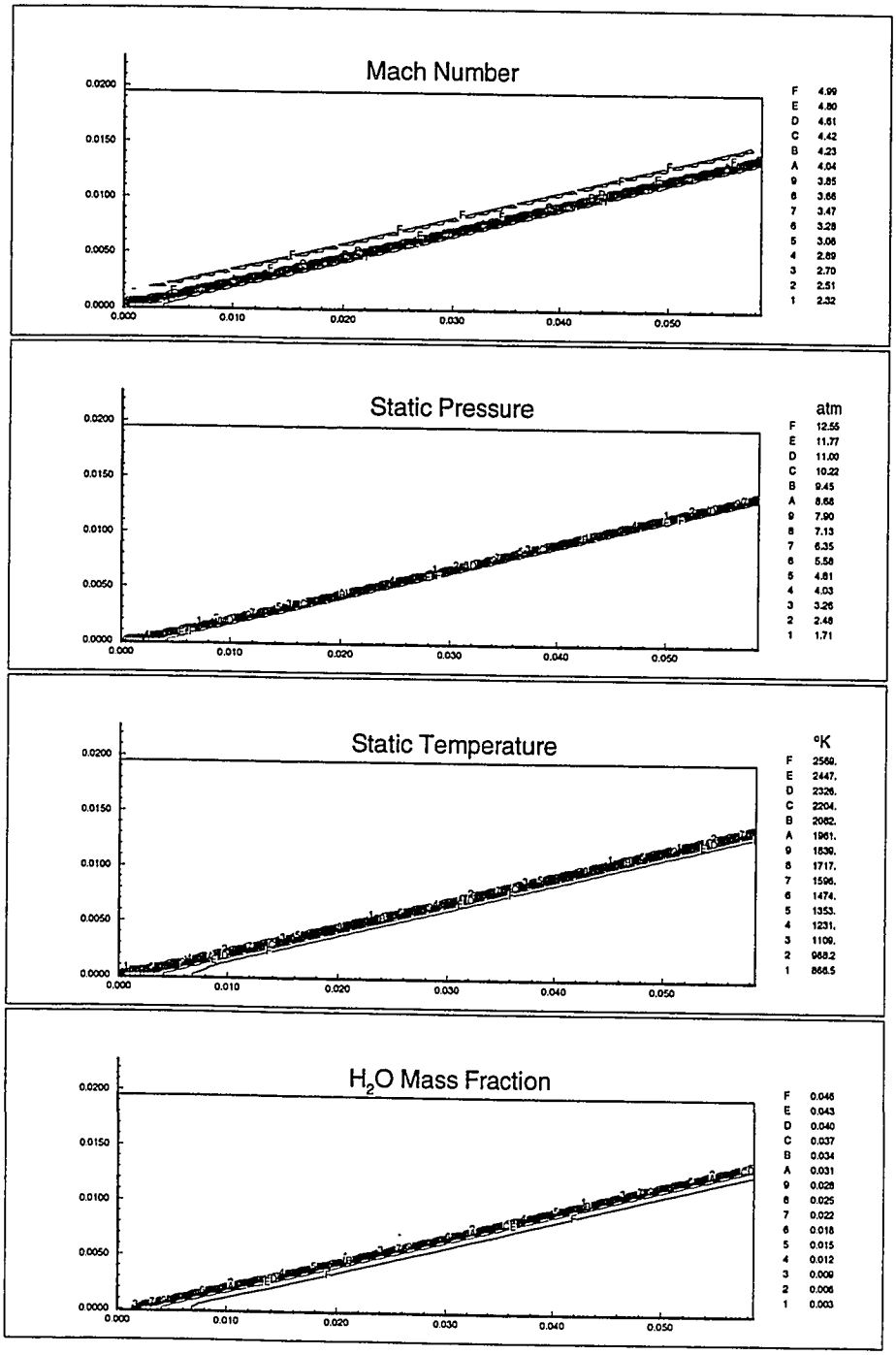

Figure 5.16: Simulation Results for Planar Test Problem with 30° Turning Angle and $\phi = 0.2$.

over the base case planar test problem, in order to achieve a coupled ODW in the computational domain. The simulation had to be run under a reduced time step ($CFL = 0.2$) to converge. This is due to the effect of large Da on reducing the stable time step.

5.4 Underdriven Wave Simulations

Underdriven ODWs were described along with the Rankine-Hugoniot analysis in Chapter 3. Their distinguishing characteristic is of course that the post-shock normal velocity is supersonic (at least that is the requirement for the Rankine-Hugoniot analysis, where the wave is modeled as a single discontinuity of infinitesimal thickness).

Despite the existence of a mathematical solution, there have been no plausible explanation for underdriven waves. Instead, the existing literature argues against their physical possibility [15, 47]. The underdriven wave cannot be dismissed on second law considerations, the argument is instead based on wave mechanics: an ODW is formed because of the support provided by a ramp; if the post-shock normal velocity is supersonic, then the ODW is effectively isolated from its support. Siestrunck et al. [47] illustrated this with a post-wave characteristics diverging from the wave. Powers and Gonthier [48] show the possibility of an underdriven wave for a hypothetical gas mixture with exothermic/endothermic reaction sequence. Of course this is the opposite of mixtures of interest in propulsion.

This section will demonstrate by numerical solution and explanatory model, that an underdriven ODW is in fact possible. The key is that the underdriven wave is comprised not of a single discontinuity, but of two waves, an overdriven ODW followed by an expansion wave. These features will be shown in numerical solutions. Transient solutions give clues to the wave's formation mechanisms, and perturbed solutions illustrate interesting properties of the wave once formed.

5.4.1 Simulation Results

The test problem being considered is a variation on the planar test problem, using the same Mach 5 flow of a stoichiometric H_2/air mixture at $800°K$ and 1 atm, but instead with a 10° turning angle. This puts the problem in the underdriven region of the stability map, as shown in Figure 5.18. The reduced turning angle decreases

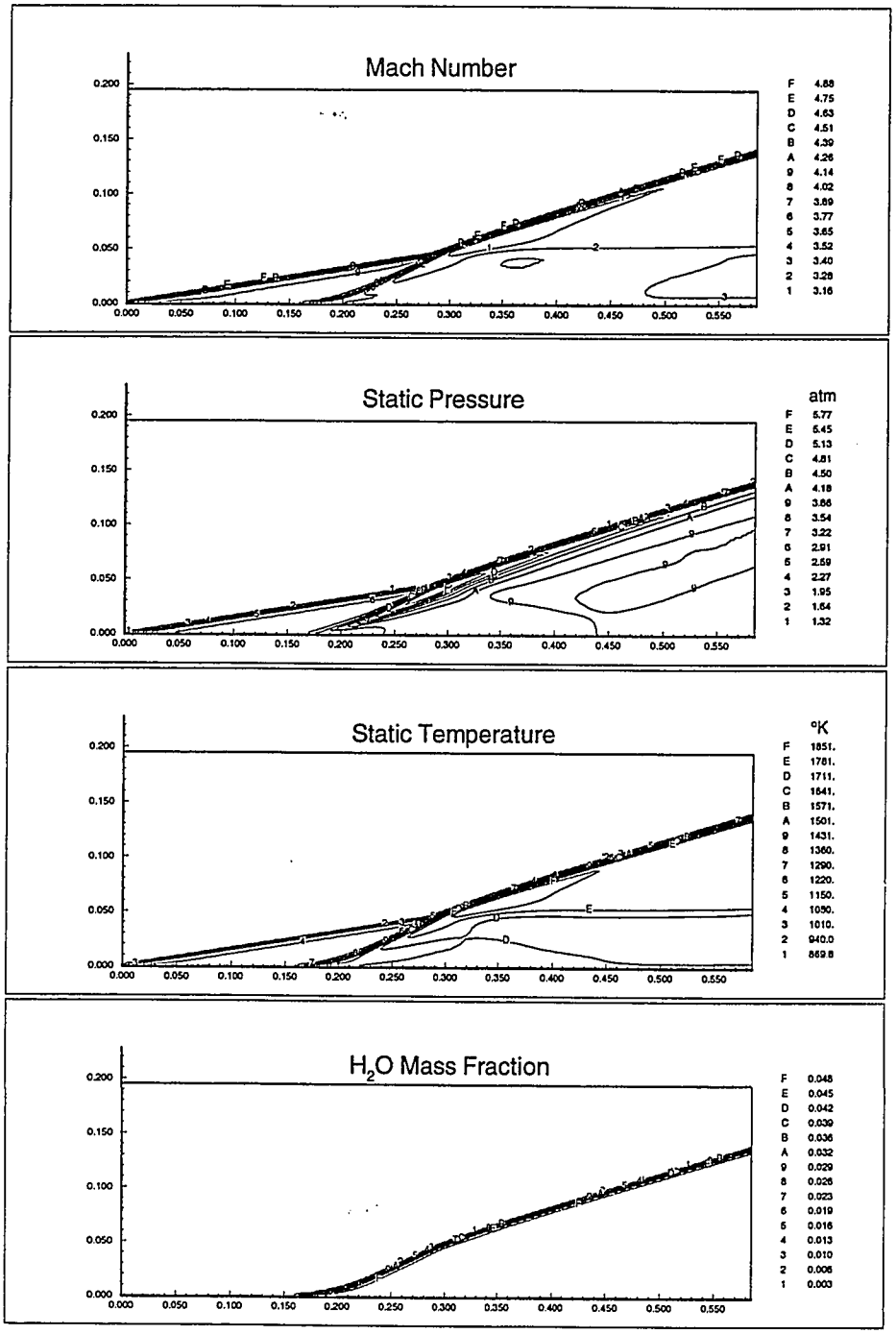

Figure 5.17: Simulation Results for Planar Test Problem with a 10° Turning Angle and $\phi = 0.2$.

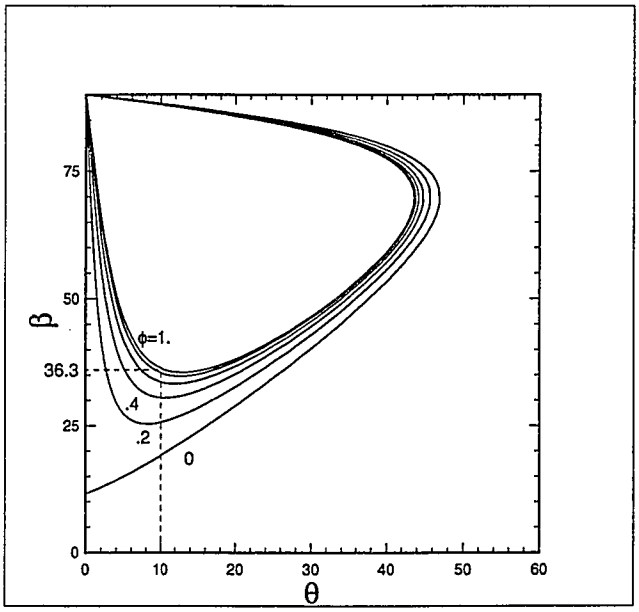

Figure 5.18: Location of Underdriven Test Case on Stability Map, hydrogen-air at $800^{o}K$, 1 atm, Mach 5 (ϕ = equivalence ratio)

the compression wave strength and results in an increased induction time, sufficiently increased to move the heat release outside the computational domain. As in the last overdriven case in Section 5.3.2, the geometric scale is increased by ten times over the planar test problem to deal with this change. Figure 5.19 shows the skewed-inflow computational domain for this problem.

The converged solution for a 261 x 131 computational grid is given in Figure 5.20. Away from the wall, the static pressure contours show a compression wave followed by an expansion fan. H_2O mass fraction contours confirm that the combustion wave is coupled to the compression wave. In this sense, the lead wave looks very much like an overdriven ODW. The difference is shown in the velocity vector plot for this solution in Figure 5.21, where a sample fluid pathline shows that the flow is overturned through the ODW (i.e. turned away from the wall), and is then turned back to parallel the wall by the expansion fan. In fact, the overturning is sufficient to give a subsonic post-shock normal velocity. A comparison of post-expansion conditions agrees very well with jump conditions predicted by the Rankine-Hugoniot analysis (Table 5.4).

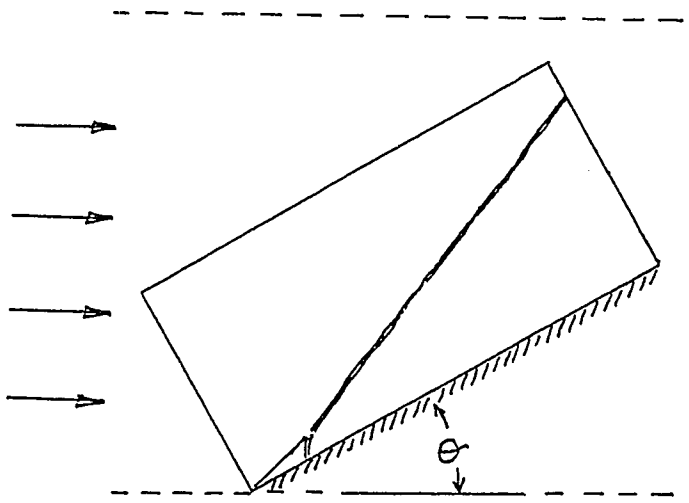

Figure 5.19: Computational Domain for Skewed Inflow Solution

The detonation wave angle is also in very good agreement.

Nearer the wall, the flow passes first through a non-reactive oblique shock, then releases heat in a deflagration wave after the induction time elapses. This induction time agrees with that predicted in a batch reactor simulation. The deflagration pressurizes the local flow consistent with Rayleigh heat addition in a supersonic flow [49]. In fact, pressures immediately behind this near-normal deflagration wave are the highest observed in this simulation, at just under 8 atmospheres. Although the Mach number decreases, it stays well into the supersonic range. An expansion wave is seen to emanate from the junction of the deflagration, non-reactive shock and detonation waves. This expansion wave reflects off of the wall producing the expansion fan through which the post-detonative flow is turned.

The solution was also computed for the parallel inflow configuration to illustrate agreement. The results for pressure contours are given in Figure 5.22. Both solutions are the result of a grid refinement study which is discussed in a subsequent section. Slight differences in induction length are observed for the two grids.

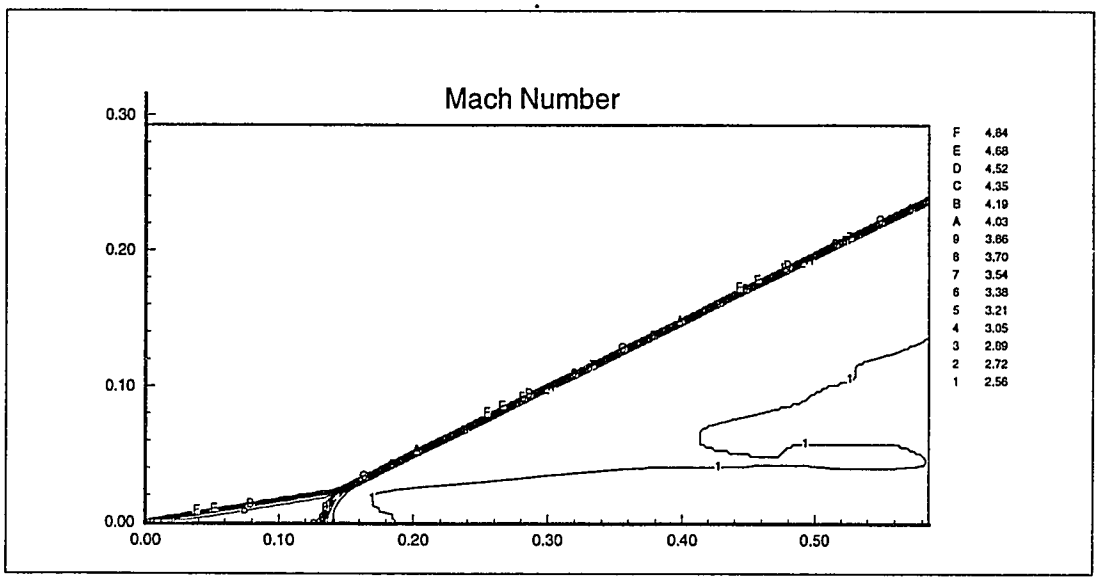

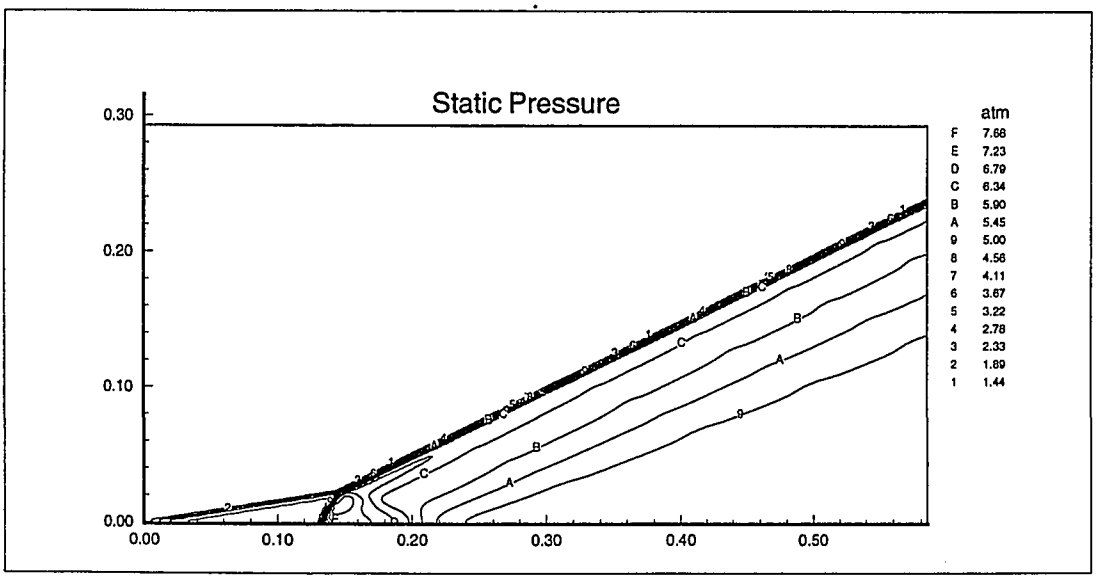

Figure 5.20: Simulation Results at 0.34 ms for Planar Test Problem with 10° Turning Angle and $\phi = 1$, 261 x 131 Grid.

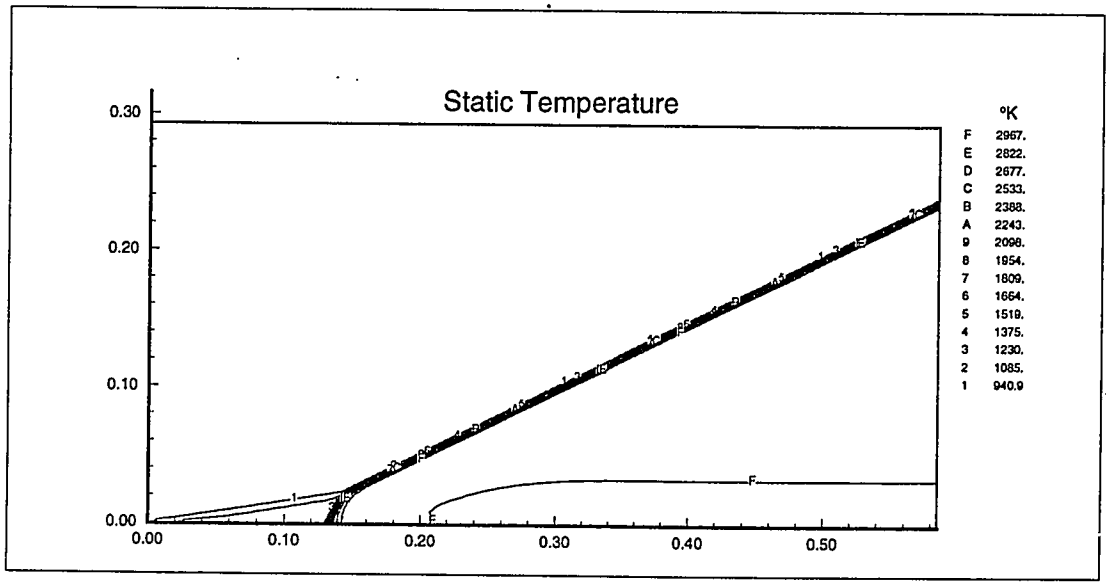

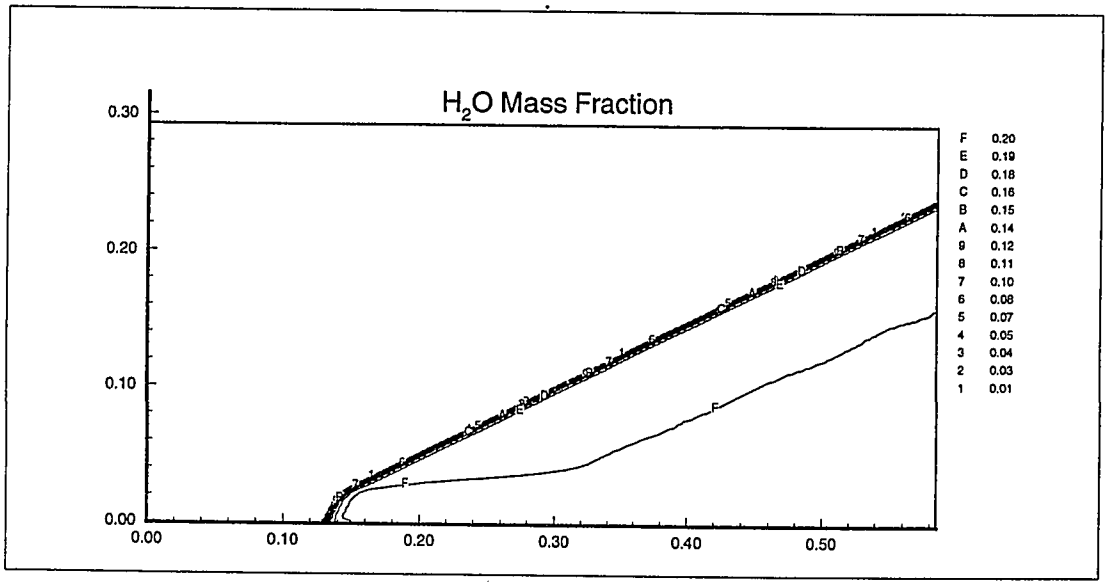

Figure 5.20: (continued)

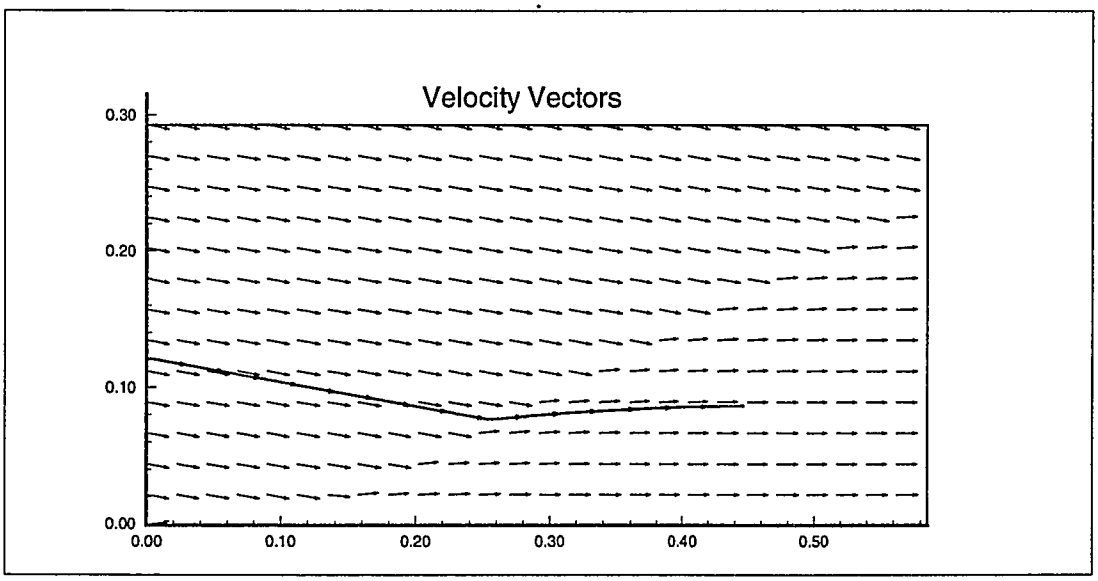

Figure 5.21: Vector Plot Showing Overturning of Flow Through Initial Wave and Subsequent Turning Back to be Parallel With the Wall Support

5.4.2 Combined Wave Model

Now a model is proposed for the underdriven wave. The boundary conditions call for an underdriven wave, but since it cannot occur (at least in the single discontinuity assumed in the Rankine-Hugoniot analysis), an overdriven wave of equivalent wave angle is formed in its place. However, since the overdriven wave overturns the flow, an expansion wave is required to restore the flow parallel to the wall. Pratt et al. [15] hypothesized that "only enough heat release would occur to admit a C-J wave." These simulation results suggest that full heat release does occur, however, this requires a two-wave or combined wave structure. To test this theory, solutions for two well understood waves are combined: 1) the Rankine-Hugoniot solution for an overdriven ODW of equal wave angle and 2) a Prandtl-Meyer expansion back to the ramp angle.

The Rankine-Hugoniot solution for the underdriven ODW is 36.33° for a 10° turning angle. For a weak overdriven ODW, this same wave angle requires a 16.7° turning angle. This is State 2 in Table 5.5. Note the post-shock normal Mach number of 0.805.

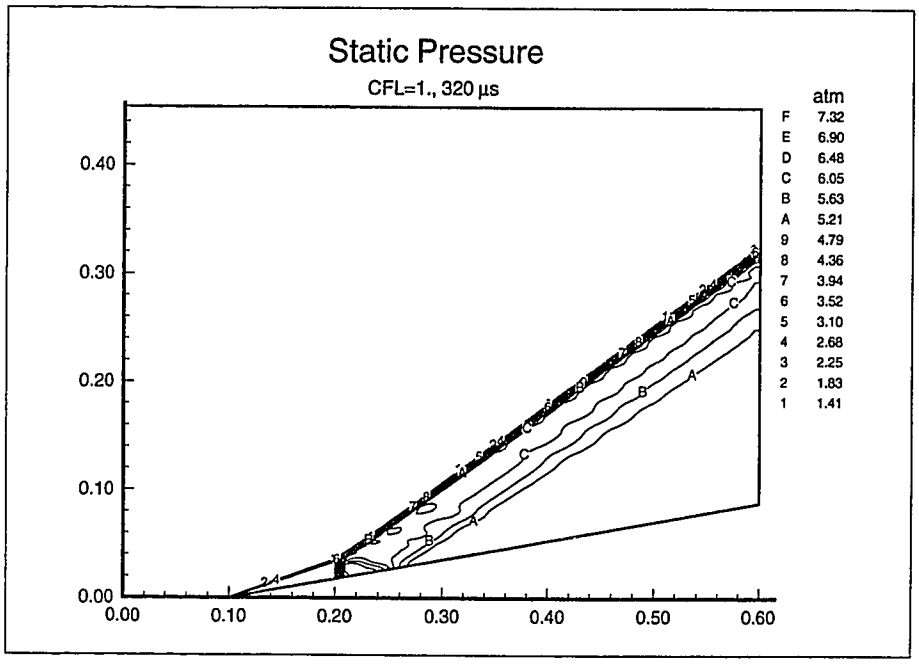

Figure 5.22: Static Pressure Contours at 0.32 ms for Parallel Inflow Configuration, 121 x 121 Grid, CFL = 1.

Table 5.4: Comparison of Rankine-Hugoniot and CFD Predicted Properties Downstream of Expansion for Underdriven ODW Test Problem with 261 x 131 Uniform Grid, downstream properties taken at grid point (194,28)

Property	R-H analysis	CFD pred.
Mach number	2.58	2.56
velocity, m/s	2959	2953
temperature, ^oK	2971	3002
pressure, atm	4.91	4.92
density, kg/m^3	.473	.469
mass frac. H_2O	.204	.206

The expansion fan must then turn the flow back parallel with the wall, through an angle of 6.7^o ($16.7^o - 10^o$). To use the Prandtl-Meyer solution, perfect gas behavior (constant specific heats) and frozen flow must be assumed. Actually, there is a slight shift in equilibrium species distribution toward more H_2O as the gas temperature drops through the expansion fan. Because of this, the results for the combined wave model ("comb." under State 3) are slightly lower in temperature and, consequently, slightly higher in density.

Although the Prandtl-Meyer expansion is isentropic, the shifting equilibrium case may not be. Still, agreement between the entropies resulting from the underdriven wave and the combined overdriven wave and expansion is excellent.

The numerical solution is given for two points in Figure 5.20. The first is our State 2, the intermediate state between the overdriven ODW and the expansion fan. It was selected by maximum positive cross-stream velocity. The second point corresponds to the exit from the expansion fan, State 3, and was marked by zero cross-stream velocity. First compare properties for the combined wave and the numerical solution at State 2. Considering that the numerical solution is somewhat limited by grid resolution, the values show good agreement. The post-ODW normal Mach number is 0.84 which is slightly greater than the Rankine-Hugoniot solution and which corresponds to a turning angle of 15.6^o.

The numerical solution results at State 3 shows excellent agreement with the Rankine-Hugoniot solution for the underdriven ODW. The agreement with State 3

resulting from the combined wave analysis is good, but is clearly limited by the idealized nature of the Prandtl-Meyer solution. (Note, in particular, the change in numerical model's H_2O mass fraction between States 2 and 3.)

Table 5.5: Comparison of Post-Wave conditions for Rankine-Hugoniot Solutions for the Combined Wave and Pure Underdriven Wave with Numerical Model (State 2 at grid point 105,28 and State 3 at grid point 194,28)

	1	2		3		
Property	inflow	comb.	numer.	comb.	under.	numer.
Mach number	5	2.3965	2.42	2.62	2.58	2.56
normal to wave		0.805	0.84			
ratio spec. heats	1.3627	1.250		1.250	1.249	
density,kg/m^3	0.3186	0.6570	0.618	0.477	0.473	0.469
pressure, atm	1	7.16	6.72	4.80	4.91	4.92
temperature,^oK	800	3095	3086	2857	2971	2953
entropy,J/kg^oK	10185	11183		11183	11180	
H_2O mass frac.	0.	.196	.198	.196	.204	.206

Approximations made in the combined model do not detract from its utility in explaining the numerical results. In summary, the combined wave model is an appealing argument which suggests that the physically realizeable form of an "underdriven wave" is comprised of an overdriven ODW through which the flow is overturned with respect to the support, followed by an expansion wave to turn the flow back parallel to the support.

5.4.3 Grid and Time Step Convergence Study

The results in Figure 5.20 are the results of a detailed grid and time step convergence study. Spurious solutions were obtained at the largest grid cell size and time step. Successive refinements in grid cell size and time step were necessary to produce physically correct solutions.

Pressure contour plots for a few examples are shown in Figure 5.23. The spurious solution is given in Figure 5.23a, and was produced with a 45 x 23 grid and a CFL

number of 0.2. Notable among the strange features of this result is the *compression* fan following the ODW. Simply reducing the time step (to a CFL number of 0.02) changes the solution radically (see Figure 5.23b. The wave angle falls back to the roughly 36° given by the Rankine-Hugoniot analysis. The chemical induction time is now evident and the compression fan has given way to an expansion fan. For remaining cases run with finer grid resolution, the wave angle always agreed well with the Rankine-Hugoniot analysis, however the chemical induction time was highly dependent on the time step. Figure 5.23c is a good example, where the induction time is one-third that given by a batch reactor simulation.

The results of the convergence study are summarized in Figure 5.24. Individual cases are located on a plot of CFL number versus grid size. Data given for each run are induction time in μs and wave angle in degrees. Three regions are identified: a spurious region where results are totally misleading, an erroneous region where wave angle is adequately predicted but induction time is incorrect, and finally an acceptable region where both induction time and wave angle are acceptably predicted. Only with the finest grid are good results obtained.

5.4.4 Wave Formation and Stability

Formation of the underdriven ODW can be observed in the transient solution results leading up to the steady solution in Figure 5.22. These are illustrated in a series of six static pressure plots in Figure 5.25. Observations for each plot follow:

$58\mu s$ The lead shock has moved off the ramp into the incoming flow, with the leading edge having reached its oblique angle, and with the balance of the shock remaining parallel to the ramp. Flow that has passed through the oblique portion of the shock burns as a deflagration at a distance downstream corresponding to the chemical induction time. The combustion wave shows up in this plot because thermal energy release causes volume dilatation and an accompanying pressure increase. The leading edge of the combustion wave is parallel to the shock, indicating a uniform induction time. Farther downstream the pressure contours surround a region of much higher pressure; a compression wave, which also contains the combustion wave, propagates laterally from the high pressure region into the unburned gas mixture, and an expansion wave separates the high pressure region from the rest of the burned gas near the wall.

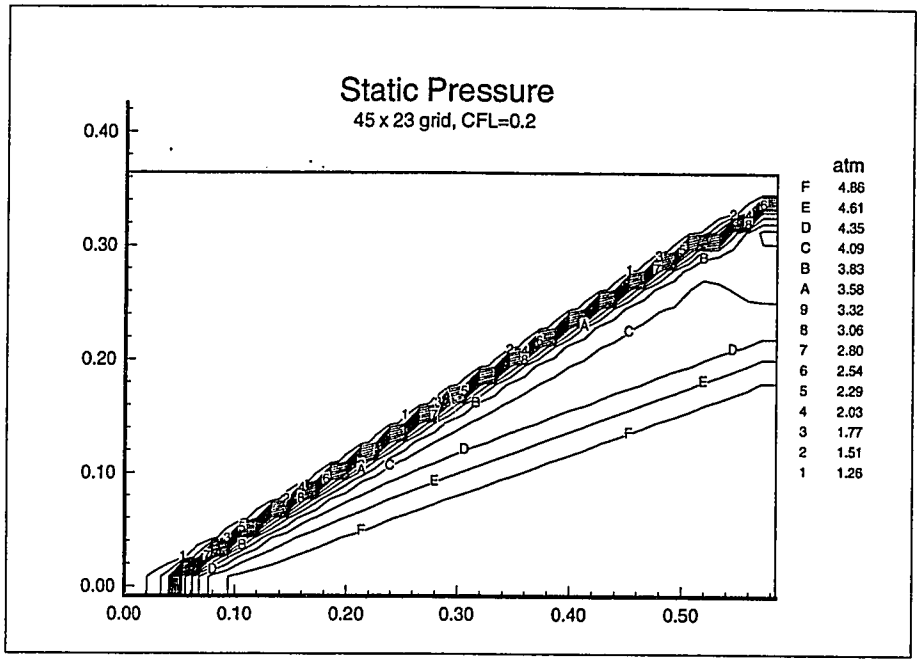

(a)

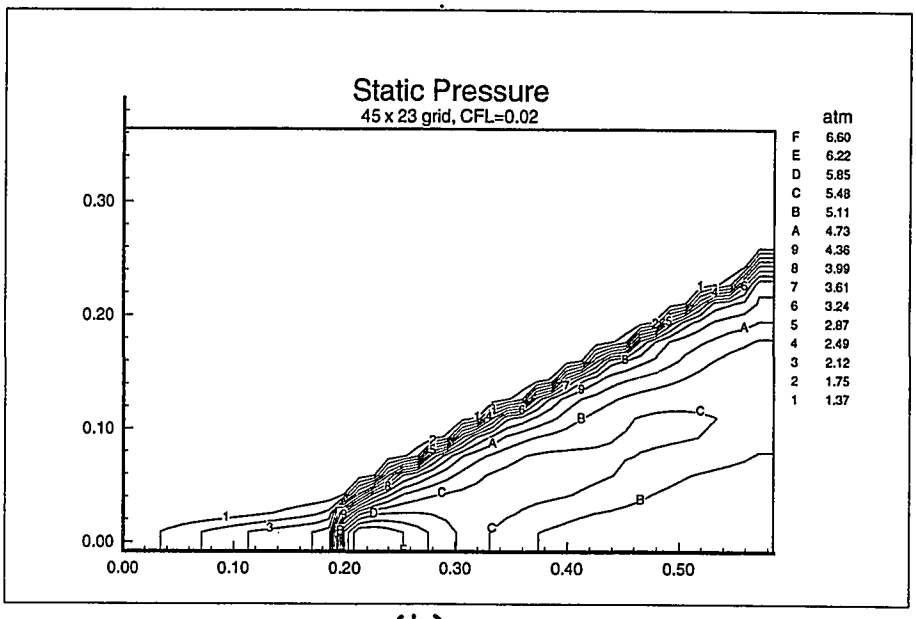

(b)

Figure 5.23: Sample Pressure Contour Plots From Grid and Time Step Convergence Study.

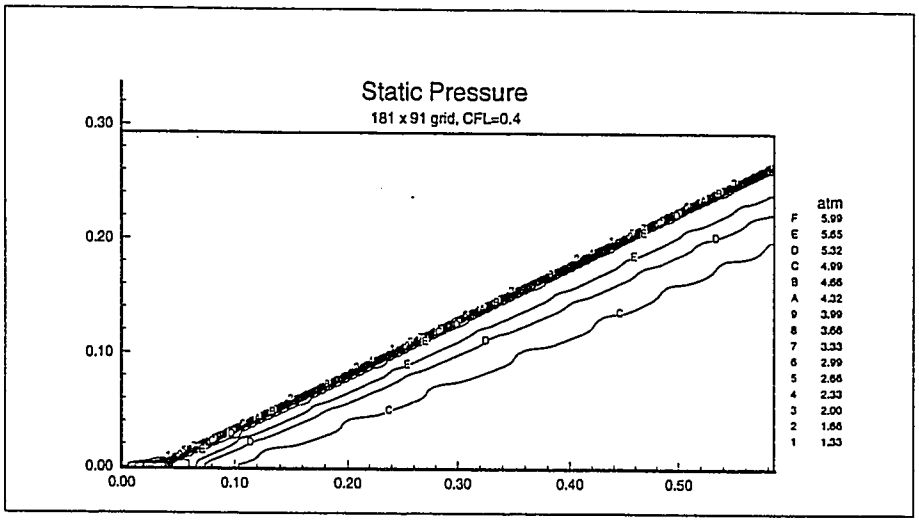

(c)

Figure 5.23: (continued)

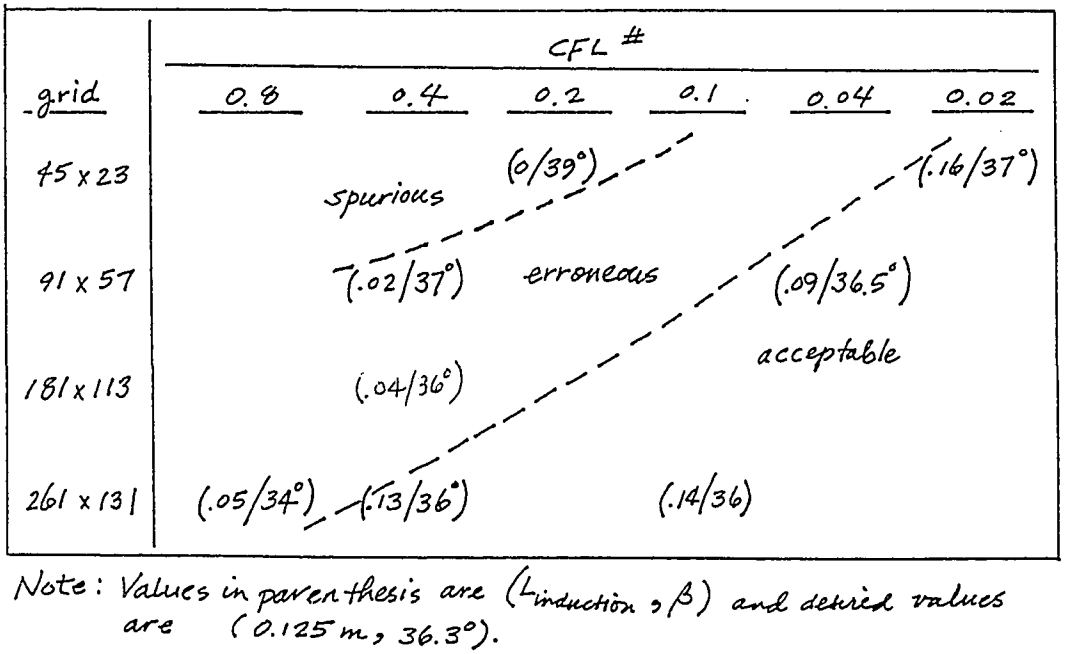

Note: Values in parenthesis are ($L_{induction}$, β) and desired values are (0.125 m, 36.3°).

Figure 5.24: Results of Convergence Study for Skewed-Inflow Configuration

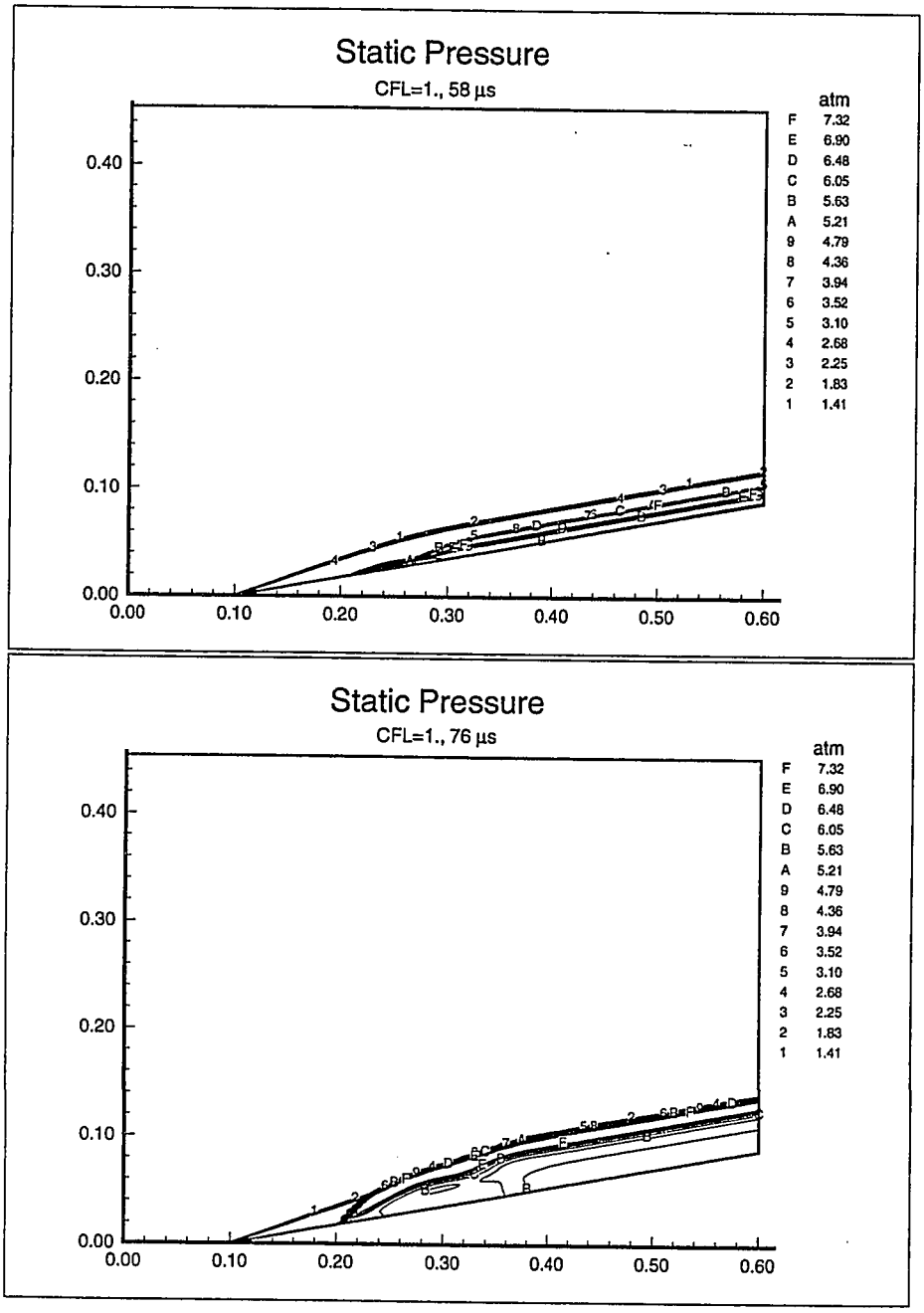

Figure 5.25: Transient Results Leading Up to Underdriven ODW Solution in Figure 5.23

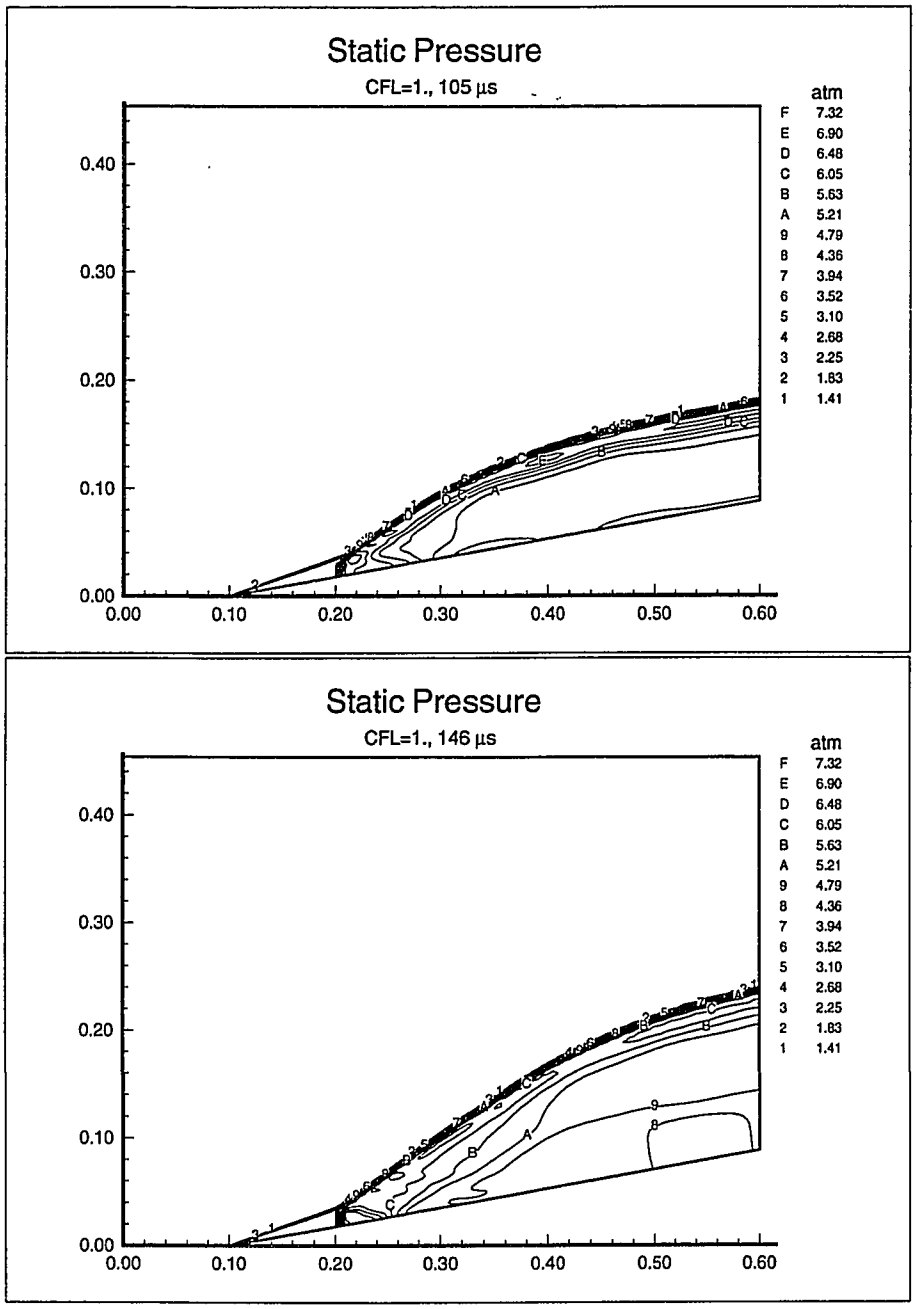

Figure 5.25: (continued)

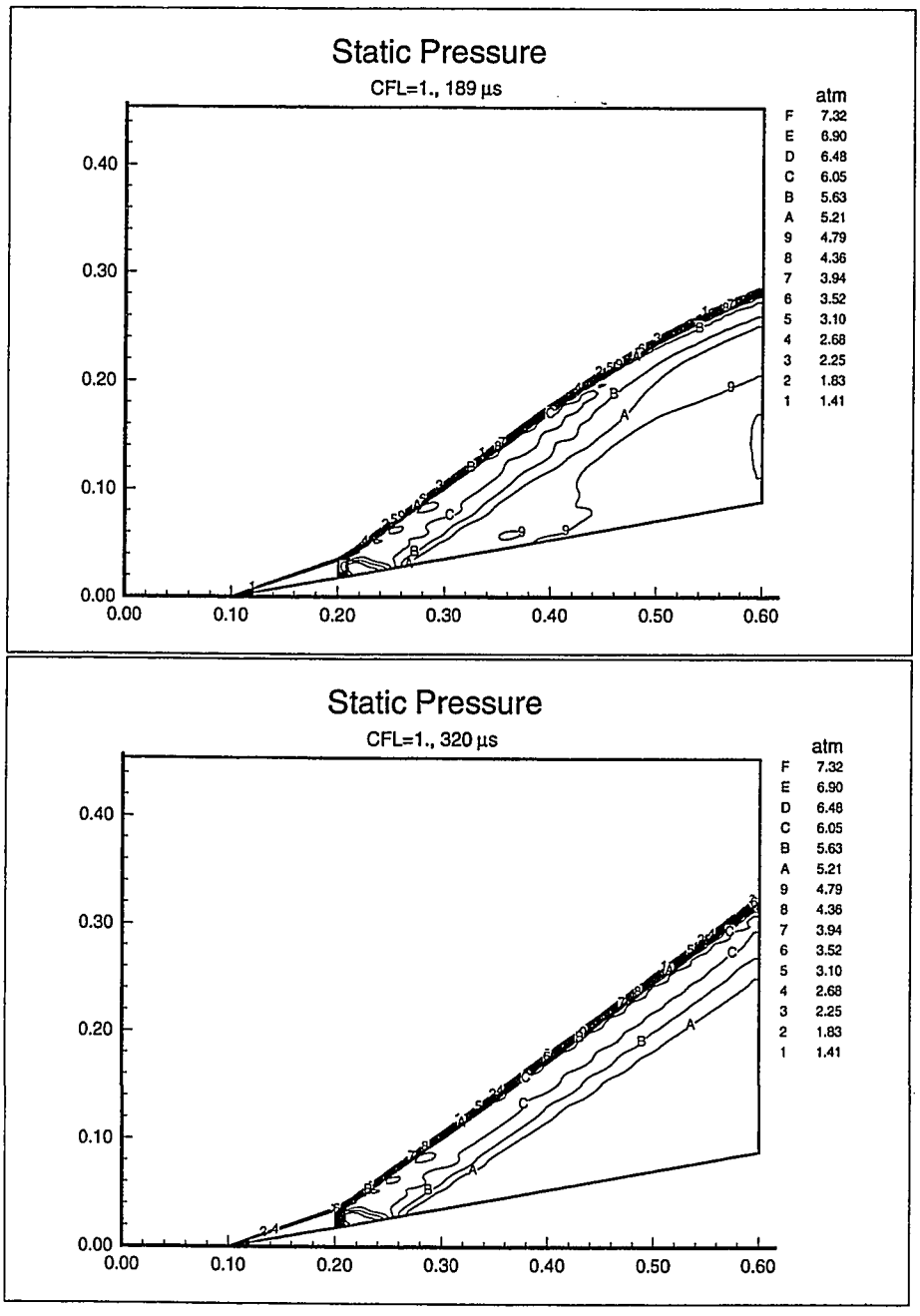

Figure 5.25: (continued)

$76\mu s$ The lead shock remains fixed but the leading edge of the combustion wave has steepened. The induction distance is unchanged at the wall. Farther downstream, the combustion wave has overtaken the oblique shock and the two are coupled. The high pressure region and expansion wave follow closely behind the combustion wave. Note that the pressure in the burned region behind the expansion is beginning to decrease.

$105\mu s$ The deflagration wave at the wall is now near normal. Near the junction of the oblique shock and combustion wave (this will be referred to as the branch point), the detonation is assuming a constant angle. The peak pressure is now limited to a small zone behind the combustion wave at the wall. Immediately behind the high pressure zone, a more complicated arrangement of expansion waves begins to appear. Pressure downstream in the burned gas continues to decrease.

$146\mu s$ The oblique detonation continues to sweep outward and the branch point is now well defined. Pressure behind the developed ODW is further decreased, as is the pressure in the burned gas region downstream of the expansion wave. A now well-defined expansion wave is shown to separate the high pressure zone from the post-ODW flow.

$189\mu s$ Near steady state.

$320\mu s$ Steady state solution.

Following these observations, it is fair to speculate on some causes. The laterally spreading compression/combustion wave observed at $58\mu s$ is a detonation. Its propagation velocity is high enough to move laterally and overtake the oblique shock wave. Once coupled to the oblique shock, it is interesting that the wave is not strengthened. The peak pressure behind the shock is not increased beyond that at $58\mu s$; in fact, it *decreases* as the ODW sweeps out to its final position. The laterally propagating detonation reaches, but does not extend beyond the leading edge of the deflagration wave at the wall. Further propagation upstream is apparently limited because the post-shock flow is superdetonative. The induction time remains fixed next to the wall, as evidenced by the fixed location of the wave. The cause of the steepening of

the deflagration wave away from the wall is not clear, but it seems plausible that the induction time can be decreased with lateral pressure communication. In any case, the near-normal deflagration wave remains at the wall after $100\mu s$. The post-wave pressure is at a maximum there, and is equal to that in the initial high pressure zone behind the laterally spreading detonation (at $58\mu s$).

The flow behind the near-normal deflagration wave differs from that behind the ODW in that the pressure (and density) rise is much higher. Such a difference would normally give a contact surface behind the branch point. However because the flow is overturned through the overdriven ODW, i.e. turned away from the wall, there exists a low pressure region behind the branch point, which separates the overturned flow and the parallel flow behind the normal wave. The expansion wave that emanates from the branch point is the result of flow accelerating from the high pressure, post deflagration wave region to the low pressure region. The reflected expansion turns the entire flow parallel to the wall.

To summarize then, the predicted underdriven detonation wave structure, when taken as a whole, agrees well with that predicted with the /rh/ analysis. Although the overturning through the lead wave results in a subsonic normal flow velocity, the detonation is still isolated from the wall by the expansion fan. How then is it supported? As a test, the solution shown in Figure 5.22 was perturbed by removing the wall downstream of the expansion wave at the wall. Except for the growth in the expansion fan, the wave structure was unchanged. The key to the wave support must lie in the high pressure region formed at the wall behind the deflagration and ahead of the expansion wave. Further work will be required to confirm this hypothesis.

Chapter 6

CONICAL RESULTS

This chapter presents a comparison of Rankine-Hugoniot analyses and two-dimensional finite-difference simulations for axisymmetric conical geometry. The canonical test problem is described first, followed by results of a parametric study which focused on the ODW formation mechanisms and properties.

6.1 Test Problem

Lehr conducted a series of experiments to investigate effects of heat addition in shock-induced combustion [20]. Spherical and conical projectiles 15 mm in diameter were shot into stoichiometric mixtures of hydrogen-oxygen and hydrogen-air at pressures ranging from 0.24 to 0.55 atmospheres. Projectile velocities ranged from 1600 to 2600 m/sec corresponded to Mach numbers ranging from 4.0 to 6.5. Images were recorded of a variety of shock/combustion wave phenomena. For the present work, interest is limited to Lehr's conical projectile results given for Mach numbers of 5.93 and 6.04.

The conditions for Lehr's conical projectile experiment are given in Table 6.1. The free stream temperature calculated from these conditions is $292^{o}K$. The CJ Mach number for the test mixture was 4.86, so both test cases were superdetonative. The photographs recorded by Lehr are shown in Figure 6.1. Distinct shock and combustion fronts can be identified in both cases. The flow field is obviously very sensitive to the inflow Mach number, since small changes in this parameter are accompanied by dramatic changes in wave angle. Lehr references past theoretical work [21, 22] and proposes a model to explain his results. This model consists of a leading shock followed by a conical flow field, in which is contained the deflagration wave and another conical flow field. The amount of heat release dictates the angle of the deflagration, which in turn dictates the angle of the shock.

Lehr's theoretical model and his experimental results pose several difficult questions. In the abstract, the author makes the general statement, presumably applying to all of the results: "the chemical reaction was caused and stabilized by the bow wave

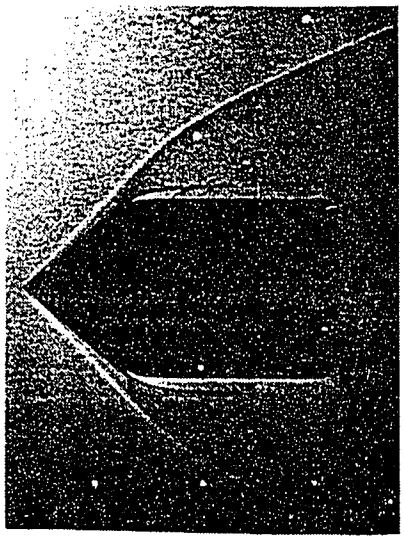

Figure 6.1a: Lehr Experiment, Mach 5.93

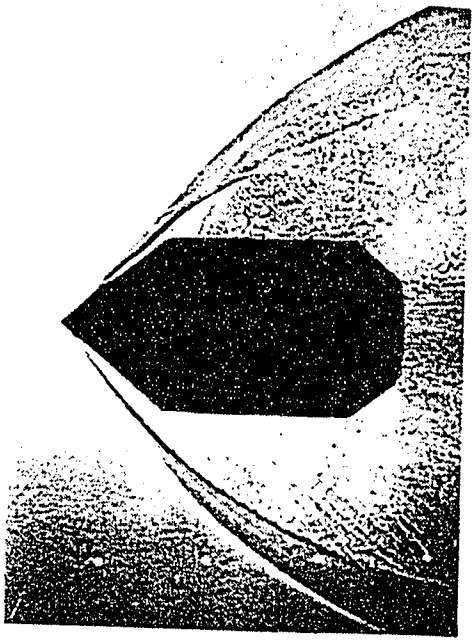

Figure 6.1b: Lehr Experiment, Mach 6.04

Table 6.1: Conditions for Lehr Conical Projectile Experiment

Figure	Velocity (m/sec)	Mach Number
6.1a	2379	5.93
6.1b	2417	6.03

gas mixture: $2H_2 + O_2 + 3.76N_2$
cone half-angle = 37.5°
pressure = 0.555 atm
speed of sound = 403 m/sec
projectile dia. = 15 mm

originating at the tip of the model". Yet tip effects are not included in the model, nor are they included in his explanation of the physics. If the deflagration is caused by bulk ignition after the conical shock, Lehr's model and his experimental results suggest that ignition delay increases with radius. This is true to some extent since the flow is turned to the cone angle, and reaches its maximum pressure, through longer distances, and therefore longer times. This needs to be investigated by integrating the rate equations along a series of streamlines passing through the shock at various radii.

In any event, Lehr's results are a good test problem for conical shock induced combustion, however the present research is directed at detonation phenomena. So in addition to the experimental geometry, simulations were performed at an increased scale to give a Damköhler number sufficient to produce an ODW. Attention will be limited to Lehr's Mach 5.93 experiment. For that case, Da was calculated from chemical induction time and fluid residence time behind a non-reactive shock. The induction time ranges from 6 μs for cone surface conditions to 8 μs for post-shock conditions. Fluid residence time is 7 μs based on the length of the cone surface. The Damköhler number for this case is then roughly 1. This is consistent with the absence of an ODW in Lehr's results, and explains why the slight increase in Mach number (and consequent increase in Da) results in large changes in the angle of the shock and deflagration waves. For a unit Damköhler number, the combustion may be quenched in the expansion fan over the shoulder of the projectile; even a small

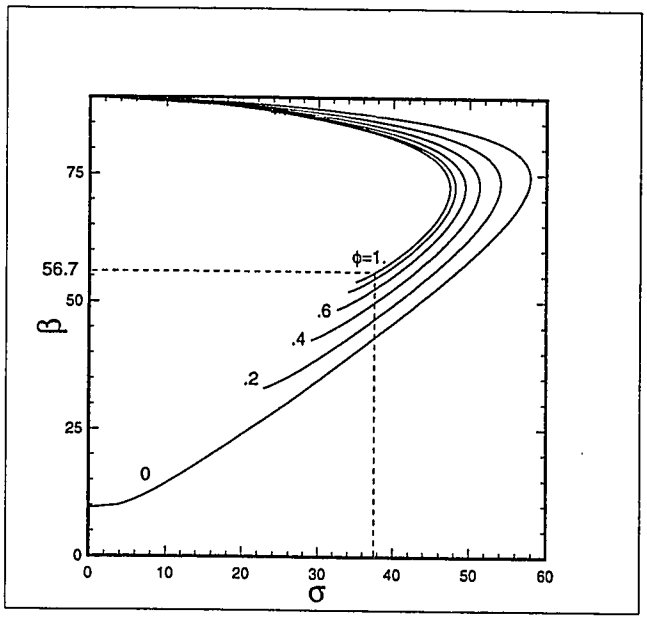

Figure 6.2: Stability Map for Conical Test Problem, hydrogen-air at $292^{o}K$, 0.555 atm, Mach 5.93 (ϕ = equivalence ratio)

increase in Da could result in a large increase in heat release over the cone surface, which may not be sufficient to produce an ODW, but would produce large changes in the wave angles.

6.2 Rankine-Hugoniot Analysis

A stability map was produced for the conical test problem and the results are shown in Figure 6.2. *If* an ODW forms, the 37.5° cone angle and unit equivalence ratio require an attached, weak overdriven wave with an angle of 56.7°. The shock wave in Figure 6.1a measures 47°, slightly greater than the 43.5° value for a non-reactive wave, but no where near the value for the ODW.

Jump conditions predicted with the Rankine-Hugoniot model are given in Table 6.2. For the conical flow solution in the Rankine-Hugoniot model, mixture properties are held constant at post-ODW, equilibrium values. Shifting equilibrium that would occur between the ODW and the cone surface is not included in the model. It is for

this reason that H_2O mass fraction is shown constant in Table 6.2.

Table 6.2: Rankine-Hugoniot Property Jumps Over ODW for Conical Test Problem

Property	upstream	post-ODW	cone surface
Mach number	5.93	1.40	1.26
temperature, ^oK	292	2986	3104
pressure, atm	.555	10.87	13.23
density, kg/m^3	.4844	1.053	1.233
mass frac. H_2O	.0	.214	.214

6.3 Validation Against Experiment

Lehr's experimental results provide an opportunity to validate the simulation model, albeit for shock-induced combustion rather than an ODW.

6.3.1 Lehr Experiment - Mach 5.93

The Mach 5.93 experiment is considered first. The 81 x 91 grid used for this case is shown in Figure 6.3. The laminar solution results at 14 μs are given in Figure 6.4 and the convergence history in Figure 6.5. This simulation consumed nearly 150 hours of CPU time on a Sun SPARCstation 2. The results can be compared directly with Lehr's experimental result in Figure 6.1a. The agreement is generally good, shock curvature is close and the deflagration on the centerbody is similar in extent. However the predicted wave angle is that for a non-reactive wave (43.5°), while Lehr reports 47° for the experimental results.

The most likely explanation for the difference between the predicted and experimentally observed wave angle is a deficient model of the boundary layer on the cone surface. The predicted boundary layer on the cone surface is visibly thinner than in the experiment. A thicker boundary layer envelops, and will burn, a larger volume of the flow. A deflagration of sufficient thickness will displace the shock outward. Laminar fluid properties are probably adequate since the Reynolds number at the top of the cone is 650,000. However, the boundary layer is inadequately resolved

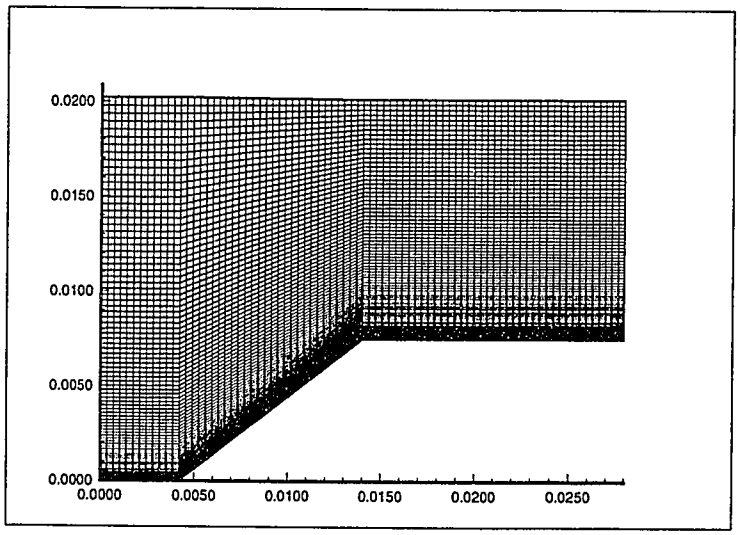

Figure 6.3: 81 x 91 Grid for Full Scale Conical Test Problem, dimensions in meters

with at most two grid cells (estimated boundary layer thickness at the top of the cone is .01 mm, minimum grid cell thickness is .006 mm). An improved grid is also required that is orthogonal to the cone surface since the thin layer approximation is being used.

A second possibility is that the chemical mechanism is not appropriate. Kinetic rate data have large uncertainties and the simple change to another chemical mechanism can sometimes produce significant changes. The simulation could be repeated with available hydrogen-air mechanisms as a test of this hypothesis.

A third and final possibility is that the projectile tip effects are important. Even a well machined tip is blunt at a small scale and the wave will be detached. Although it would quickly decay to an oblique shock, the detached wave will burn a larger volume of fluid. This effect could be enhanced by high stagnation temperatures that may cause tip erosion even during a brief experiment.

6.4 Overdriven Wave Simulations

To produce a conical ODW, the Damköhler number will have to be increased significantly. The results for a 10 : 1 scaling of experimental problem geometry will be

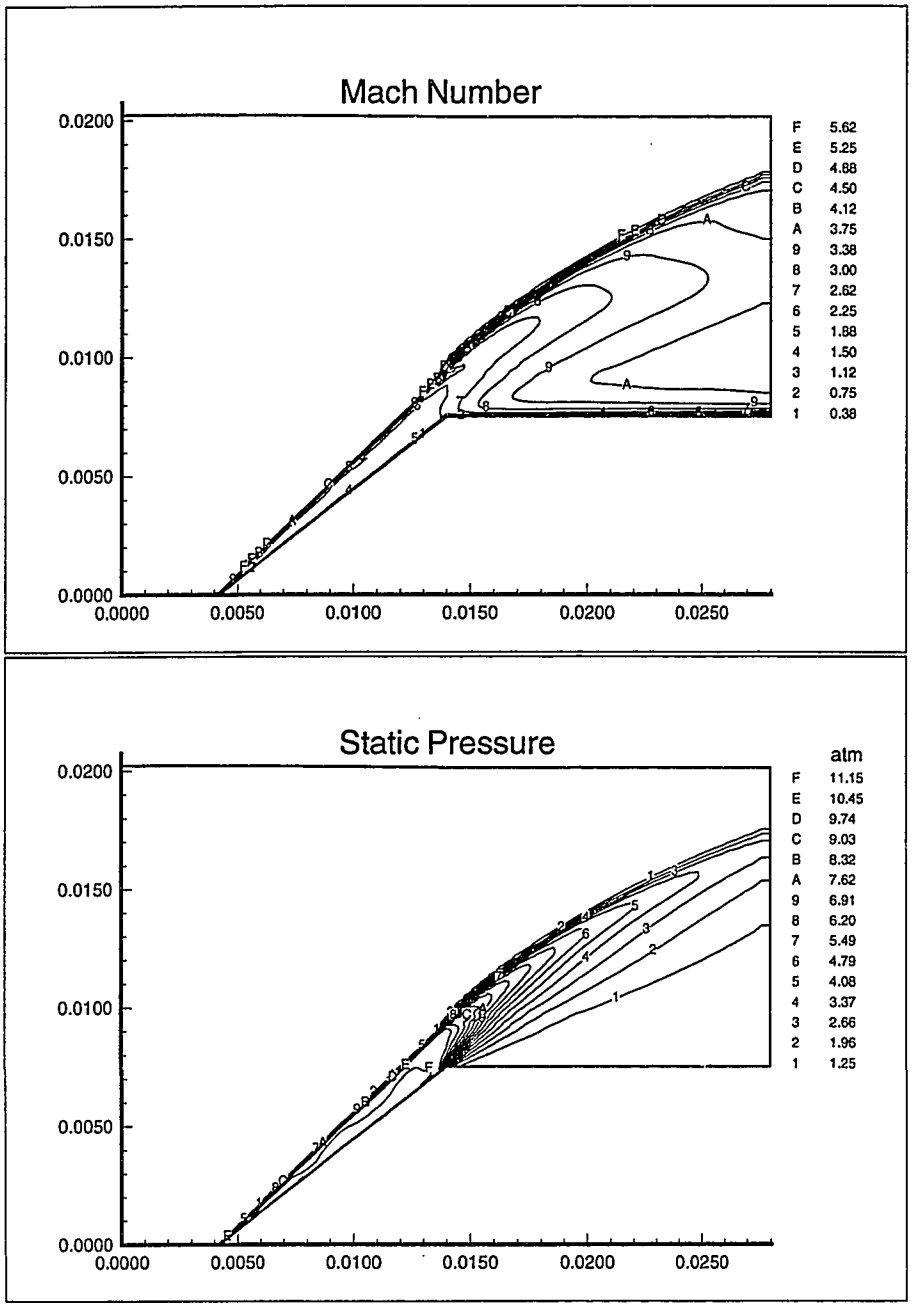

Figure 6.4: Laminar Solution at 14 μs for Full Scale Conical Test Problem

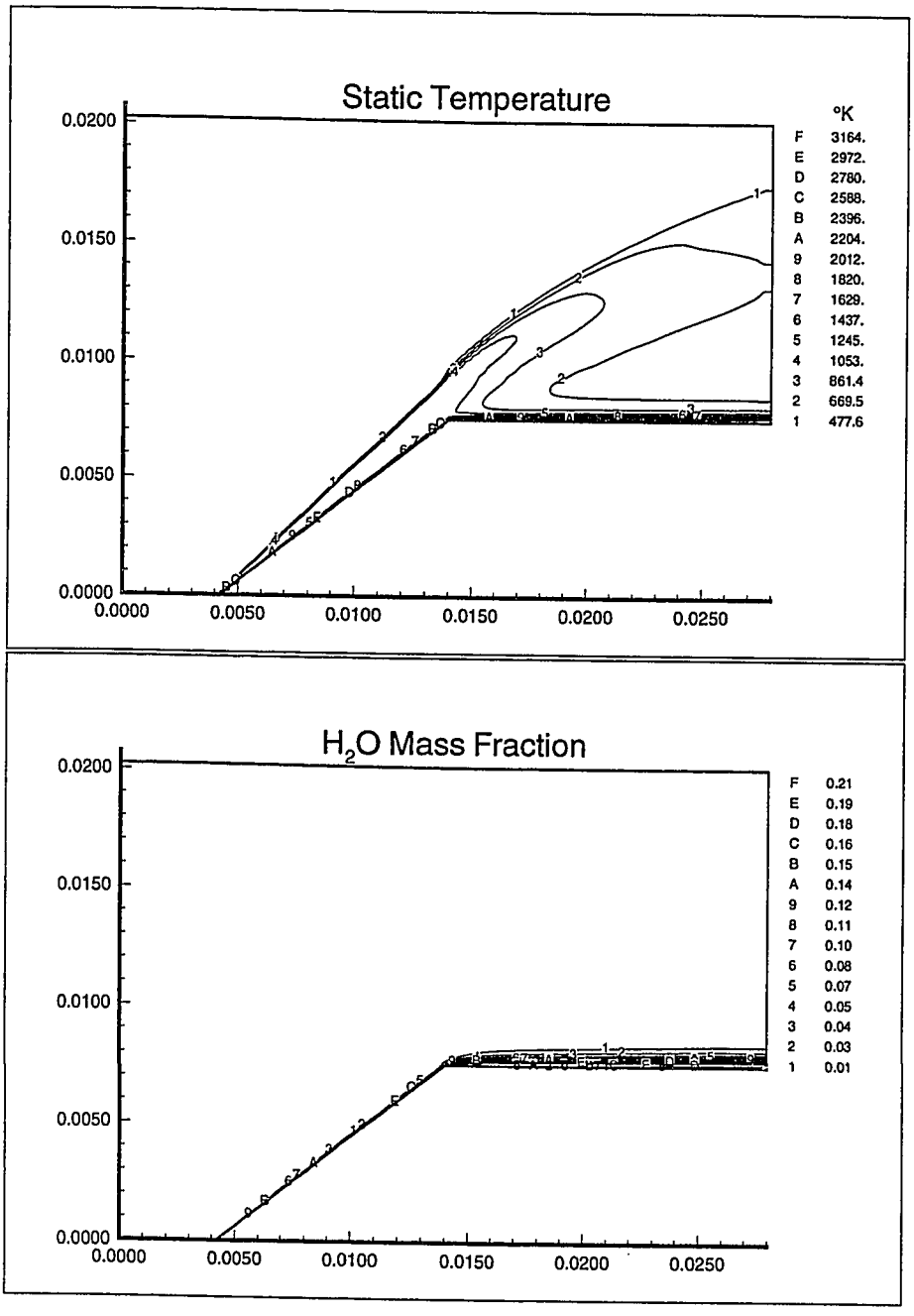

Figure 6.4: (continued)

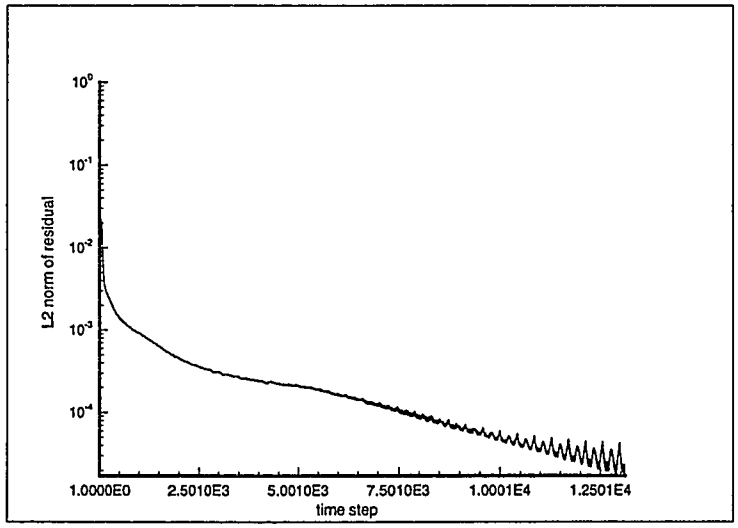

Figure 6.5: Convergence History for Full Scale Conical Test Problem

presented first, followed by predictions for the actual geometry.

The 41 x 76 grid used for the 10 : 1 scale conical test problem is shown in Figure 6.6. The computational domain is limited to the ramp to minimize the computational effort. Grid trajectories are far from orthogonal along the cone surface because of the large cone half angle. While this should present no problem for the inviscid simulations, it may limit the accuracy of the viscous simulation as will be discussed later.

The inviscid 10 : 1 scale solution was much more difficult to achieve than any planar simulation that was run. Simulations initialized with the full 37.5° ramp angle would not converge. The time consuming, but successful, procedure of incrementally increasing ramp angle during the solution was adopted for all inviscid conical simulations. The general procedure was to begin with a 20° cone half angle and advance to the full angle in at most 5° increments; 100 time steps were taken at each wave angle. The solution could then be advanced to a steady state.

The inviscid 10 : 1 scale solution at a cumulative simulated time of 180 μs is given in Figure 6.7. The 56° wave angle agrees very well with the 56.7° value from the Rankine-Hugoniot analysis. Table 6.3 gives predicted post-ODW and cone surface properties for comparison with the values in Table 6.2. Post-ODW properties agree

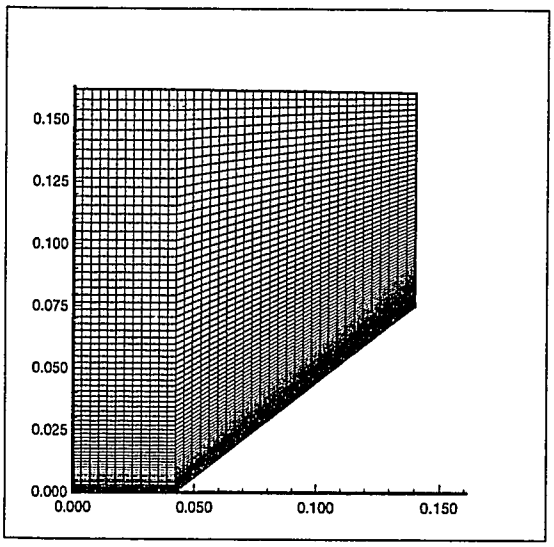

Figure 6.6: 41 x 76 Grid for 10 : 1 Scale Conical Test Problem, dimensions in meters

to within 3 percent except mixture density, which shows a 10 percent difference. The data location is a factor in these differences; the post-ODW grid point was chosen by visual inspection of the H_2O mass fraction contour plot in Figure 6.7. Differences in cone surface properties range from 7 percent for Mach number to less than 2 percent in pressure. The failure to model shifting equilibrium in the Rankine-Hugoniot model may be a factor in these differences, however, the numerical predictions indicate little change in mixture composition. In general, the conical simulation results show less agreement with the theory than the planar simulation results.

The 10 : 1 scale inviscid solution represents a considerable computational effort. The 180 μs of simulation time required over 15,000 time steps and 44.5 hours of CPU time on a Sun SPARCstation 2. The convergence history is shown in Figure 6.8. For planar simulations, two methods were demonstrated for accelerating convergence. The skewed inflow grid configuration cannot model the centerline boundary condition for the conical geometry and is therefore not an option. Local time stepping failed to converge. This latter problem may be due to the approximate treatment of the centerline boundary condition (see Section 4.6.4) or it may be a result of stiffness associated with the axisymmetric source term. Whatever the cause, an efficient solution procedure was not found for the axisymmetric test problem.

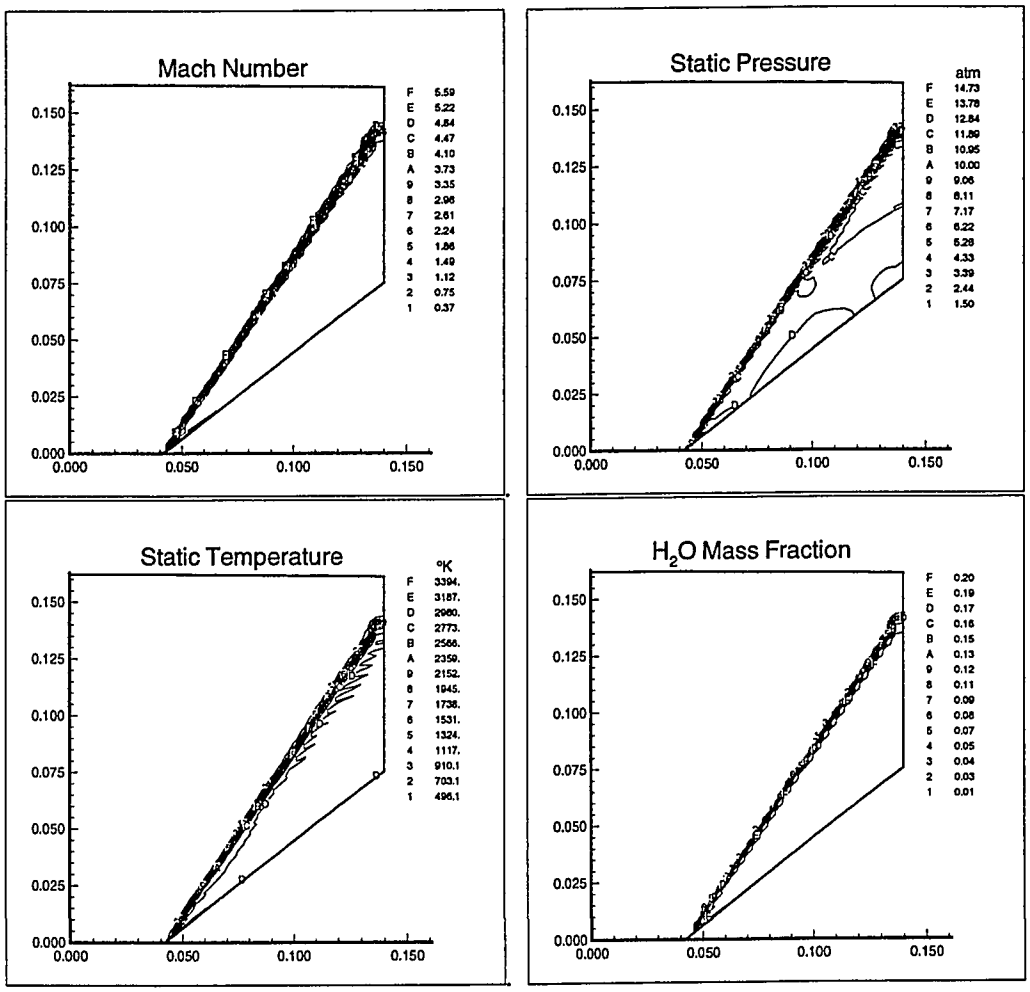

Figure 6.7: Inviscid Solution for 10 : 1 Scale Conical Test Problem

Table 6.3: Predicted post-ODW and Cone Surface Properties for 10 : 1 Scale Conical Test Problem, Simulation Results from Figure 6.7 at grid points (22,25) and (40,1).

Property	post-ODW	cone surface
Mach number	1.36	1.35
temperature, ^oK	2949	2956
pressure, atm	11.0	13.0
density, kg/m^3	1.16	1.26
mass frac. H_2O	.2072	.2075

The laminar solution was easier to produce since it would converge when initialized with the full 37.5° cone half angle. The only compromise was that the simulation began in a non-reactive mode. Results for the laminar simulation at 170 μs are presented in Figure 6.9. The convergence history is shown in Figure 6.10. A slightly shorter grid was used for this case (41 x 71), but with identical grid cell spacing. The laminar case was actually run before the inviscid case, and the computational domain was extended to avoid the Mach reflection from forming on the upper boundary. Agreement between the inviscid and laminar solutions is excellent; both give a wave angle of 56°. This was the same finding for the large Damköhler number case for the planar geometry; the viscous boundary layer has no influence on the ODW for large Da since formation is determined by bulk ignition.

This finding is tempered by the fact that the boundary layer is not resolved and should be turbulent. The Reynolds number based on the cone surface length is 6.5 million, well into the turbulent range. The model uses laminar fluid properties, which should give a boundary layer thickness of .03 mm at the end of the cone. The minimum grid cell spacing is .06 mm, so there is no hope of resolving the boundary layer. In fact it is artificially thickened. That the use of a well resolved, turbulent boundary layer will not alter the results is supported by the planar simulation results.

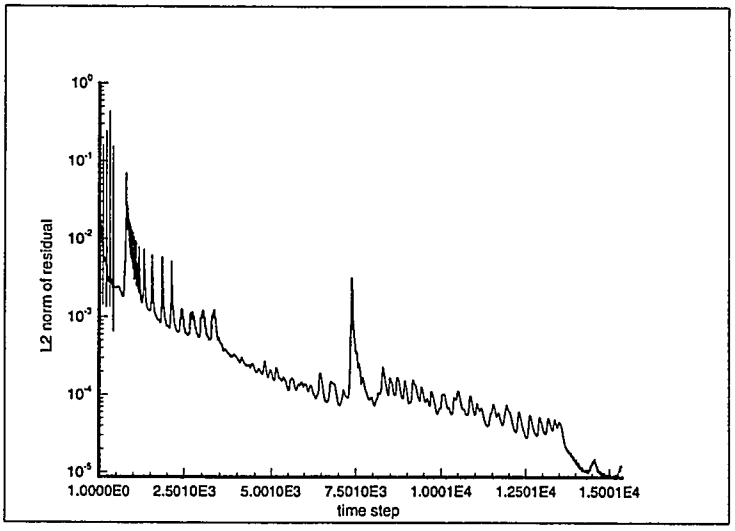

Figure 6.8: Convergence History for Inviscid 10 : 1 Scale Test Problem

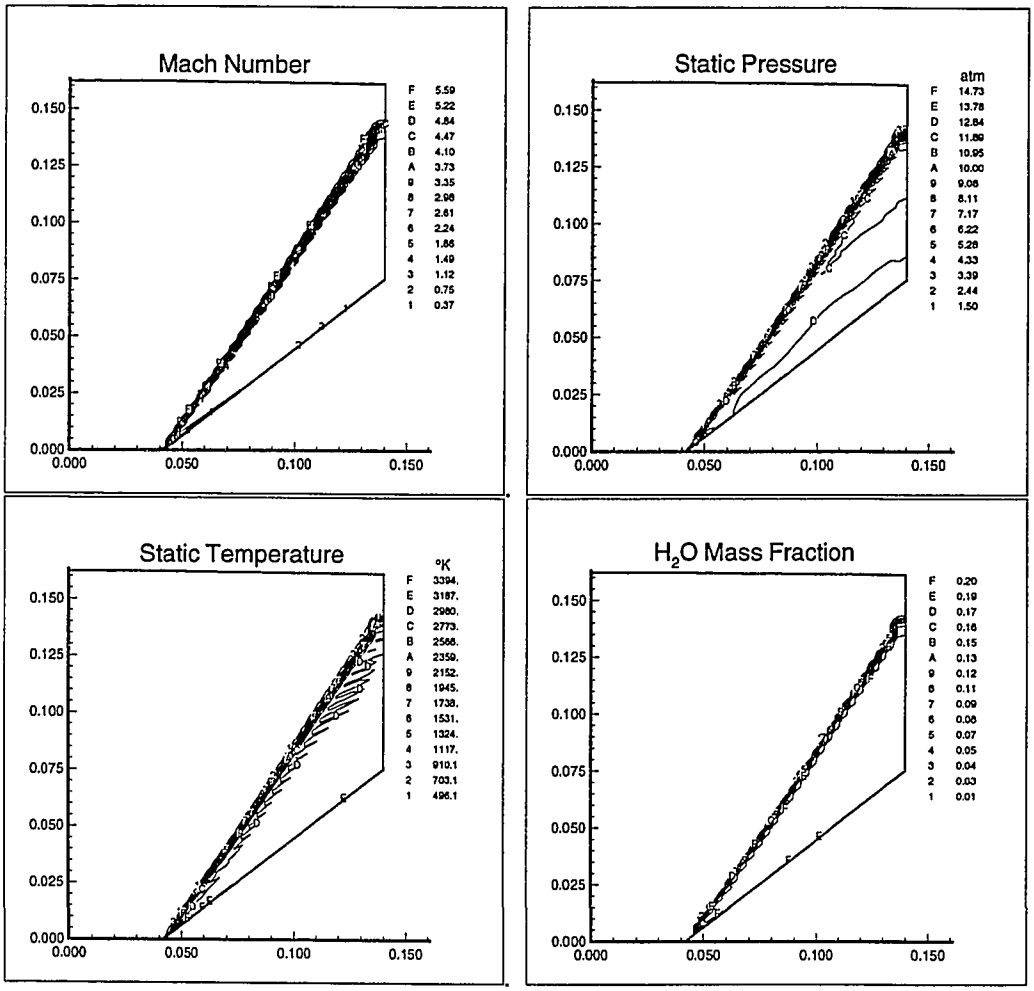

Figure 6.9: Laminar Solution for 10 : 1 Scale Conical Test Problem

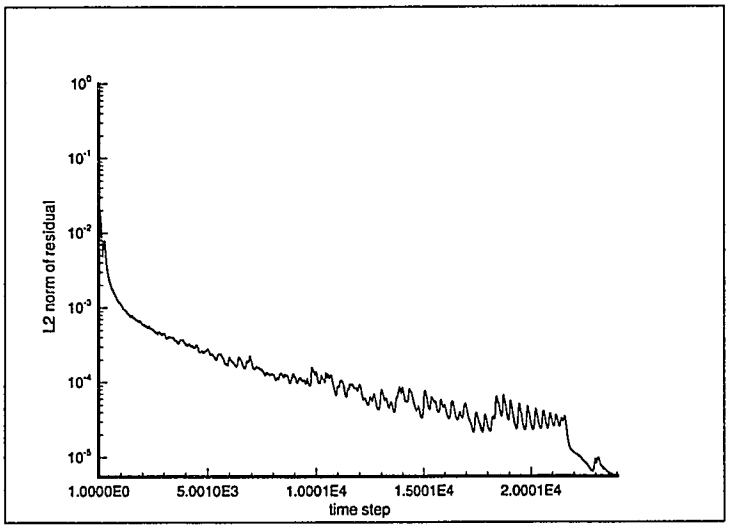

Figure 6.10: Convergence History for Laminar 10 : 1 Scale Test Problem

Chapter 7

CONCLUSIONS

Lacking finite rate chemistry and other important effects, Rankine-Hugoniot analysis is insufficient to predict the occurrence of an oblique detonation wave (ODW). While multi-dimensional CFD codes are limited by the accuracy of their physical models and numerical solution schemes, they do have the potential to include these important effects and to predict the limits of ODW formation. The numerical model developed in the present research predicts planar and conical ODWs under a variety of conditions.

The Damköhler number is important in the formation of an ODW. ODWs were routinely predicted for Da on the order of 10. The formation mechanism in this case is bulk ignition due to adiabatic compression in the shock. For Da as small as 2, ODWs formed over at least a portion of the wave. If an ODW formed in an inviscid simulation, it was always present in the viscous simulation. The effect of viscosity is confined to the boundary layer, which contains a burned-gas layer. For the cases investigated, the boundary layer had no effect on ODW formation or position once formed. This conclusion corrects earlier published results showing a strong effect of viscosity.

Rankine-Hugoniot jump conditions for ODWs were used as a basis of comparison with code-predicted jumps and wave angle. Planar Rankine-Hugoniot solutions were obtained with a previously developed model that solves the oblique shock relations with heat release and temperature dependent fluid properties. This model was coupled to a conical flow solution in the present research to obtain Rankine-Hugoniot solutions for conical ODWs. Agreement between these solutions and numerical predictions was very good for planar geometry, jump conditions being within 2 percent for cases considered. Agreement was poorer for the conical geometry, with maximum differences in jump conditions ranging between 7 and 10 percent, although wave angles agreed within 1°.

Solutions were produced for an underdriven weak oblique detonation wave. Un-

derdriven weak oblique detonation waves have previously been dismissed as physically impossible, however these conclusions were always based on a single compression-heat release wave. A combined wave model, consisting of a compression wave with heat release followed by an expansion wave, is proposed as a possible explanation for these results. Although the underdriven ODW solution presented is supported by considerable numerical experimentation, further analysis will be required for this solution to be either accepted as physically possible or for it to be dismissed as a spurious numerical result.

Two methods were demonstrated for improving the computational efficiency of planar steady state, inviscid simulations: local time stepping and an alternative computational grid. Only the first option is available for viscous simulations because of the need to resolve wall boundary layers. Neither of these methods were successfully applied to the axisymmetric simulations.

Simulations of a shock-induced combustion experiment for a conical projectile showed general agreement with flow features, but underpredicted the shock angle. Reasons postulated for this difference included inadequate boundary layer resolution, lack of grid orthogonality at the cone surface, and an inappropriate chemical mechanism.

Chapter 8

RECOMMENDATIONS

The results presented in this dissertation by no means represent the final word on attached oblique detonation waves. Further research is needed to develop ideas introduced here. The topic of underdriven ODWs is particularly intriguing and needs to be considered from both an analytical and numerical standpoint. The impact of equilibrium chemistry and viscous flow properties are recommended as areas to explore in numerical simulations. The influence of viscous flow phenomena on ODWs in general should be explored further. Although thin laminar boundary layers had no apparent affect, thick turbulent boundary layers may have a role in ODW formation and stability.

More work is needed in modeling conical detonation waves. Better agreement with the Lehr experiment should be a first goal. Possible approaches include trying different chemical mechanisms and use of a refined orthogonal grid to better model the boundary layer on the cone surface. Tip effects may also be important and may need to be modeled in detail. Progress on this problem was limited by large CPU investment for each solution. A means of accelerating convergence to a steady state is required; as a first step in this regard is to determine the failure mode of local time stepping in the axisymmetric geometry. Finally, underdriven waves should be included in the Rankine-Hugoniot analyses and simulations representative cases should be attempted.

BIBLIOGRAPHY

[1] O'Brien, C. J. and Kobayashi, A. C., "Advanced Earth-to-Orbit Propulsion Concepts," Paper No. AIAA-86-1386, AIAA/ASME/SAE/ASEE 22nd Joint Prop. Conference, Huntsville, AL, June 16–18, 1986.

[2] Dunlap, R., Brehm, R. L. and Nicholls, J. A., "A Preliminary Study of the Application of Steady- State Detonative Combustion to a Reaction Engine," *Jet Propulsion*, **28**, 7, July 1958, pp. 451–456.

[3] Morrison, R. B., "Oblique Detonation Wave Ramjet," NASA Contractor Report 159192, January 1980.

[4] Rubins, P. M. and Bauer, R. C., "A Hypersonic Ramjet Analysis with Premixed Fuel Combustion," Paper No. AIAA-66-648, AIAA 2nd Propulsion Joint Specialist Conference, Colorado Springs, Colorado, June 13–17, 1966.

[5] Jachimowski, C. J., "An Analytical Study of the Hydrogen-Air Reaction Mechanism With Application to Scramjet Combustion," NASA TP- 2791, February 1988.

[6] Hertzberg, A., Bruckner, A. P. and Bogdanoff, D. W., "Ram Accelerator: A New Chemical Method for Accelerating Projectiles to Ultrahigh Velocities," *AIAA J.*, Vol. 26, No. 2, 1988, pp. 195–203.

[7] Yungster, S. and A. P. Bruckner, "Computational Studies of a Superdetonative Ram Accelerator Mode," *J. Propulsion*, Vol. 8, No. 2, 1992, pp. 457–463.

[8] Westbrook, C. K., "Hydrogen Oxidation Kinetics in Gaseous Detonations," *Combustion Science and Technology*, vol. 29, pp. 67–81, 1982.

[9] Glenn, D. E. and D. T. Pratt, "Numerical Modeling of Standing Oblique Detonation Waves," Paper No. AIAA-88-0440, AIAA 26th Aerospace Sciences Meeting, Reno, Nevada, January 11–14, 1988.

[10] Cambier, Jean-Luc, Adelman, H. G. and Menees, G. P., "Numerical Simulations of Oblique Detonations in Supersonic Combustion Chambers," *J. Propulsion*, Vol. 5, No. 4, 1989, pp. 482–491.

[11] Fort, J. A. and Pratt, D. T., "Supersonic Flameholding by Attached Oblique Shock Waves," Paper No. AIAA-90-0735, AIAA 28th Aerospace Sciences Meeting, Reno, Nevada, January 8–11, 1990.

[12] Fort, J. A. and Pratt, D. T., "Conical Detonation Waves - A Comparison Between Theoretical and Numerical Results," Paper No. AIAA-92-0348, AIAA 30th Aerospace Sciences Meeting, Reno, Nevada, January 6–9, 1992.

[13] Li C., K. Kailasanath, and E. S. Oran, "Stability of Oblique Detonations in Ram Accelerators," Paper No. AIAA-92-0089, AIAA 30th Aerospace Sciences Meeting, Reno, Nevada, January 6–9, 1992.

[14] Li C., K. Kailasanath, and E. S. Oran, "Effects of Boundary Layers on Oblique-Detonation Structures," Paper No. AIAA-93-0450, AIAA 31st Aerospace Sciences Meeting, Reno, Nevada, January 11–14, 1993.

[15] Pratt, D. T., J. W. Humphrey and D. E. Glenn, "Morphology of Standing Oblique Detonation Waves," *J. Propulsion*, vol. 7, no. 5, pp. 837–845, Sept.-Oct. 1991.

[16] Strehlow, R.A., *Combustion Fundamentals*, McGraw-Hill, 1984.

[17] Davis, William C., "The Detonation of Explosives," *Scientific American*, Vol. 256, No. 5, pp. 106–112, May 1987.

[18] Fickett, Wildon, "Detonation in Miniature," Chap. 4 in *The Mathematics of Combustion*, J. D. Buckmaster, ed., SIAM, 1985.

[19] Liepmann, H.W. and A. Roshko, *Elements of Gasdynamics*, J. Wiley, 1957.

[20] Lehr, H., "Experiments on Shock-Induced Combustion," *Astronautica Acta*, **17**, 1972, pp. 589–597.

[21] Kvashnina, S. S. and Chernyi, G. G., "Steady State Flow of a Detonating Gas Around a Cone," *Journal of Applied Mathematics and Mechanics*, Vol. 23, pp. 252–259, 1959.

[22] Woolard, H. W., "Analytical Approximations for Stationary Conical Detonations and Deflagrations in Supersonic Flow," Applied Physics Lab., The Johns Hopkins University, TG-446, 1963.

[23] Yee, H. C., "Construction of Explicit and Implicit Symmetric TVD Schemes and Their Applications," *Journal of Computational Physics*, Vol. 68, pp. 151–179, 1987.

[24] Yee, H. C., "Numerical Experiments with a Symmetric High-Resolution Shock-Capturing Scheme," Proc. of the 10th Intl. Conf. on Numerical Methods in Fluid Dynamics, June 23–27, 1986, Beijing, published in *Lecture Notes in Physics*, Springer Verlag.

[25] Oran, E. S. and J. P. Boris, *Numerical Simulation of Reacting Flow*, Elsevier, New York, 1987.

[26] Roe, P.L., "Characteristic-Based Schemes for the Euler Equations",Ann. Rev. Fluid Mechanics,**18**, 337-365, 1986.

[27] Yee, H. C., "Upwind and Symmetric Shock-Capturing Schemes," NASA Technical Memorandum 89464, May 1987.

[28] Harten, A., "High Resolution Schemes for Hyperbolic Conservation Laws", Jour. Computat. Phys.,**49**, 357-393, 1983.

[29] Shuen, J. S., M. S. Liou and B. van Leer, "Inviscid Flux Splitting Algorithms for Real Gases with Non-equilibrium Chemistry," *Journal of Computational Physics*, Vol. 90, pp. 371–395, 1990.

[30] Eberhardt, D. S., Course Notes for AA510, Computational Fluid Dynamics, Aeronautics and Astronautics Dept., University of Washington, 1988.

[31] Glassman, I., *Combustion*, Academic Press, 1987.

[32] Radhakrishnan, K. and Pratt, D. T., "Fast Algorithm for Calculating Chemical Kinetics in Turbulent Reacting Flow," *Combust. Sci. and Tech.*, 1988, Vol. 58, pp 155–176.

[33] Gordon, S., and B. J. McBride, "Computer Program for Calculation of Complex Chemical Equilibrium Compositions, Rocket Performance, Incident and Reflected Shocks, and Chapman Jouget Detonations," NASA SP-273, 1976.

[34] Waldman, Wilson and Maloney, Environmental Protection Technology Series, EPA-650/2-74-045, 1974.

[35] Gordon, S., McBride, B. J., and Zeleznik, F. J., "Computer Program for Calculation of Complex Chemical Equilibrium Compositions and Applications, Supplement I—Transport Properties," NASA Tech. Memorandum 86885, October 1984.

[36] Sutherland, William, "The Viscosity of Mixed Gases," *Phil. Mag.*, **40**, 1895, pp. 421–431.

[37] Wassiljewa, A., "Heat-Conduction in Gaseous Mixtures," *Phys. Z.*, **5**, 1904, pp. 737–742.

[38] Wilke, C. R., "A Viscosity Equation for Gas Mixtures," *J. Chem. Phys.*, **18**, no. 4, April 1950, pp. 517–519.

[39] Vanderslice, J. T., et al., "High-Temperature Transport Properties of Dissociating Hydrogen," Phys. Fluids, *5*, no. 2, Feb. 1962, pp. 155–164.

[40] Welty, James R., Charles E. Wicks and Robert E. Wilson, *Fundamentals of Momentum, Heat and Mass Transfer*, second ed., Wiley, 1976.

[41] Bird, R. Byron, Warren E. Stewart and Edwin N. Lightfoot, *Transport Phenomena*, Wiley, 1960.

[42] Pulliam, T. H. and J. L. Steger, "Recent Improvements in Efficiency, Accuracy, and Convergence for Implicit Approximate Factorization Algorithms," Paper No. AIAA-85-0360, AIAA 23rd Aerospace Sciences Meeting, Reno, Nevada, January 14–17, 1985.

[43] Roache, P. J., *Computational Fluid Dynamics*, Hermosa Publishers, Albuquerque, 1985.

[44] Amsden, A. A., H. M. Ruppel and C. W. Hirt, "SALE: A Simplified Arbitrary Lagrangian- Eulerian Computer Program for Fluid Flow at All Speeds," Los Alamos National Laboratory Report LA-8095, UC-32, June 1980.

[45] Oran, E. S., Boris, J. P., Young, T., Flanigan, M., Burks, T. and Picone, M., "Numerical Simulations of Detonations in Hydrogen-air and Methane-air Mixtures," *Eighteenth Symposium (International) on Combustion*, The Combustion Institute, 1981, pp. 1641–1649.

[46] Shuen, J.S. and S. Yoon, "Numerical Study of Chemical Reacting Flows Using an LU Scheme," Paper No. AIAA-88-0436, AIAA 26th Aerospace Sciences Meeting, Reno, Nevada, January 11–14, 1988.

[47] Siestrunck, R., Fabri, J., and LeGriveś, E., "Some Properties of Stationary Detonation Waves," Fourth Symposium (International) on Combustion, Williams and Wilkins, Baltimore, 1953, pp. 498-501.

[48] Powers, J. M. and K. A. Gonthier, "Reaction Zone Structure of Weak Underdriven Oblique Detonations," Paper No. AIAA-92-0347, AIAA 30th Aerospace Sciences Meeting, Reno, Nevada, January 6–9, 1992.

[49] Shapiro, A. H., *The Dynamics and Thermodynamics of Compressible Fluid Flow*, Wiley, 1953.

[50] Anderson, Dale A., Tannehill, John C. and Pletcher, Richard H., *Computational Fluid Mechanics and Heat Transfer*, Hemisphere, 1984.

Appendix A

DERIVATION OF GOVERNING EQUATIONS

Two coordinate geometries are considered, planar and axisymmetric. In all cases only the laminar form of the equations are treated.

A.1 2-D Planar Geometry

Anderson, Tannehill and Pletcher [50, pp. 479–481] give the compressible Navier-Stokes equations in Cartesian coordinates without body forces or external heat addition. Modified for a mixture of N species in two dimensions, these equations become,

$$\frac{\partial Q}{\partial t} + \frac{\partial F}{\partial x} + \frac{\partial G}{\partial y} = 0 \tag{A.1}$$

where Q is the vector of conserved variables and F and G are the flux vectors,

$$Q = \begin{bmatrix} \rho_1 \\ \rho_2 \\ \vdots \\ \rho_N \\ \rho u \\ \rho v \\ E \end{bmatrix} \tag{A.2}$$

$$F = \begin{bmatrix} \rho_1 u \\ \rho_2 u \\ \vdots \\ \rho_N u \\ \rho u^2 + p - \tau_{xx} \\ \rho uv - \tau_{xy} \\ u(E+p) - u\tau_{xx} - v\tau_{xy} + q_x \end{bmatrix} \tag{A.3}$$

$$G = \begin{bmatrix} \rho_1 v \\ \rho_2 v \\ \vdots \\ \rho_N v \\ \rho uv - \tau_{xy} \\ \rho v^2 + p - \tau_{yy} \\ v(E+p) - u\tau_{xy} - v\tau_{yy} + q_y \end{bmatrix} \tag{A.4}$$

where components of the shear stress tensor and heat-flux vector are,

$$\tau_{xx} = \frac{2}{3}\mu\left(2\frac{\partial u}{\partial x} - \frac{\partial v}{\partial y}\right)$$

$$\tau_{yy} = \frac{2}{3}\mu\left(2\frac{\partial v}{\partial y} - \frac{\partial u}{\partial x}\right)$$

$$\tau_{xy} = \mu\left(\frac{\partial u}{\partial y} + \frac{\partial v}{\partial x}\right) = \tau_{yx} \tag{A.5}$$

$$q_x = -k\frac{\partial T}{\partial x}$$

$$q_y = -k\frac{\partial T}{\partial y}$$

A more useful form of equations (A.1) through (A.5) is obtained by the transformation to a generalized nonorthogonal curvilinear coordinate system (ξ, η),

$$\xi = \xi(x, y, t) \tag{A.6}$$

$$\eta = \eta(x, y, t) \tag{A.7}$$

$$t = t \tag{A.8}$$

By chain rule,

$$\frac{\partial Q}{\partial t} = \frac{\partial Q}{\partial t} + \frac{\partial Q}{\partial \xi}\frac{\partial \xi}{\partial t} + \frac{\partial Q}{\partial \eta}\frac{\partial \eta}{\partial t} \tag{A.9}$$

$$\frac{\partial Q}{\partial x} = \frac{\partial Q}{\partial \xi}\frac{\partial \xi}{\partial x} + \frac{\partial Q}{\partial \eta}\frac{\partial \eta}{\partial x} \tag{A.10}$$

$$\frac{\partial Q}{\partial y} = \frac{\partial Q}{\partial \xi}\frac{\partial \xi}{\partial y} + \frac{\partial Q}{\partial \eta}\frac{\partial \eta}{\partial y} \tag{A.11}$$

Substituting equations (A.9) through (A.11) into (A.1) through (A.5), and assuming a steady grid ($\partial \xi / \partial t = \partial \eta / \partial t = 0$) gives,

$$\frac{\partial Q}{\partial t} + \frac{\partial F_i}{\partial \xi} + \frac{\partial G_i}{\partial \eta} = \frac{\partial F_v}{\partial \xi} + \frac{\partial G_v}{\partial \eta} \tag{A.12}$$

$$Q = J^{-1}\begin{bmatrix} \rho_1 \\ \rho_2 \\ \vdots \\ \rho_N \\ \rho u \\ \rho v \\ E \end{bmatrix} \tag{A.13}$$

$$F_i = J^{-1}\begin{bmatrix} \rho_1 U \\ \rho_2 U \\ \vdots \\ \rho_N U \\ \rho u U + \xi_x p \\ \rho v U + \xi_y p \\ U(E+p) \end{bmatrix} \tag{A.14}$$

$$G_i = J^{-1}\begin{bmatrix} \rho_1 V \\ \rho_2 V \\ \vdots \\ \rho_N V \\ \rho u V + \eta_x p \\ \rho v V + \eta_y p \\ V(E+p) \end{bmatrix} \tag{A.15}$$

$$F_v = J^{-1}\begin{bmatrix} 0 \\ 0 \\ \vdots \\ 0 \\ \xi_x\tau_{xx} + \xi_y\tau_{xy} \\ \xi_x\tau_{xy} + \xi_y\tau_{yy} \\ \xi_x(u\tau_{xx} + v\tau_{xy} - q_x) + \xi_y(u\tau_{xy} + v\tau_{yy} - q_y) \end{bmatrix} \tag{A.16}$$

$$G_v = J^{-1}\begin{bmatrix} 0 \\ 0 \\ \vdots \\ 0 \\ \eta_x\tau_{xx} + \eta_y\tau_{xy} \\ \eta_x\tau_{xy} + \eta_y\tau_{yy} \\ \eta_x(u\tau_{xy} + v\tau_{yy} - q_y) + \eta_y(u\tau_{xy} + v\tau_{yy} - q_y) \end{bmatrix} \tag{A.17}$$

$$\tau_{xx} = \frac{2}{3}\mu[2(\xi_x u_\xi + \eta_x u_\eta) - (\xi_y v_\xi + \eta_y v_\eta)]$$

$$\tau_{yy} = \frac{2}{3}\mu[2(\xi_y v_\xi + \eta_y v_\eta) - (\xi_x u_\xi + \eta_x u_\eta)]$$

$$\tau_{xy} = \mu(\xi_y u_\xi + \eta_y u_\eta + \xi_x v_\xi + \eta_x v_\eta) \tag{A.18}$$

$$q_x = -k(\xi_x T_\xi + \eta_x T_\eta)$$

$$q_y = -k(\xi_y T_\xi + \eta_y T_\eta)$$

The generalized coordinate form of the equations is noticeably more complicated. The exception is the vector of conserved variables, Q, which only requires multiplication by a scale factor. For convenience, the flux vectors F and G have been split into inviscid and viscous parts and subscripts are used to denote partial derivatives. New

terms resulting from the transformation include J^{-1}, the inverse of the transformation Jacobian,

$$J^{-1} = \begin{vmatrix} x_\xi & x_\eta \\ y_\xi & y_\eta \end{vmatrix} = x_\xi y_\eta - x_\eta y_\xi \tag{A.19}$$

the grid metrics, ξ_x, ξ_y, η_x and η_y,

$$\xi_x = y_\eta J\ , \quad \eta_x = -y_\xi J\ , \quad \xi_y = -x_\eta J\ , \quad \eta_y = x_\xi J \tag{A.20}$$

and the contravariant velocities, U and V,

$$U = \xi_x u + \xi_y v\ , \quad V = \eta_x u + \eta_y v \tag{A.21}$$

Equations (A.12) through (A.21) are the "full" Navier-Stokes equations. They are expensive to solve and a simplified equation set is often satisfactory. The form of the equations used in the present work is the "thin-layer" Navier-Stokes equations (see Anderson, Tannehill and Pletcher, [50, pp. 421-424]). This approximation is a useful simplification of the Navier-Stokes equations for high speed, boundary-layer flows where flow separation will not occur. It basically drops all diffusion terms containing partial derivatives in the streamwise direction and retains the normal derivatives. The two conditions which must be satisfied for the thin-layer approximation to be valid are [30]:

1. Body surfaces are mapped onto coordinate surfaces in the computational plane.
2. Grid lines must be clustered to the surface and must be close to perpendicular.

The first requirement is automatically satisfied using non-orthogonal generalized coordinates.

Applying the thin-layer approximation to equations (A.12) to (A.21), the resulting thin-layer Navier-Stokes equations are [50],

$$\frac{\partial Q}{\partial t} + \frac{\partial F_i}{\partial \xi} + \frac{\partial G_i}{\partial \eta} = \frac{\partial G_{v2}}{\partial \eta} \tag{A.22}$$

where terms on the left side of the equation are unchanged, and the remaining viscous flux vector is,

$$G_{v2} = J^{-1} \begin{bmatrix} 0 \\ 0 \\ \vdots \\ 0 \\ \mu(\eta_x^2 + \eta_y^2)u_\eta + \frac{\mu}{3}(\eta_x u_\eta + \eta_y v_\eta)\eta_x \\ \mu(\eta_x^2 + \eta_y^2)v_\eta + \frac{\mu}{3}(\eta_x u_\eta + \eta_y v_\eta)\eta_y \\ (\eta_x^2 + \eta_y^2)\left[\frac{\mu}{2}(u^2 + v^2)_\eta + kT_\eta\right] + \frac{\mu}{3}(\eta_x u + \eta_y v)(\eta_x u_\eta + \eta_y v_\eta) \end{bmatrix} \tag{A.23}$$

A.2 2-D Axisymmetric

The full, multi-species Navier-Stokes equations in cylindrical coordinates (r, θ, z), specialized for axisymmetry $(\partial/\partial\theta = 0)$ and written in conservation form are,

$$\frac{\partial Q}{\partial t} + \frac{\partial F}{\partial r} + \frac{\partial G}{\partial z} = S \tag{A.24}$$

where,

$$Q = \begin{bmatrix} \rho_1 \\ \rho_2 \\ \vdots \\ \rho_N \\ \rho v_r \\ \rho v_z \\ E \end{bmatrix} \tag{A.25}$$

$$F = \begin{bmatrix} \rho_1 v_r \\ \rho_2 v_r \\ \vdots \\ \rho_N v_r \\ \rho v_r^2 + p - \tau_{rr} \\ \rho v_r v_z - \tau_{rz} \\ v_r(E + p) - v_r\tau_{rr} - v_z\tau_{rz} + q_r \end{bmatrix} \tag{A.26}$$

$$G = \begin{bmatrix} \rho_1 v_z \\ \rho_2 v_z \\ \vdots \\ \rho_N v_z \\ \rho v_r v_z - \tau_{rz} \\ \rho v_z^2 + p - \tau_{zz} \\ v_z(E+p) - v_r \tau_{rz} - v_z \tau_{zz} + q_z \end{bmatrix} \tag{A.27}$$

S is the axisymmetric source term,

$$S = -\frac{1}{r} \begin{bmatrix} \rho_1 v_r \\ \rho_2 v_r \\ \vdots \\ \rho_N v_r \\ \rho v_r^2 - \tau_{rr} \\ \rho v_r v_z - \tau_{rz} \\ v_r(E+p) - v_r \tau_{rr} - v_z \tau_{rz} + q_r \end{bmatrix} \tag{A.28}$$

and

$$\tau_{rr} = \mu \left[2\frac{\partial v_r}{\partial r} - \frac{2}{3}\left(\frac{1}{r}\frac{\partial r v_r}{\partial r} + \frac{\partial v_z}{\partial z}\right) \right]$$

$$\tau_{zz} = \mu \left[2\frac{\partial v_z}{\partial z} - \frac{2}{3}\left(\frac{1}{r}\frac{\partial r v_r}{\partial r} + \frac{\partial v_z}{\partial z}\right) \right]$$

$$\tau_{rz} = \mu \left(\frac{\partial v_r}{\partial z} + \frac{\partial v_z}{\partial r} \right) = \tau_{zr} \tag{A.29}$$

$$q_r = -k\frac{\partial T}{\partial r}$$

$$q_z = -k\frac{\partial T}{\partial z}$$

Transformed into generalized, nonorthogonal coordinates these equations become,

$$\frac{\partial Q}{\partial t} + \frac{\partial F_i}{\partial \xi} + \frac{\partial G_i}{\partial \eta} = S_1 + \frac{\partial F_v}{\partial \xi} + \frac{\partial G_v}{\partial \eta} \tag{A.30}$$

$$Q = J^{-1} \begin{bmatrix} \rho_1 \\ \rho_2 \\ \vdots \\ \rho_N \\ \rho v_r \\ \rho v_z \\ E \end{bmatrix} \tag{A.31}$$

$$F_i = J^{-1} \begin{bmatrix} \rho_1 U \\ \rho_2 U \\ \vdots \\ \rho_N U \\ \rho v_r U + \xi_r p \\ \rho v_z U + \xi_z p \\ U(E+p) \end{bmatrix} \tag{A.32}$$

$$G_i = J^{-1} \begin{bmatrix} \rho_1 V \\ \rho_2 V \\ \vdots \\ \rho_N V \\ \rho v_r V + \eta_r p \\ \rho v_z V + \eta_z p \\ V(E+p) \end{bmatrix} \tag{A.33}$$

$$F_v = J^{-1} \begin{bmatrix} 0 \\ 0 \\ \vdots \\ 0 \\ \xi_r \tau_{rr} + \xi_z \tau_{rz} \\ \xi_r \tau_{rz} + \xi_z \tau_{zz} \\ \xi_r (v_r \tau_{rr} + v_z \tau_{rz} - q_r) + \xi_z (v_r \tau_{rz} + v_z \tau_{zz} - q_z) \end{bmatrix} \tag{A.34}$$

$$G_v = J^{-1}\begin{bmatrix} 0 \\ 0 \\ \vdots \\ 0 \\ \eta_r\tau_{rr} + \eta_z\tau_{rz} \\ \eta_r\tau_{rz} + \eta_z\tau_{zz} \\ \eta_r(v_r\tau_{rr} + v_z\tau_{rz} - q_r) + \eta_z(v_r\tau_{rz} + v_z\tau_{zz} - q_z) \end{bmatrix} \tag{A.35}$$

$$S_1 = -\frac{J^{-1}}{r}\begin{bmatrix} \rho_1 v_r \\ \rho_2 v_r \\ \vdots \\ \rho_N v_r \\ \rho v_r^2 \\ \rho v_r v_z \\ v_r(E+p) \end{bmatrix} \tag{A.36}$$

$$\tau_{rr} = \mu\{2(\xi_r\partial_\xi v_r + \eta_r\partial_\eta v_r) - \frac{2}{3}[\frac{1}{r}(\xi_r\partial_\xi(rv_r) + \eta_r\partial_\eta(rv_r)) + \xi_z\partial_\xi v_z + \eta_z\partial_\eta v_z]\}$$

$$\tau_{zz} = \mu\{2(\xi_z\partial_\xi v_z + \eta_z\partial_\eta v_z) - \frac{2}{3}[\frac{1}{r}(\xi_r\partial_\xi(rv_r) + \eta_r\partial_\eta(rv_r)) + \xi_z\partial_\xi v_z + \eta_z\partial_\eta v_z]\}$$

$$\tau_{rz} = \mu(\xi_r\partial_\xi v_z + \eta_r\partial_\eta v_z + \xi_z\partial_\xi v_r + \eta_z\partial_\eta v_r) \tag{A.37}$$

$$q_r = -k(\xi_r T_\xi + \eta_r T_\eta)$$

$$q_z = -k(\xi_z T_\xi + \eta_z T_\eta)$$

Again, the full set of equations can be simplified using the thin-layer approximation ($\partial/\partial\xi = 0$). The left side of equation (A.30) remains the same. On the right hand side, S_1 remains the same, but the viscous flux vector F_v drops out entirely and the stress tensor and heat flux components making up the other viscous flux vector,

G_v, are simplified. Performing these simplifications and substituting into G_v, the resulting thin-layer, axisymmetric equations can be written as,

$$\frac{\partial Q}{\partial t} + \frac{\partial F_i}{\partial \xi} + \frac{\partial G_i}{\partial \eta} = S_1 + \frac{\partial G_{v2}}{\partial \eta} \quad \cdots \tag{A.38}$$

$$G_{v2} = J^{-1} \begin{bmatrix} 0 \\ 0 \\ \vdots \\ 0 \\ \mu(\eta_r^2 + \eta_z^2)\partial_\eta v_r + \frac{\mu}{3}[\eta_r(3\partial_\eta v_r - \frac{2}{r}\partial_\eta(rv_r)) + \eta_z \partial_\eta v_z]\eta_r \\ \mu(\eta_r^2 + \eta_z^2)\partial_\eta v_z + \frac{\mu}{3}[\eta_r(3\partial_\eta v_r - \frac{2}{r}\partial_\eta(rv_r)) + \eta_z \partial_\eta v_z]\eta_z \\ (\eta_r^2 + \eta_z^2)\left[\frac{\mu}{2}(v_r^2 + v_z^2)_\eta + kT_\eta\right] + \frac{\mu}{3}(\eta_r v_r + \eta_z v_z)[\eta_r(3\partial_\eta v_r - \frac{2}{r}\partial_\eta(rv_r)) + \eta_z \partial_\eta v_z] \end{bmatrix} \tag{A.39}$$

This is the form of the axisymmetric equations used in the present research.

Finally, note the similarity between the thin-layer equations for the axisymmetric and planar geometries (equations (A.22), (A.23)). They only difference is the addition of S_1, the axisymmetric source term, and in a slight difference in the viscous source term G_{v2}. A set of equations satisfying both geometries can be written in terms of a parameter, β,

$$\frac{\partial Q}{\partial t} + \frac{\partial F_i}{\partial \xi} + \frac{\partial G_i}{\partial \eta} = \beta S_1 + \frac{\partial S_2}{\partial \eta} \tag{A.40}$$

where Q, F_i, G_i are given by (A.13), (A.14) and (A.15), respectively. S_1 is now

$$S_1 = -\frac{J^{-1}}{x} \begin{bmatrix} \rho_1 u \\ \rho_2 u \\ \vdots \\ \rho_N u \\ \rho u^2 \\ \rho uv \\ u(E+p) \end{bmatrix} \tag{A.41}$$

and S_2 is

$$S_2 = J^{-1}\begin{bmatrix} 0 \\ 0 \\ \vdots \\ 0 \\ \mu(\eta_x^2+\eta_y^2)u_\eta + \frac{\mu}{3}[\eta_x(3u_\eta - 2x^{-\beta}(x^\beta u)_\eta) + \eta_y v_\eta]\eta_x \\ \mu(\eta_x^2+\eta_y^2)v_\eta + \frac{\mu}{3}(\eta_x(3u_\eta - 2x^{-\beta}(x^\beta u)_\eta) + \eta_y v_\eta]\eta_y \\ (\eta_x^2+\eta_y^2)\left[\frac{\mu}{2}(u^2+v^2)_\eta + kT_\eta\right] + \frac{\mu}{3}(\eta_x u + \eta_y v)[\eta_x(3u_\eta - 2x^{-\beta}(x^\beta u)_\eta) + \eta_y v_\eta] \end{bmatrix} \tag{A.42}$$

where β is,

$$\beta = \begin{cases} 0 & \text{for planar geometry} \\ 1 & \text{for axisymmetric geometry} \end{cases} \tag{A.43}$$

For planar geometry, x, y, u and v are defined as usual. For axisymmetric geometry, $x = r$, $y = z$, $u = v_r$ and $v = v_z$.

Appendix B

DERIVATION OF THE FLUX JACOBIAN

B.1 Single-Component, Ideal Gas With Constant Specific Heats

The Euler equations for a one-dimensional flow of a single-component fluid can be written as

$$\frac{\partial Q}{\partial t} + \frac{\partial F}{\partial x} = 0 \tag{B.1}$$

where

$$Q = [\rho, m, E]^T \tag{B.2}$$

$$F = [m, \frac{m^2}{\rho} + P, \frac{m}{\rho}(E + P)]^T \tag{B.3}$$

where x momentum, $m = \rho u$. Since $F = F(Q)$, write (B.1) alternatively as

$$\frac{\partial Q}{\partial t} + A\frac{\partial Q}{\partial x} = 0$$

where A is the flux jacobian

$$A = \begin{bmatrix} \frac{\partial F_1}{\partial Q_1} & \frac{\partial F_1}{\partial Q_2} & \frac{\partial F_1}{\partial Q_3} \\ \frac{\partial F_2}{\partial Q_1} & \frac{\partial F_2}{\partial Q_2} & \frac{\partial F_2}{\partial Q_3} \\ \frac{\partial F_3}{\partial Q_1} & \frac{\partial F_3}{\partial Q_2} & \frac{\partial F_3}{\partial Q_3} \end{bmatrix}$$

or in strict terms

$$A = \begin{bmatrix} \left(\frac{\partial F_1}{\partial Q_1}\right)_{Q_i, i\neq 1} & \left(\frac{\partial F_1}{\partial Q_2}\right)_{Q_i, i\neq 2} & \left(\frac{\partial F_1}{\partial Q_3}\right)_{Q_i, i\neq 3} \\ \left(\frac{\partial F_2}{\partial Q_1}\right)_{Q_i, i\neq 1} & \left(\frac{\partial F_2}{\partial Q_2}\right)_{Q_i, i\neq 2} & \left(\frac{\partial F_2}{\partial Q_3}\right)_{Q_i, i\neq 3} \\ \left(\frac{\partial F_3}{\partial Q_1}\right)_{Q_i, i\neq 1} & \left(\frac{\partial F_3}{\partial Q_2}\right)_{Q_i, i\neq 2} & \left(\frac{\partial F_3}{\partial Q_3}\right)_{Q_i, i\neq 3} \end{bmatrix}$$

Using (B.2) and (B.3),

$$A = \begin{bmatrix} \left(\frac{\partial m}{\partial \rho}\right)_{m,E} & \left(\frac{\partial m}{\partial m}\right)_{\rho,E} & \left(\frac{\partial m}{\partial E}\right)_{\rho,m} \\ \left(\frac{\partial\left[\frac{m^2}{\rho}+P\right]}{\partial \rho}\right)_{m,E} & \left(\frac{\partial\left[\frac{m^2}{\rho}+P\right]}{\partial m}\right)_{\rho,E} & \left(\frac{\partial\left[\frac{m^2}{\rho}+P\right]}{\partial E}\right)_{\rho,m} \\ \left(\frac{\partial\left[\frac{m}{\rho}(E+P)\right]}{\partial \rho}\right)_{m,E} & \left(\frac{\partial\left[\frac{m}{\rho}(E+P)\right]}{\partial m}\right)_{\rho,E} & \left(\frac{\partial\left[\frac{m}{\rho}(E+P)\right]}{\partial E}\right)_{\rho,m} \end{bmatrix}$$

which simplifies to

$$A = \begin{bmatrix} 0 & 1 & 0 \\ -\frac{m^2}{\rho^2} + \left(\frac{\partial P}{\partial \rho}\right)_{m,E} & \frac{2m}{\rho} + \left(\frac{\partial P}{\partial m}\right)_{\rho,E} & \left(\frac{\partial P}{\partial E}\right)_{\rho,m} \\ -\frac{m}{\rho^2}(E+P) + \frac{m}{\rho}\left(\frac{\partial P}{\partial \rho}\right)_{m,E} & \frac{E+P}{\rho} + \frac{m}{\rho}\left(\frac{\partial P}{\partial m}\right)_{\rho,E} & \frac{m}{\rho}\left[1 + \left(\frac{\partial P}{\partial E}\right)_{\rho,m}\right] \end{bmatrix}$$

A computationally useful form of A requires expressions for the three partial derivatives of pressure. This requires an equation of state and a definition for the energy density, E.

For a single-component ideal gas, the equation of state is the ideal gas law,

$$P = \rho \frac{R_u}{MW} T \tag{B.4}$$

where R_u is the universal gas constant and MW is the molecular weight of the gas. The energy density is the product of the gas density and the sum of the internal and kinetic energy,

$$E = \rho\left(\frac{1}{MW}\int_{T_{ref}}^{T} \bar{C}_v dT + \frac{1}{2}u^2\right)$$

which, with the added assumption of constant specific heats can be written as

$$E = \rho\left(\frac{\bar{C}_v}{MW} T + \frac{1}{2}u^2\right)$$

Using (B.4) and the fact that $R_u = \bar{C}_p - \bar{C}_v$ for an ideal gas, this becomes

$$E = \frac{P}{\gamma - 1} + \frac{m^2}{2\rho} \tag{B.5}$$

where $\gamma = \bar{C}_p/\bar{C}_v$. Since (B.5) can be solved explicitly for $P = P(\rho, E, m)$, the three partial derivatives can be easily obtained. (Such simplification is not generally possible as will be shown soon.)

Solving (B.5) for P

$$P = (\gamma - 1)\left[E - \frac{m^2}{2\rho}\right] \tag{B.6}$$

the desired partial derivatives are

$$\left(\frac{\partial P}{\partial E}\right)_{\rho,m} = \gamma - 1 \tag{B.7}$$

$$\left(\frac{\partial P}{\partial \rho}\right)_{m,E} = (\gamma - 1)\frac{m^2}{2\rho^2} = (\gamma - 1)\frac{u^2}{2} \tag{B.8}$$

$$\left(\frac{\partial P}{\partial m}\right)_{\rho,E} = -(\gamma - 1)\frac{m}{\rho} = -(\gamma - 1)u = -u\left(\frac{\partial P}{\partial E}\right)_{\rho,m} \tag{B.9}$$

These expressions (B.7-9) agree with [30].

B.2 Multi-Component, Ideal Gas With Variable Specific Heats

For this more general case, the form of the Euler equations (B.1) is the same except that $N-1$ equations are added for the additional species and a source term is added to account for chemical growth and depletion of the various species.

$$\frac{\partial Q}{\partial t} + \frac{\partial F}{\partial x} = W \tag{B.10}$$

where now

$$Q = [\rho_1, \rho_2, \cdots, \rho_N, m, E]^T \tag{B.11}$$

$$F = [m_1, m_2, \cdots, m_N, \frac{m^2}{\rho} + P, \frac{m}{\rho}(E + P)]^T \tag{B.12}$$

$$W = [w_1, w_2, \cdots, w_N, 0, 0]^T \tag{B.13}$$

and $m_i = \rho_i u$.

The flux jacobian is similarly expanded,

$$A = \begin{bmatrix} \left(\frac{\partial m_1}{\partial \rho_1}\right)_{m,E,\rho_i,i\neq 1} & \left(\frac{\partial m_1}{\partial \rho_2}\right)_{m,E,\rho_i,i\neq 2} & \cdots & \left(\frac{\partial m_1}{\partial \rho_N}\right)_{m,E,\rho_i,i\neq N} & \left(\frac{\partial m_1}{\partial m}\right)_{E,\rho_i} & \left(\frac{\partial m_1}{\partial E}\right)_{m,\rho_i} \\ \left(\frac{\partial m_2}{\partial \rho_1}\right)_{m,E,\rho_i,i\neq 1} & \left(\frac{\partial m_2}{\partial \rho_2}\right)_{m,E,\rho_i,i\neq 2} & \cdots & \left(\frac{\partial m_2}{\partial \rho_N}\right)_{m,E,\rho_i,i\neq N} & \left(\frac{\partial m_2}{\partial m}\right)_{E,\rho_i} & \left(\frac{\partial m_2}{\partial E}\right)_{m,\rho_i} \\ \vdots & \vdots & \ddots & \vdots & \vdots & \vdots \\ \left(\frac{\partial m_N}{\partial \rho_1}\right)_{m,E,\rho_i,i\neq 1} & \left(\frac{\partial m_N}{\partial \rho_2}\right)_{m,E,\rho_i,i\neq 2} & \cdots & \left(\frac{\partial m_N}{\partial \rho_N}\right)_{m,E,\rho_i,i\neq N} & \left(\frac{\partial m_N}{\partial m}\right)_{E,\rho_i} & \left(\frac{\partial m_N}{\partial E}\right)_{m,\rho_i} \\ \left(\frac{\partial\left[\frac{m^2}{\rho}+P\right]}{\partial \rho_1}\right)_{m,E,\rho_i,i\neq 1} & \left(\frac{\partial\left[\frac{m^2}{\rho}+P\right]}{\partial \rho_2}\right)_{m,E,\rho_i,i\neq 2} & \cdots & \left(\frac{\partial\left[\frac{m^2}{\rho}+P\right]}{\partial \rho_N}\right)_{m,E,\rho_i,i\neq N} & \left(\frac{\partial\left[\frac{m^2}{\rho}+P\right]}{\partial m}\right)_{E,\rho_i} & \left(\frac{\partial\left[\frac{m^2}{\rho}+P\right]}{\partial E}\right)_{m,\rho_i} \\ \left(\frac{\partial\left[\frac{m}{\rho}(E+P)\right]}{\partial \rho_1}\right)_{m,E,\rho_i,i\neq 1} & \left(\frac{\partial\left[\frac{m}{\rho}(E+P)\right]}{\partial \rho_2}\right)_{m,E,\rho_i,i\neq 2} & \cdots & \left(\frac{\partial\left[\frac{m}{\rho}(E+P)\right]}{\partial \rho_N}\right)_{m,E,\rho_i,i\neq N} & \left(\frac{\partial\left[\frac{m}{\rho}(E+P)\right]}{\partial m}\right)_{E,\rho_i} & \left(\frac{\partial\left[\frac{m}{\rho}(E+P)\right]}{\partial E}\right)_{m,\rho_i} \end{bmatrix} \tag{B.14}$$

Noting that $m = \rho u$ and $m_i = \rho_i u$ where ρ is the mixture density,

$$\rho = \sum_{i=1}^{N} \rho_i$$

careful application of the derivatives gives many simplifications in A. For example,

$$\left(\frac{\partial m_1}{\partial \rho_1}\right)_{m,E,\rho_i,i\neq 1} = u\frac{\partial \rho_1}{\partial \rho_1} + \rho_1 \left(\frac{\partial u}{\partial \rho_1}\right)_{m,E,\rho_i,i\neq 1}$$

The first term on the rhs is just u, the second term is also non-zero since

$$u = \frac{m}{\sum_i \rho_i}$$

$$\left(\frac{\partial u}{\partial \rho_1}\right)_{m,E,\rho_i,i\neq 1} = m\left(\frac{\partial}{\partial \rho_1}\left[\frac{1}{\sum_i \rho_i}\right]\right)_{m,E,\rho_i,i\neq 1} = -\frac{m(1)}{\left[\sum_i \rho_i\right]^2} = -\frac{u}{\rho}$$

If c_1 is defined as the mass fraction, ρ_1/ρ,

$$\left(\frac{\partial m_1}{\partial \rho_1}\right)_{m,E,\rho_i,i\neq 1} = u(1 - c_1)$$

Or in general,

$$\left(\frac{\partial m_j}{\partial \rho_k}\right)_{m,E,\rho_i,i\neq k} = u(\delta_{jk} - c_j) \tag{B.15}$$

where δ_{jk} is the Kronecker delta. Further examples are

$$\left(\frac{\partial m_j}{\partial m}\right)_{\rho_i,E} = u\left(\frac{\partial \rho_j}{\partial m}\right)_{\rho_i,E} + \rho_j\left(\frac{\partial}{\partial m}\left[\frac{m}{\rho}\right]\right)_{\rho_i,E} = c_j \tag{B.16}$$

since the first of the pair of derivatives is zero, and

$$\left(\frac{\partial m_j}{\partial E}\right)_{m,\rho_i} = u\left(\frac{\partial \rho_j}{\partial E}\right)_{m,\rho_i} + \rho_j\left(\frac{\partial}{\partial E}\left[\frac{m}{\rho}\right]\right)_{m,\rho_i} = 0 \tag{B.17}$$

since both derivatives are zero.

$$\left(\frac{\partial}{\partial \rho_k}\left[\frac{m^2}{\rho} + P\right]\right)_{m,E,\rho_i,i\neq k} = \frac{1}{\rho}\left(\frac{\partial m^2}{\partial \rho_k}\right)_m + m^2\left(\frac{\partial}{\partial \rho_k}\left[\frac{1}{\sum_i \rho_i}\right]\right)_{\rho_i,i\neq k} + \left(\frac{\partial P}{\partial \rho_k}\right)_{m,E,\rho_i,i\neq k}$$

$$= -\frac{m^2}{\left[\sum_i \rho_i\right]^2} + \left(\frac{\partial P}{\partial \rho_k}\right)_{m,E,\rho_i,i\neq k}$$

$$= \left(\frac{\partial P}{\partial \rho_k}\right)_{m,E,\rho_i,i\neq k} - u^2$$

$$\left(\frac{\partial}{\partial m}\left[\frac{m^2}{\rho}+P\right]\right)_{\rho_i,E} = \frac{1}{\rho}(2m) + m^2(0) + \left(\frac{\partial P}{\partial m}\right)_{\rho_i,E} = 2u + \left(\frac{\partial P}{\partial m}\right)_{\rho_i,E} \tag{B.18}$$

$$\left(\frac{\partial}{\partial E}\left[\frac{m^2}{\rho}+P\right]\right)_{\rho_i,m} = \left(\frac{\partial P}{\partial E}\right)_{\rho_i,m}$$

$$\left(\frac{\partial}{\partial \rho_k}\left[\frac{m}{\rho}(E+P)\right]\right)_{m,E,\rho_i,i\neq k} = m(E+P)\left(-\frac{1}{\rho^2}\right) + \frac{m}{\rho}\left(\frac{\partial P}{\partial \rho_k}\right)_{m,E,\rho_i,i\neq k}$$

$$= u\left[\left(\frac{\partial P}{\partial \rho_k}\right)_{m,E,\rho_i,i\neq k} - H\right]$$

where H, the specific total enthalpy, is defined for convenience as

$$H = \left(\frac{E+P}{\rho}\right) \tag{B.19}$$

$$\left(\frac{\partial}{\partial m}\left[\frac{m}{\rho}(E+P)\right]\right)_{\rho_i,E} = H(1) + \frac{m}{\rho}\left(\frac{\partial P}{\partial m}\right)_{\rho_i,E} = H + u\left(\frac{\partial P}{\partial m}\right)_{\rho_i,E} \tag{B.20}$$

$$\left(\frac{\partial}{\partial E}\left[\frac{m}{\rho}(E+P)\right]\right)_{\rho_i,m} = \frac{m}{\rho}\left[1 + \left(\frac{\partial P}{\partial E}\right)_{\rho_i,m}\right] = u\left[1 + \left(\frac{\partial P}{\partial E}\right)_{\rho_i,m}\right] \tag{B.21}$$

Substituting (B.15) through (B.21) into (B.14) gives a simplified form of A

$$A = \begin{bmatrix} u(1-c_1) & -uc_1 & \cdots & -uc_1 & c_1 & 0 \\ -uc_2 & u(1-c_2) & \cdots & -uc_2 & c_2 & 0 \\ \vdots & \vdots & \ddots & \vdots & \vdots & \vdots \\ -uc_N & -uc_N & \cdots & -u(1-c_N) & c_N & 0 \\ P_{\rho_1} - u^2 & P_{\rho_2} - u^2 & \cdots & P_{\rho_N} - u^2 & 2u + P_m & P_E \\ u(P_{\rho_1} - H) & u(P_{\rho_2} - H) & \cdots & u(P_{\rho_N} - H) & H + uP_m & u(1+P_E) \end{bmatrix} \tag{B.22}$$

where P_{ρ_i}, P_m and P_E represent the derivatives

$$P_{\rho_i} = \left(\frac{\partial P}{\partial \rho_i}\right)_{m,E,\rho_j,j\neq i} \quad P_m = \left(\frac{\partial P}{\partial m}\right)_{\rho_i,E} \quad P_E = \left(\frac{\partial P}{\partial E}\right)_{\rho_i,m}$$

Equation (B.22) agrees with the form given by [10].

As before, simplified expressions for the three partial derivatives of pressure requires an equation of state and a definition of energy density, E. The multi-component ideal gas law is the equation of state

$$P = \sum_{i=1}^{N} \frac{\rho_i}{MW_i} R_u T \tag{B.23}$$

The expression for specific internal energy, e, assumes variable specific heat and includes chemical energy as well as the sensible energy term. For species i,

$$e_i = \int_{T_{ref}}^{T} \bar{C}_{v_i} dT + \bar{h}^{o}_{f_i} \tag{B.24}$$

As shown, the internal energy is that above an arbitrary reference state. The chemical energy is given by the formation enthalpy since

$$\bar{h}^{o}_{f_i} = \bar{e}^{o}_{f_i} \tag{B.25}$$

The overbars in (B.24) and (B.25) denote molar quantities (e.g. $\bar{e}_i = J/k - mol$, $\bar{C}_{v_i} = J/(k - mol^o K)$). The superscript zero denotes values at standard state conditions.

The resulting definition for energy density is

$$E = \sum_{i=1}^{N} \left(\frac{\rho_i}{MW_i} \left[\int_{T_{ref}}^{T} \bar{C}_{v_i} dT + \bar{h}^{o}_{f_i} \right] \right) + \frac{m^2}{2\rho} \tag{B.26}$$

Unlike the single component, constant specific heat definition (B.5), T cannot be eliminated in (B.26) using the equation of state (B.23). This adds considerable difficulty in obtaining expressions for the partial derivatives of pressure.

Beginning with the easiest of the three, by chain rule

$$\left(\frac{\partial P}{\partial E}\right)_{\rho_i,m} = \left(\frac{\partial P}{\partial E}\right)_{\rho_i,T} + \left(\frac{\partial P}{\partial T}\right)_{\rho_i} \left(\frac{\partial T}{\partial E}\right)_{\rho_i,m} \tag{B.27}$$

The first derivative is zero, and from (B.23)

$$\left(\frac{\partial P}{\partial T}\right)_{\rho_i} = \sum_{i=1}^{N} \left(\frac{\rho_i}{MW_i}\right) R_u \tag{B.28}$$

Since

$$\left(\frac{\partial T}{\partial E}\right)_{\rho_i,m} = \left(\frac{\partial E}{\partial T}\right)^{-1}_{\rho_i,m} \tag{B.29}$$

and, from (B.26)

$$\left(\frac{\partial E}{\partial T}\right)_{\rho_i,m} = \sum_{i=1}^{N} \left(\frac{\rho_i}{MW_i} \bar{C}_{v_i}\right) \tag{B.30}$$

Substituting (B.28) through (B.30) into (B.27) gives the desired expression,

$$\left(\frac{\partial P}{\partial E}\right)_{\rho_i,m} = R_u \sum_i \left(\frac{\rho_i}{MW_i}\right) / \sum_i \left(\frac{\rho_i}{MW_i} \bar{C}_{v_i}\right) \tag{B.31}$$

Similarly

$$\left(\frac{\partial P}{\partial m}\right)_{\rho_i,E} = \left(\frac{\partial P}{\partial m}\right)_{\rho_i,T} + \left(\frac{\partial P}{\partial T}\right)_{\rho_i} \left(\frac{\partial T}{\partial m}\right)_{\rho_i,E} \tag{B.32}$$

Again, the first derivative is zero. Solving (B.26) for m

$$m = \left[\left(E - \sum_{i=1}^{N} \left(\frac{\rho_i}{MW_i} \left[\int_{T_{ref}}^{T} \bar{C}_{v_i} dT + \bar{h}^{o}_{f_i}\right]\right)\right) 2\rho\right]^{\frac{1}{2}} \tag{B.33}$$

$$\left(\frac{\partial T}{\partial m}\right)_{\rho_i,E} = \left(\frac{\partial m}{\partial T}\right)^{-1}_{\rho_i,E}$$

$$= \left[\frac{1}{2}(2\rho)\left(-\sum_i \frac{\rho_i}{MW_i} \bar{C}_{v_i}\right)/m\right]^{-1}$$

$$= -u / \sum_i \left(\frac{\rho_i}{MW_i} \bar{C}_{v_i}\right) \tag{B.34}$$

Substituting (B.34) and (B.28) into (B.32) gives

$$\left(\frac{\partial P}{\partial m}\right)_{\rho_i,E} = -uR_u \sum_i \left(\frac{\rho_i}{MW_i}\right) / \sum_i \left(\frac{\rho_i}{MW_i}\bar{C}_{v_i}\right)$$

$$= -u\left(\frac{\partial P}{\partial E}\right)_{\rho_i,m} \tag{B.35}$$

For the final derivative, expand as for the previous two

$$\left(\frac{\partial P}{\partial \rho_i}\right)_{m,E,\rho_j,j\neq i} = \left(\frac{\partial P}{\partial \rho_i}\right)_T + \left(\frac{\partial P}{\partial T}\right)_{\rho_i} \left(\frac{\partial T}{\partial \rho_i}\right)_{m,E,\rho_j,j\neq i} \tag{B.36}$$

In this case the first term is nonzero; by (B.23)

$$\left(\frac{\partial p}{\partial \rho_i}\right)_T = \frac{R_u T}{MW_i} \tag{B.37}$$

Furthermore, the last derivative in (B.36) is complicated in that both T and ρ_i are implicit variables in (B.26). First differentiate (B.26) with respect to ρ_i,

$$\left(\frac{\partial E}{\partial \rho_i}\right)_{m,E,\rho_j,j\neq i} = \sum_i \left(\frac{\rho_i}{MW_i}\bar{C}_{v_i}\right) \left(\frac{\partial T}{\partial \rho_i}\right)_{m,E,\rho_j,j\neq i}$$

$$+\frac{1}{MW_i}\left[\int_{T_{ref}}^{T} \bar{C}_{v_i} dT + h^o_{f_i}\right] \left(\frac{\partial \rho_i}{\partial \rho_i}\right)$$

$$+(-)\frac{1}{2(\sum_i \rho_i)^2} m^2 \left(\frac{\partial \rho_i}{\partial \rho_i}\right)$$

then solve for $\partial T/\partial \rho_i$ gives

$$\left(\frac{\partial T}{\partial \rho_i}\right)_{m,E,\rho_j,j\neq i} = \frac{\frac{u^2}{2} - \frac{1}{MW_i}\left[\int_{T_{ref}}^{T} \bar{C}_{v_i} dT + h^o_{f_i}\right]}{\sum_i \left(\frac{\rho_i}{MW_i}\bar{C}_{v_i}\right)} \tag{B.38}$$

Substituting (B.28), (B.37) and (B.38) into (B.36) and using the definition of $(\partial P/\partial E)_{\rho_i,m}$ from equation (B.31), get

$$\left(\frac{\partial P}{\partial \rho_i}\right)_{m,E,\rho_j,j\neq i} = \frac{R_u T}{MW_i} + \left(\frac{\partial P}{\partial E}\right)_{\rho_i,m} \left(\frac{u^2}{2} - \frac{1}{MW_i}\left[\int_{T_{ref}}^{T} \bar{C}_{v_i} dT + h^o_{f_i}\right]\right) \tag{B.39}$$

In summary then, for the one-dimensional flow [1] of a multi-component, ideal gas mixture with variable specific heats, the partial derivatives of pressure required for the flux jacobian are given by equations (B.31), (B.35) and (B.39). Repeated again these are,

$$\left(\frac{\partial P}{\partial E}\right)_{\rho_i,m} = R_u \sum_i \left(\frac{\rho_i}{MW_i}\right) / \sum_i \left(\frac{\rho_i}{MW_i}\bar{C}_{v_i}\right)$$

$$\left(\frac{\partial P}{\partial m}\right)_{\rho_i,E} = -u\left(\frac{\partial P}{\partial E}\right)_{\rho_i,m}$$

$$\left(\frac{\partial P}{\partial \rho_i}\right)_{m,E,\rho_j,j\neq i} = \frac{R_u T}{MW_i} + \left(\frac{\partial P}{\partial E}\right)_{\rho_i,m}\left(\frac{u^2}{2} - \frac{1}{MW_i}\left[\int_{T_{ref}}^{T} \bar{C}_{v_i} dT + h^{\circ}_{f_i}\right]\right)$$

[1] These expressions are identical for a two-dimensional flow with the exception of an added v^2 term in P_{ρ_i}.

VITA

JAMES A. FORT

Education

Ph.D.	Mechanical Engineering, University of Washington, 1993 computational fluid dynamics, combustion
M.S.	Mechanical Engineering, Oregon State University, 1983 thermal sciences, solid mechanics
B.S.	Mechanical Engineering, Oregon State University, 1979

Work Experience

9/90 to present - Battelle Memorial Institute, Pacific Northwest Laboratory, Richland, WA. Senior research engineer. Responsible for computational fluid dynamic analyses in incompressible fluid flow systems including waste tanks, ceramic melters and nuclear reactors.

1/84 to 8/87 - Flow Research, Kent, WA. Research engineer. Developed specialized applications of high pressure waterjet cutting systems.

7/79 to 12/83 - Battelle Memorial Institute, Pacific Northwest Laboratory, Richland, WA. Research engineer. Project areas included experimental fluid dynamics and computer modeling.